Finite Element Simulation of Nonlinear Fluids with Application to Granular Material and Powder

Dissertation
Doktors der Naturwissenschaften

Dem Fachbereich Mathematik der Universität Dortmund

vorgelegt am 2005 von

Abderrahim Ouazzi

Finite Element Simulation of Nonlinear Fluids with Application to Granular Material and Powder

Summary. This thesis is concerned with new numerical and algorithmic tools for flows with pressure and shear dependent viscosity together with the necessary background of the generalized Navier-Stokes equations.

In general, the viscosity can depend on the density, for instance in the case of compressible flow, and if the relation between the pressure and the density is reversible, the viscosity may depend on the pressure. This, however, is not the case for incompressible powder flow where the viscous stresses may change with varying pressure whereas density changes remain negligible. Meanwhile, the viscosity of the flow may change as the shear rate is varied, for instance in Bingham flow. Both dependencies can occur together, something that holds for the so-called non-flowing or slow-flowing materials, namely slow-flowing smaller-sized bulk powder. The Navier-Stokes equations in primitive variables (velocity-pressure) are regarded as the privilege answer to incorporate these phenomena. The modification of the viscous stresses leads to generalized Navier-Stokes equations extending the range of their validity to such flow.

The resulting equations are mathematically more complex than the Navier-Stokes equations. From the numerical point of view several problems arise. Firstly, the difficulty of approximating incompressible velocity fields. Secondly, poor conditioning and possible lack of differentiability of the involved nonlinear functions due to the material laws and finally, the eventual domination of convective effects.

The difficulty related to the approximation of incompressible velocity fields was treated by applying the non-conforming Rannacher-Turek Stokes element. However, with this approach another problem arises related to the low order nonconforming approximation for problems involving the symmetric part of the gradient: the classical discrete Korn's inequality is not satisfied. To handle this, the interior penalty stabilized finite element method in the frame of Nitsche's method was used. It requires a modification of the discrete bilinear form by adding an interface term, penalizing the jump of the velocity over edges. This was achieved via a modified procedure in the derivation of a discontinuous Galerkin formulation. This general approach is referred to as edge-oriented finite element method.

The lack of differentiability was treated by regularization. Then, the continuous Newton method as linearization technique was applied. The method consists of working directly on the variational integrals. Then, the corresponding continuous Jacobian operators were derived. Consequently, a convergence rate of the nonlinear iterations independent of the mesh refinement was achieved. This continuous approach is advantageous: Firstly, the explicit accessibility of the Jacobian allows adaptive treatment which leads to a robust method with respect to the starting guess. Secondly, it avoids the delicate task of choosing the step-length which is required for divided differences approaches.

Another criterion for the success of any numerical method is to overcome the numerical instabilities at high Reynolds number such that the Galerkin formulation fails and causes spurious oscillations. Although the edge-oriented method was introduced in the frame of hybrid finite element methods, it has been shown that the appropriate choice of edge-oriented stabilization is able to provide simultaneously excellent results regarding robustness and accuracy for both apparent problems of the numerical solution: the lack of coercivity and a convection dominated problem.

A fundamental issue for edge-oriented stabilization is the growing stencil for the stiffness matrix. The jump terms involve more than the adjacent elements; the problem of storing the new stabilization matrix arises. To overcome the storage problem, the stiffnes matrix would contain a part of stabilization matrix which fits into the same standard FEM data structure, while the complementary part is assembled via elementwise operations. Moreover, the construction of preconditioners for the corresponding linear systems would only include parts of the matrix. In parallel, a nonstandard edge-oriented data structure has been developed to support the additional contributed elements. So, the local element and edge matrices are easily deduced from the global one. Accordingly, efficient Vanka smoothers were introduced, namely a full cell-oriented Vanka smoother and edge-oriented Vanka smoother. In doing so, it became possible to privilege edge-oriented stabilization for CFD simulations. Moreover, the velocity-

pressure coupling was treated in linearized saddle point problems via local Multilevel Pressure Schur Complement methods.

The principle of empiric verification stands behind the wide range of well known benchmark calculations introduced to fulfill the objective need of performance.

Key words: Edge-oriented Finite Element Method, Multilevel Pressure Schur Complement, Newton's Method, Nonlinear Fluids, Granular Material.

Abderrahim Ouazzi
University of Dortmund, Germany

Acknowledgement. First and foremost, I would like to thank my supervisor, Prof. Dr. Stefan Turek, for introducing the topic to me, for his invaluable academic advice and for his subtle direction of my efforts throughout the preparation of this thesis. Gratitude is also due to Prof. Dr. Heribert Blum for accepting to review my thesis.

It is unimaginable that an academic effort of this magnitude could successfully come to fruition without the help of others. It's my pleasure to thank them all. Among them, Prof. Gabriel Tardos from The City College of New York who provided insights into the application with an integrated understanding of it and my colleague Dr. Jaroslav Hron for sharing ideas. My special thanks are due to all members of FeatFlow/ FEAST group. I would also like to thank Prof. Dr.-Ing. Günter Rombach and Frank Neumann from TU Hamburg-Harburg for the collaboration work under the DFG project (FKZ DFG (SP): TU 102/4-1; TU 102/4-3). And not to forget all other scientific assistants participating in the DFG program the initiative "Behavior of Granular Media" in Germany for both the successful and the intensive workshops allowing refinement of my research.

A. O.

Contents

Part II Applications: Granular and powder flow

1

Introduction

The aim of this thesis is to present new numerical and algorithmic tools for the solution of flow problems with shear and pressure dependent viscosity. The Navier-Stokes equations are generalized to model flow of material involving the dependence of the viscosity from both shear rate and pressure, namely granular material. So important is this issue and so relevant to industrial flows, that reliable numerical simulation is required. The original numerical techniques in the field of incompressible Navier-Stokes equations is extended with respect to these material models.

The Cauchy stress tensor is given by $\sigma = 2\nu(D_{\mathrm{II}}(\boldsymbol{u}), p)\mathbf{D}(\boldsymbol{u}) - p\mathbf{I}$, where p is the pressure; $\mathbf{D}(\boldsymbol{u}) = \frac{1}{2}(\nabla\boldsymbol{u} + \nabla^T\boldsymbol{u})$ is the rate of deformation tensor, $\boldsymbol{u}$ denotes the velocity, and $\nu(\cdot)$ is the (nonlinear) viscosity which may depend on the second invariant of the deformation rate tensor $D_{\mathrm{II}}(\boldsymbol{u}) = \frac{1}{2}\operatorname{tr}(\mathbf{D}^2(\boldsymbol{u}))$ and the pressure p. Then, depending on the chosen viscosity function $\nu(\cdot)$ the following prototypical models are considered:

1. Newtonian law

$$\nu(z, p) = \nu_{\mathrm{o}} \quad (\nu_{\mathrm{o}} > 0), \tag{1.1}$$

2. Carreau law

$$\nu(z) = \nu_\infty + (\nu_0 - \nu_\infty)(1 + \lambda z)^{\frac{r}{2}-1} \quad (\nu_{\mathrm{o}} > \nu_\infty \geq 0, \lambda > 0, r > 1), \tag{1.2}$$

3. Power law

$$\nu(z, p) = \nu_{\mathrm{o}} z^{\frac{r}{2}-1} \quad (\nu_{\mathrm{o}} > 0, r > 1), \tag{1.3}$$

4. Bingham law

$$\nu(z, p) = \nu_{\mathrm{o}} z^{-\frac{1}{2}} \quad (\nu_{\mathrm{o}} > 0), \tag{1.4}$$

5. Schaeffer's law

$$\nu(z, p) = \sqrt{2}\sin\phi\, p z^{-\frac{1}{2}} \quad (\phi \text{ is angle of internal friction}). \tag{1.5}$$

In all cases, the velocity $\boldsymbol{u}$ and the pressure p satisfy the following momentum and continuity equations which we refer to as generalized Navier-Stokes equations

$$\frac{\partial \boldsymbol{u}}{\partial t} + \boldsymbol{u}\cdot\nabla\boldsymbol{u} - \operatorname{div}\left(2\nu(D_{\mathrm{II}}(\boldsymbol{u}), p)\mathbf{D}(\boldsymbol{u})\right) + \nabla p = \boldsymbol{f}, \quad \operatorname{div}\boldsymbol{u} = 0\,. \tag{1.6}$$

especially, for Newtonian flow with constant viscosity (1.6) becomes

$$\frac{\partial \boldsymbol{u}}{\partial t} + \boldsymbol{u} \cdot \nabla \boldsymbol{u} - \nu \Delta \boldsymbol{u} + \nabla p = \boldsymbol{f}, \quad \operatorname{div} \boldsymbol{u} = 0\,. \tag{1.7}$$

In the following, let us consider the generalized Navier-Stokes problem in a bounded domain $\Omega \subset \mathbb{R}^2$, and use the rate of deformation tensor formulation (1.6) instead of the gradient formulation as in (1.7), unless it is stated explicitly.

The investigation is based on the work done by Turek et al. [91, 92], in which their research activities in the field of the incompressible Navier-Stokes equations have been concentrated on the development and realization of numerical techniques which provide sufficient flexibility and particularly efficiency for the solution of nonsteady flow problems for medium Reynolds numbers in realistic 2D and 3D configurations. As a main result, they developed the general framework of the *Multilevel Pressure Schur Complement* methods [92] which allows a classification and generalization of most of the available Navier-Stokes solvers in the CFD community (see for instance [27, 28, 29, 37, 70]). Then, having this general description, one has the possibility to select those ingredients for a new Navier-Stokes solver which can combine the higher accuracy of fully coupled Galerkin-type approaches - which solve Oseen-like equations in an outer Newton-like iteration - with the much faster projection-like schemes (following the ideas of Chorin [20], Van Kan [102] and Gresho [35]) which however have problems with accuracy and robustness due to their operator-splitting character. In combination with rigorous multigrid applications and special nonconforming FEM spaces, very efficient Navier-Stokes solvers have been derived which can handle the complete regime of very low up to medium Reynolds numbers in a steady as well as nonsteady context, on more or less general domains which include anisotropic mesh refinement in space and time. Due to the fully implicit treatment, the time step size is mainly due to accuracy reasons - in contrast to any 'hidden' stability restriction - such that error control approaches become feasible. The details for this general *Multilevel Pressure Schur Complement* approach are described in [92] and the realization is partially included in the FeatFlow software [91].

The contribution of this thesis has three aspects: the spatial discretization, the nonlinear solver and the linear solver. In part I, the selected examples from known CFD benchmarks are presented with the aim of providing satisfactory tests of the solver component, and more advanced applications from real life industry are described in detail in part II. The thesis follows the following organization:

Chapter 2: This chapter deals with a nonconforming finite element method for incompressible flow with the unavoidable stabilization techniques required for both: Firstly, the lack of coercivity due to the use of deformation tensor formulation rather than gradient formulation. This is done by edge-oriented stabilization. Secondly, the classical stabilization techniques for convection terms namely streamline diffusion and upwinding with the corresponding error analysis.

Chapter 3: The nonlinear coupling of the pressure and shear rate in the viscosity function is linearized via Newton method which leads to an additional term introducing a new nonclassical linear saddle point problem. Also, the investigations go towards the growing stencil due to the edge-oriented stabilization which leads to nonstandard FEM data structure. The corresponding multigrid components are analyzed in combination with local Multilevel Pressure Schur Complement methods.

Chapter 4: The deeper the investigation proceeds the clearer it becomes that a comparative study could give a view without ambiguity to our numerical components. For this reason, the chapter aims to examine the influence of two different FEM discretization techniques (conforming Q_2/P_1, nonconforming $\tilde{Q}_1/Q_0$ Stokes element) and solution procedures (nonlinear Newton variants and multigrid versus Krylov-space solvers for linear subproblems) onto the approximation properties and particularly the total efficiency of corresponding CFD simulation tools for non-Newtonian flow of power law type.

Chapter 5: To move towards a real CFD application, the edge-oriented stabilization method is analyzed without preventing any questions concerning the necessity, robustness and efficiency. It is shown that the appropriate choice of edge-oriented stabilization could be a candidate for a black box tool for all relevant Reynolds numbers and nonlinear viscosity.

Chapter 6: As an advanced real life application the generalized Navier-Stokes problem is developed to describe the flow of granular material in which the non-Newtonian effect of viscous stress varies with the shear rate and the pressure is considered. Drawing the main mathematical challenges, giving briefly how to overcome them and then presenting simulations which confirm the well known physical behavior for granular material, namely the instability in a hopper and the independence of drag force of the velocity.

Part I

Numerical Methods and Simulation Techniques for Nonlinear Incompressible Flow Problems

2

Nonconforming Finite Element Methods for Incompressible Flow

Nonconforming FEM approaches have proven advantageous for incompressible flow problems due to their excellent stability properties with respect to the LBB condition (2.17) and anisotropic mesh deformation [19, 23, 26, 65, 69, 74, 75]. Moreover, together with discrete projection techniques or Multilevel Pressure Schur Complement methods they allow very efficient FEM solvers for nonstationary problems [92]. And, finally, their edge-oriented degrees of freedom lead to very compact data structures which have big advantages for parallel high performance computations [5, 13, 94, 96, 97]. They are quite natural candidates to include error control mechanisms and concepts for adaptivity with respect to meshes in space and time [53, 84, 95].

2.1 Preliminaries

Let us consider the Laplace equation in a convex polygonal domain Ω:

$$-\triangle \boldsymbol{u} = f \quad , \quad \boldsymbol{u}_{|\partial\Omega} = 0\,, \tag{2.1}$$

where $f \in L_2(\Omega)$. For $\boldsymbol{u} \in H_0^1(\Omega) \cap H^2(\Omega)$, then (see [38])

$$\|\boldsymbol{u}\|_2 \leq C_\Omega \, \|f\|_0\,, \tag{2.2}$$

where $\|\cdot\|_2 := \|\cdot\|_{H^2(\Omega)}$ and $\|\cdot\|_0 := \|\cdot\|_{L^2(\Omega)}$.

To derive the weak formulation, first consider a test function $\boldsymbol{v} \in H_0^1(\Omega)$, then multiply (2.1) with $\boldsymbol{v}$ and integrate by parts to obtain the problem

Find $\boldsymbol{u} \in H_0^1(\Omega)$ such that:

$$a(\boldsymbol{u}, \boldsymbol{v}) = F(\boldsymbol{v}) \quad \forall \boldsymbol{v} \in H_0^1(\Omega) \quad , \quad \text{where} \tag{2.3}$$

$$a(\boldsymbol{u}, \boldsymbol{v}) = \int_\Omega \nabla \boldsymbol{u} \nabla \boldsymbol{v} \; dx \quad , \quad F(\boldsymbol{v}) \quad = \int_\Omega f \; \boldsymbol{v} \, dx\,. \tag{2.4}$$

Let $\mathcal{T}_h$ be a triangulation of the domain Ω and V_h the space of approximations, then the approximate problem reads

Find $\boldsymbol{u}_h \in V_h(\Omega)$ such that:

$$\begin{aligned} a_h(\boldsymbol{u}_h, \boldsymbol{v}) =& F(\boldsymbol{v}) \quad \forall \boldsymbol{v} \in V_h \quad , \quad \text{where} \\ a_h(\boldsymbol{u}, \boldsymbol{v}) =& \sum_{T \in \mathcal{T}_h} \int_T \nabla \boldsymbol{u} \nabla \boldsymbol{v} \; dx \quad \forall \boldsymbol{u}, \boldsymbol{v} \in V_h\,. \end{aligned} \tag{2.5}$$

2.1.1 Error analysis

This section will mainly sketch the results concerning the approximation in $H_0^1(\Omega)$. More detailed presentation can be found in Brenner and Scott [10], Brezzi and Fortin [11], Raviart and Thomas [76], Girault and Raviart [33], and Ciarlet [21]. Standard approximations of Sobolev spaces can be subdivided into two classes: conforming and nonconforming methods.

Conforming finite element approximation: In order to obtain a conforming finite element approximation, let us introduce a finite dimensional subspace $V_h^c \subseteq H_0^1(\Omega)$

$$V_h^c = \left\{ \begin{array}{c} \boldsymbol{v} \in L_2(\Omega) : \boldsymbol{v}_{|T} \in P_1(T), \forall T \in \mathcal{T}_h \\ \boldsymbol{v} \text{ is continuous at the vertices of } \mathcal{T}_h \text{ and} \\ \boldsymbol{v} = 0 \text{ at the vertices along } \partial\Omega. \end{array} \right\}, \tag{2.6}$$

and define the norm $\|\boldsymbol{v}\|_1 = (a(\boldsymbol{v},\boldsymbol{v}))^{\frac{1}{2}} = |\boldsymbol{v}|_{H^1(\Omega)}$. It follows from $V_h^c \subseteq H_0^1(\Omega)$ that $a_h(\boldsymbol{u},\boldsymbol{v}) = a(\boldsymbol{u},\boldsymbol{v}) \quad \forall \boldsymbol{u},\boldsymbol{v} \in V_h^c$, then

$$\|\boldsymbol{u} - \boldsymbol{u}_h\|_1 = \min_{\boldsymbol{v} \in V_h} \|\boldsymbol{u} - \boldsymbol{v}\|_1 . \tag{2.7}$$

With the linear interpolation operator π_h and for $\boldsymbol{u} \in H^2(\Omega)$ the error estimate holds (Brenner and Scott [10])

$$\|\boldsymbol{u} - \boldsymbol{u}_h\|_1 \leq \|\boldsymbol{u} - \pi_h \boldsymbol{u}\|_1 \leq Ch \|\boldsymbol{u}\|_2 . \tag{2.8}$$

Nonconforming finite element approximation: In contrast to the conforming finite element approximations, the nonconforming finite element approximations are not required to be globally continuous. It can also be seen in the frame of external approximations [11]. The nonconforming finite dimensional subspace V_h^{nc} is defined as follows

$$V_h^{nc} = \left\{ \begin{array}{c} \boldsymbol{v} \in L_2(\Omega) : \boldsymbol{v}_{|T} \in P_1(T), \forall T \in \mathcal{T}_h \\ \boldsymbol{v} \text{ is continuous at the midpoints of } \mathcal{T}_h \text{ and} \\ \boldsymbol{v} = 0 \text{ at the midpoints along } \partial\Omega \end{array} \right\}. \tag{2.9}$$

It is important to notice that $V_h^{nc} \not\subseteq H_0^1(\Omega)$. Let us introduce the energy norm $\|\boldsymbol{v}\|_h = (a_h(\boldsymbol{v},\boldsymbol{v}))^{\frac{1}{2}}$ on $V_h^{nc} + H_0^1(\Omega)$. Then, using the coerciveness and continuity assumptions, the following result known as Scott-Strang lemma holds (Brenner and Scott [10], Ciarlet [21] and Strang and Fix [86])

$$\|\boldsymbol{u} - \boldsymbol{u}_h\|_h \leq \min_{\boldsymbol{v} \in V_h} \|\boldsymbol{u} - \boldsymbol{v}\|_h + \max_{\boldsymbol{v} \in V_h \setminus \{0\}} \frac{|a_h(\boldsymbol{u},\boldsymbol{v}) - F(\boldsymbol{v})|}{\|\boldsymbol{v}\|_h}. \tag{2.10}$$

The right hand side of the inequality (2.10) contains the approximation error (first term) plus consistency error (second term). The consistency error measures how well the exact solution satisfies the discrete equations. This error vanishes for $V_h \subseteq H_0^1(\Omega)$ and the standard result for the conforming case (2.7) is recovered. Also here for $\boldsymbol{u} \in H^2(\Omega)$ the error estimate holds (Brenner and Scott [10])

$$\|\boldsymbol{u} - \boldsymbol{u}_h\|_h \leq Ch \|\boldsymbol{u}\|_2 . \tag{2.11}$$

The question arises, then, why one would like to use nonconforming finite elements ? Clearly, there are situations where nonconforming methods are suitable in for instance the incompressible fluid flow problems. In fact, the only function in V_h^c which satisfies the divergence-free condition is the zero vector function. In order to obtain a good approximation by a conforming method, one must use higher-order polynomials. On the other hand, the space V_h^{nc} can be used to solve such a problem even with low order polynomials (Brenner and Scott [10]).

2.2 Problems involving incompressibility

2.2.1 Navier-Stokes equations

Let us consider the nonstationary (or stationary, without the term $\frac{\partial \boldsymbol{u}}{\partial t}$) generalized Navier-Stokes problem (1.6) in a bounded domain $\Omega \subset \mathbb{R}^2$, first discretize the equations (1.6) in time by a standard numerical solution method for ODEs. For instance, the implicit θ-scheme for θ in the range of $[0,1]$ (backward Euler or Crank-Nicholson) or the Fractional-step-θ-scheme yields a sequence of boundary value problems of the form [92]

Given $\boldsymbol{u}^n$, *compute* $\boldsymbol{u} = \boldsymbol{u}^{n+1}$ *and* $p = p^{n+1}$ *by solving*

$$\begin{aligned}\left[\alpha \mathbf{I} + \theta(\boldsymbol{u}\cdot\nabla - \nabla\cdot\nu(\boldsymbol{u},p)\mathbf{D})\right]\boldsymbol{u} + \nabla p = \left[\alpha I - \theta_1(\boldsymbol{u}^n\cdot\nabla - \nabla\cdot\nu(\boldsymbol{u}^n,p^n)\mathbf{D})\right]\boldsymbol{u}^n \\ + \theta_2 \boldsymbol{f}^{n+1} + \theta_3 \boldsymbol{f}^n\end{aligned} \tag{2.12}$$

subject to the incompressibility constraint $\nabla\cdot\boldsymbol{u} = 0$.

where $(\cdot)^n$ indicates the value of the generic quantity $(\cdot)$ at time step t_n for time-dependent problems and the n-th iteration for the steady-state formulation. The time-dependent problem is defined for $\alpha := 1/\Delta t$, while the steady-state formulation is recovered for $\alpha := 0$, $\theta = \theta_1 = \theta_3 = 1,$ and $\theta_2 = 0$.

For the spatial discretization let V_h and Q_h be approximate spaces of $H_0^1(\Omega)$ and $L_2(\Omega)$ respectively, then the approximate problem may have the following algebraic system form:

Compute $\boldsymbol{u}$ *and* p *by solving*

$$\mathbf{A}\boldsymbol{u} + \mathbf{B}\,p = \boldsymbol{g} \quad , \quad \mathbf{B}^T\boldsymbol{u} = 0 \qquad \text{where} \tag{2.13}$$

$$\boldsymbol{g} = \left[\alpha M - \theta_1 \mathbf{L}(\boldsymbol{u}^n, p^n) - \theta_1 N(\boldsymbol{u}^n)\right]\boldsymbol{u}^n + \theta_2 f^{n+1} + \theta_3 f^n. \tag{2.14}$$

Here, M is the (consistent or lumped) mass matrix, $\mathbf{B}$ is the discrete gradient operator and $-\mathbf{B}^T$ is the associated divergence operator. Furthermore,

$$\mathbf{A}\boldsymbol{u} = \left[\alpha M + \theta \mathbf{L}(\boldsymbol{u},p) + \theta \mathbf{N}(\boldsymbol{u})\right]\boldsymbol{u}, \tag{2.15}$$

where $\mathbf{L}(\boldsymbol{u},p)$ is the discrete nonlinear viscouss term and $\mathbf{N}(\boldsymbol{u})$ is the nonlinear transport operator. Furthermore, the fully discretized equations (2.12) as well as the linear subproblems can be solved within the outer iteration loop for a Fixpoint defect correction or Newton method. They may admit the following representation:

$$\begin{bmatrix} \mathbf{A} & \mathbf{B} \\ \mathbf{B}^T & 0 \end{bmatrix} \begin{bmatrix} \boldsymbol{u} \\ p \end{bmatrix} = \begin{bmatrix} \boldsymbol{g} \\ 0 \end{bmatrix}. \tag{2.16}$$

This is a saddle point problem in which the pressure acts as the Lagrange multiplier for the incompressibility constraint. As a consequence, the choice of the spaces V_h and Q_h is subject to the so-called LBB-condition named after Ladyzhenskaya, Babuška and Brezzi[33]

$$\min_{q_h \in Q_h} \max_{\boldsymbol{v}_h \in V_h} \frac{(q_h, \nabla\cdot\boldsymbol{v}_h)}{\|q_h\|_0 \|\nabla \boldsymbol{v}_h\|_0} \geq \beta > 0, \tag{2.17}$$

where β is a mesh-independent constant and $(\cdot,\cdot)$ the L_2 inner product. This condition is also known as the inf-sup condition and it is hard to check in its abstract form (2.17). In practice, it is deduced from the continuous one by construction of a family of uniformly continuous operators embedded into stable subspaces [11].

2.2.2 Mixed Stokes elements

For the generalized Navier-Stokes equations (1.6), a mixed finite element method based on a primitive formulation is advantageous. This formulation allows direct and simultaneous access to the most relevant physical quantities: pressure and velocity. Furthermore the method is suitable for the treatment of the nonlinear coupling of the pressure and velocity in the viscous term.

Let us now present two examples of admissible elements, namely conforming Q_2/P_1 (see [7, 11]) and nonconforming $\tilde{Q}_1/Q_0$ see [75]. Currently, these two pairs of elements are probably the most popular on quadrilateral meshes. They are linked in the discontinuous pressure group (Crouzeix-Raviart family [24]) which leads to cell oriented Vanka smoother [50]. So, the analysis concerning the linear solver for $\tilde{Q}_1/Q_0$ is to be deduced similarly for Q_2/P_1.

The nonconforming Stokes element $\tilde{Q}_1/Q_0$

For the parametric rotated bilinear element $\tilde{Q}_1$, let $\psi_T : \hat{T} \to T$ be the bilinear transformation for each $T \in \mathcal{T}_h$ to the unit square. So, $\tilde{Q}_1$ is defined by

$$\tilde{Q}_1 := \left\{ q \circ \psi_T^{-1} : q \in \text{span} < 1, x, y, x^2 - y^2 > \right\}. \tag{2.18}$$

The degrees of freedom are determined by the following nodal functionals $\{F_\Gamma^{(a,b)}(\cdot), \Gamma \subset \partial\mathcal{T}_h\}$, with

$$F_\Gamma^a := |\Gamma|^{-1} \int_\Gamma v d\gamma \qquad \text{or} \qquad F_\Gamma^b := v(m_\Gamma) \quad (m_\Gamma \text{ midpoint of edge } \Gamma) \tag{2.19}$$

such that the finite element space can be written as

$$\begin{aligned} W_h^{a,b} := \{ & v \in L_2(\Omega_h), v \in \tilde{Q}_1(T), \forall T \in \mathcal{T}_h, v \text{ continuous with respect to all} \\ & \text{nodal functionals } F_{\Gamma_{i,j}}^{a,b}(\cdot), \text{ and } F_{\Gamma_{i0}}^{a,b}(v) = 0, \forall \Gamma_{i0} \}. \end{aligned} \tag{2.20}$$

Here, $\Gamma_{i,j}$ denote all inner edges sharing the two elements i and j, while Γ_{i0} denotes the boundary edges of $\partial\Omega_h$. The corresponding discrete functions will be approximated in the spaces

$$V_h := W_h^{a,b} \times W_h^{a,b}, \; Q_h := \left\{ q_h \in L_0^2(\Omega), q_{h|T} = \text{const.}, \forall \mathcal{T} \in \mathcal{T}_h \right\}. \tag{2.21}$$

A convergence analysis is given in [75] and computational results are reported in [92]. This nonconforming finite element is a quadrilateral counterpart of the well-known Stokes element of Crouzeix-Raviart [23] and similarly the stability condition holds for the pair (V_h^a, Q_h) from the uniform one with a constant β independent of the mesh's aspect ratio. In contrast, for the "midpoint oriented" finite element V_h^b the independence of the stability constant on the mesh aspect ratio is restricted with the modification of the bilinear form $\mathbf{B}(\cdot,\cdot)$ by its numerically integrated version [90]

$$\begin{aligned} (\mathbf{B}^{(b)} q_h, \boldsymbol{v}_h) &:= -\sum_{T \in \mathcal{T}_h} q_h \sum_{\Gamma \subset \partial T} F_\Gamma^b(\boldsymbol{v}_h) \cdot \boldsymbol{n}_\Gamma \\ &\approx -\sum_{T \in \mathcal{T}_h} q_h \sum_{\Gamma \subset \partial T} \oint_\Gamma \boldsymbol{v}_h \cdot \boldsymbol{n}_\Gamma \, d\gamma \end{aligned} \tag{2.22}$$

Furthermore, on general nonuniform meshes the bilinear transformations $\psi_T : \hat{T} \to T$ are of another polynomial type than the shape functions on T.

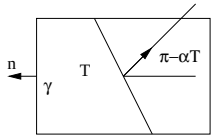

Fig. 2.1. Deterioration of quadrilaterals (from [90])

Set $\sigma_h = \max\{|\pi - \alpha_T|, T \in \mathcal{T}_h\}$ and i_h the interpolation operator, so we obtain the following error estimate [90]

$$\|v - i_h v\|_0 + h\,\|v - i_h v\|_h \le ch(h + \sigma_h)\,\|v\|_2\,, \quad \forall v \in H_0^1(\Omega) \cap H^2(\Omega) \tag{2.23}$$

In contrast to the parametric counterpart, let (ξ, η) be a local coordinate system obtained by joining the midpoints of the opposing faces of T.

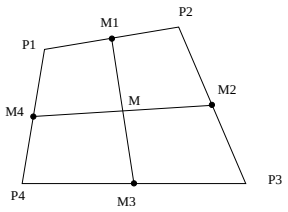

Fig. 2.2. General quadrilateral T

Then, in the *nonparametric* case, set on each element T

$$\tilde{Q}_1(T) := \text{span} < 1, \xi, \eta, \xi^2 - \eta^2 >, \tag{2.24}$$

hence, we get the error estimate independent of σ_h

$$\|v - i_h v\|_0 + h\,\|v - i_h v\|_h \le ch^2\,\|v\|_2\,, \quad \forall v \in H_0^1(\Omega) \cap H^2(\Omega). \tag{2.25}$$

As a consequence the optimal order convergence estimates holds [75]

$$\|\boldsymbol{u} - \boldsymbol{u}_h\|_h + \|p - p_h\|_0 \le c\,h\,\{\|\boldsymbol{u}\|_2 + \|p\|_1\}\,. \tag{2.26}$$

The conforming Stokes element Q_2/P_1

Let us define the finite dimensional spaces V_h and Q_h for the velocity and the pressure approximations as

$$V_h = \{\boldsymbol{v}_h \in \mathbf{H}_0^1(\Omega_h)^2, \quad \boldsymbol{v}_{h|T} \in Q_2(T)^2 \ \ \forall T \in \mathcal{T}_h, \quad \boldsymbol{v}_h = 0 \text{ on } \partial\Omega_h\}, \tag{2.27}$$

$$Q_h = \{p_h \in L^2(\Omega_h), \quad p_{h|T} \in P_1(T) \ \ \forall T \in \mathcal{T}_h\}, \tag{2.28}$$

and consider for each $T \in \mathcal{T}_h$ the bilinear transformation $\psi_T : \hat{T} \to T$ to the unit square T. So, $Q_2(T)$ is defined by

$$Q_2(T) = \left\{ q \circ \psi_T^{-1} : q \in \text{span} < 1, x, y, xy, x^2, y^2, x^2y, y^2x, x^2y^2 > \right\} \tag{2.29}$$

with nine local degrees of freedom located at the vertices, midpoints of the edges and in the center of the quadrilateral. The space $P_1(T)$ consists of linear functions defined by

$$P_1(T) = \left\{ q \circ \psi_T^{-1} : q \in \text{span} < 1, x, y > \right\} \tag{2.30}$$

with the function value and both partial derivatives located in the center of the quadrilateral, as its three local degrees of freedom. The inf-sup condition is satisfied (see [7]). However, the combination of the bilinear transformation ψ with a linear function on reference square $P_1(\hat{T})$ would imply that the basis on the reference square did not contain the full bilinear basis. So, the method can at most be first order accurate on general meshes (see [3, 7])

$$\|p - p_h\|_0 = O(h). \tag{2.31}$$

The standard remedy (see [3, 75, 92]) is to consider a local coordinate system (ξ, η) obtained by joining the midpoints of the opposing faces of T. Then, we set on each element T

$$P_1(T) := \text{span} < 1, \xi, \eta > . \tag{2.32}$$

For this case, the inf-sup condition is also satisfied and the second order approximation is recovered for the pressure [7, 33]

$$\|p - p_h\|_0 = O(h^2). \tag{2.33}$$

For a smooth solution, the approximation error for the velocity in the L_2-norm is of order $O(h^3)$ which can easily be demonstrated for prescribed polynomials or for smooth data on appropriate domains [7].

2.2.3 Elasticity problem and locking

The equations of linear elasticity in two dimensions is defined as follows: Find the displacement $\boldsymbol{u}$ and the symmetric stress tensor σ such that

$$\begin{aligned} \sigma = \lambda \nabla \cdot \boldsymbol{u} \mathbf{I} + 2\mu \mathbf{D}(\boldsymbol{u}) \text{ in } \Omega, \\ -\nabla \cdot \sigma = \mathbf{f} \text{ in } \Omega, \\ \boldsymbol{u} = \boldsymbol{g} \text{ on } \partial\Omega_D, \\ \sigma \cdot \boldsymbol{n} = \boldsymbol{h} \text{ on } \partial\Omega_N, \end{aligned} \tag{2.34}$$

where $\mathbf{f}$ and $\boldsymbol{h}$ are given loads, and $\boldsymbol{g}$ is a given boundary displacement. The so-called Lamé constants λ and μ satisfy $0 < \mu_1 < \mu < \mu_2$ and $0 < \lambda < \infty$ and are related to the Poisson ratio μ and the Young's modulus E by the following formulas:

$$\lambda = \frac{E\mu}{(1+\mu)(1-2\mu)} \quad , \quad \nu = \frac{E}{2(1+\mu)}. \tag{2.35}$$

As the Poisson ratio approaches $\frac{1}{2}$ the incompressible behavior dominates and locking phenomena occurs so that the performance of standard conforming methods will detoriate (see Brenner and Scott [10]). A remedy is to introduce the dual variable $p = -\lambda \operatorname{div} \boldsymbol{u}$ and consider the corresponding mixed formulation (see Brezzi and Fortin [11]). Here again the spaces V_h and Q_h are subject to the LBB condition (2.17). The nonconforming method leads to robust methods with the constraint of fulfilling a discrete Korn's inequality. Korn's inequality guarantees the coercivity of the corresponding weak formulation of problems (2.34) and (1.6) since it involves the strain tensor operator instead of the gradient operator. In what follows some results concerning Korn's inequality are presented.

2.3 Korn's inequality

To establish the coercivity of the variational formulations for both problems elasticity (2.34) and generalized Navier-Stokes (1.6), appropriate versions of Korn's inequality are needed. Here, let us briefly outline the recent results related to the topic and refer the reader to [4, 9, 10, 32] for detailed presentation where one also finds further references.

Theorem 1. *(Classical Korn's inequality cf. Nitsche [68]) Let $d \geq 2$ and $\Omega \in \mathbb{R}^d$ be an open and bounded domain with Lipschitz boundary. Then there exists $c(\Omega) > 0$ such that*

$$\|\mathbf{D}(\boldsymbol{v})\|_0^2 + \|\boldsymbol{v}\|_0^2 \geq c\,\|\boldsymbol{v}\|_1^2 \tag{2.36}$$

for every $\boldsymbol{v} \in H^1(\Omega)$.

Proposition 1. *(Korn's first inequality cf. [68, 83]) Let $d \geq 2$ and $\Omega \in \mathbb{R}^d$ be open and bounded with Lipschitz boundary. Assume that the Dirichlet boundary $\partial\Omega_D$ has a positive surface measure. Then there exists $c(\Omega, \partial\Omega_D) > 0$ such that*

$$\|\mathbf{D}(\boldsymbol{v})\|_0^2 \geq c\,\|\boldsymbol{v}\|_1^2 \tag{2.37}$$

for every $\boldsymbol{v} \in H^1(\Omega)$ with homogeneous Dirichlet boundary value on $\partial\Omega_D$.

The extension of Korn's inequality to the nonlinear case can be found for instance in Fuchs [32]. Recently, Brenner [9] introduced a general version for piecewise H^1 vector fields. In fact, let $\mathbf{RM}(\Omega)$ be the space of rigid body motions, defined by

$$\mathbf{RM}(\Omega) = \left\{ a + \eta x : a \in R^d, \eta = -\eta^T \right\}, \tag{2.38}$$

which is exactly the kernel of the strain tensor $\mathbf{D}$ in $H^1(\Omega)$ (see [9, 83]), then there holds

Proposition 2. *(cf.[9]) For any seminorm Φ on $[H^1(\Omega)]^d$ with the following properties:*

1. $\Phi(\boldsymbol{v}) \leq c_\Phi \|\boldsymbol{v}\|_1 \quad \forall \boldsymbol{v} \in [H^1(\Omega)]^d, \quad$ *where c_Φ is a generic constant depending on Φ, and*
2. $\Phi(m) = 0$ *and* $m \in \mathbf{RM}(\Omega) \Leftrightarrow m$ *is a constant vector.*

Then the following inequality holds

$$\|\nabla \boldsymbol{v}\|_0 \leq c_\Phi(\|\mathbf{D}(\boldsymbol{u})\|_0 + \Phi(\boldsymbol{v})) \quad \forall \boldsymbol{v} \in [H^1(\Omega)]^d. \tag{2.39}$$

By the way, let us point out some of the early attempts to surmount the instability of the nonconforming low order approximation with the strain tensor formulation. Turek in [93] has established Korn's inequality for the rotated bilinear $\tilde{Q}_1$ element. In fact, the strain tensor can be written in the following manner

$$\begin{aligned} \mathbf{D}(\boldsymbol{v}) &= \frac{1}{2}(\nabla \boldsymbol{v} + \nabla^T \boldsymbol{v}) \\ &= \nabla \boldsymbol{v} - \frac{1}{2}(\nabla \boldsymbol{v} - \nabla^T \boldsymbol{v}) \\ &= \nabla \boldsymbol{v} - \frac{1}{2}(\operatorname{rot} \boldsymbol{v})\chi \quad , \quad \text{where} \end{aligned} \tag{2.40}$$

$$\chi = \begin{bmatrix} 0 & -1 \\ 1 & 0 \end{bmatrix} \quad \text{and} \quad \operatorname{rot} \boldsymbol{v} = \frac{\partial \boldsymbol{v}_2}{\partial x_1} - \frac{\partial \boldsymbol{v}_1}{\partial x_2} \tag{2.41}$$

with appropriate local projection of the rotational operator in the discrete formulation, the discrete Korn's inequality holds. For the elasticity problem, Lee et al. [62] introduced high-order polynomials for $\tilde{Q}_1$.

The most successful way to establish Korn's inequality for a low order nonconforming finite element methods is to use interior penalty stabilized finite element methods in the frame of Nitsche's method [9, 39, 98] referred to as edge-oriented stabilization.

2.3.1 Edge-oriented stabilization for the nonconforming element

The continuity requirement, for the Rannacher-Turek element, across the edges of the triangulation is weakened to the validity of patch test of order one, then the classical discrete Korn's inequality is not satisfied [56] which is important for problems involving the symmetric part of the gradient.

Another perspective is to point out Hughes's argument for the Crouzeix-Raviart element [39, 48]: prescribing the displacement along one side of an element means prescribing the displacement in only one node, which cannot preclude rigid body rotation.

To avoid this problem, Hansbo and Larson modify the Rannacher-Turek element for elasticity [39], and treat it with discontinuous Galerkin approximations by Nitsche's method. Hence, after omitting the consistency terms involving the normal derivatives on the boundaries of the elements, following Rannacher and Turek [75], appropriate edge-oriented stabilization techniques (see [9, 39, 98]) have to be included which directly treat the jump across the interelementary boundaries via adding the following bilinear forms

$$\langle \mathbf{J}\boldsymbol{u}, \boldsymbol{v}\rangle = \gamma \sum_{E\in E_I\cup E_D} \frac{1}{|E|}\int_E [\boldsymbol{u}][\boldsymbol{v}]d\sigma \tag{2.42}$$

Here, $\gamma = \gamma(\nu)$ is an additional relaxation parameter and the jump of a function $\boldsymbol{u}$ on an edge E is given by

$$[\boldsymbol{u}] = \begin{cases} \boldsymbol{u}^+\cdot\boldsymbol{n}^+ + \boldsymbol{u}^-\cdot\boldsymbol{n}^- & \text{on internal edges } E_I\ , \\ \boldsymbol{u}\cdot\boldsymbol{n} & \text{on Dirichlet boundary edges } E_D, \\ 0 & \text{on Neumann boundary edges } E_N, \end{cases} \tag{2.43}$$

where $\boldsymbol{n}$ is the outward normal to the edge and $(\cdot)^+$ and $(\cdot)^-$ indicate the value of a generic quantity $(\cdot)$ on the two elements sharing the same edge. For a detailed description of the analysis for this stabilization technique, we refer to [39] and [9].

Corollary 1. *(General Korn's inequality cf. [9])*

$$\|\boldsymbol{v}\|_h^2 \le c(\|\mathbf{D}(\boldsymbol{v})\|_{L_2(\Omega)}^2 + \|\boldsymbol{v}\|_{L_2(\Gamma)}^2 + \sum_E \frac{1}{|E|}\|[\boldsymbol{v}]_E\|_{L_2(E)}^2), \qquad \forall \boldsymbol{v}\in \prod_{T\in\mathcal{T}_h} H^1(T). \tag{2.44}$$

Let us introduce the mesh dependent norm on the space V_h

$$\begin{aligned} |\!|\!|\boldsymbol{v}|\!|\!|^2 &= \sum_{T\in\mathcal{T}_h}\int_T \nu\,\mathbf{D}(\boldsymbol{v}):\mathbf{D}(\boldsymbol{v})\,dx + \langle \mathbf{J}\boldsymbol{v},\boldsymbol{v}\rangle \quad , \quad \text{where} \\ \mathbf{D}(\boldsymbol{u}):\mathbf{D}(\boldsymbol{v}) &= \sum_{ij}\mathbf{D}_{ij}(\boldsymbol{u})\mathbf{D}_{ij}(\boldsymbol{v}). \end{aligned} \tag{2.45}$$

2.3.2 Error estimates and robustness

In the following, let us present a priori error estimates for the linear (Stokes) case (see [39, 92]). Then, the nonlinear case can be treated in the same manner following Baranger and Najib [4].

Theorem 2. *(inf-sup condition cf. [40, 39]) There exists a constant β strictly positive and independent of h such that*

$$\beta \leq \inf_{q \in Q_h} \sup_{v \in V_h} \frac{(q, \nabla \cdot v)}{|||\boldsymbol{v}||| \, \|q\|_{Q_h}}, \tag{2.46}$$

moreover,the following bound for errors holds

$$\|u - u_h\|_h + \|p - p_h\|_0 \leq c\, h \left\{ \|\boldsymbol{u}\|_2 + \|p\|_1 \right\}. \tag{2.47}$$

As a first test, let us introduce the specific kernel function on the unit square (see [56]) which takes -1 or 1 on the midpoints (see Fig. 2.3). If $u = \sum_i X_i \phi_i$, then define the (semi-)norm $\|u\|_M = (\sum_{i,j} M_{ij} X_i X_j)^{\frac{1}{2}}$ for any positive definite matrix M and introduce the constant $C_M = \frac{\|u\|_M}{\|u\|_A}$. Let G, T and ST be the stiffness matrices resulting from the discretization including the gradient, deformation tensor and stabilized deformation tensor, respectively. Then, the following table clearly demonstrates that $C_T = 0$, in contrast to $C_{ST} = O(1)$.

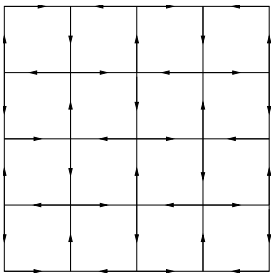

Level	NEL	$\|u\|_G$	$\|u\|_T$	$\|u\|_{ST}$
2	4	0.91	0.63×10^{-15}	0.30
3	16	1.1	0.20×10^{-14}	0.60
4	64	1.3	0.41×10^{-14}	0.76
5	256	1.3	0.69×10^{-14}	0.85
6	1024	1.4	0.14×10^{-14}	0.90
7	4096	1.4	0.30×10^{-13}	0.92
8	16384	1.4	0.61×10^{-13}	0.93

Fig. 2.3. The specific kernel function and examples for the constant in Korn's inequality on an equidistant refined unit square

2.4 Stabilization of convection terms

One quantity which has an important effect on the quality of the resulting discrete solution is the local Reynolds number Re_T defined as

$$Re_T = \frac{\|\boldsymbol{u}\|_{\infty,T} \cdot h_T}{\nu} \tag{2.48}$$

where h_T is a measure of element size and $\| \, \|_{\infty,T}$ is the maximum norm on the element T . In particular, if the Reynolds number is big which occur whenever convective operators are dominant then the standard Galerkin formulation fails and leads to nonphysical oscillations. A preliminary step towards minimizing the effects of these oscillations is to stabilize the discrete problem by using certain stabilization techniques like FEM upwinding, FEM streamline-diffusion, or algebraic FEM-FCT and FEM-TVD. While these schemes have been successfully integrated into nonconforming rotated bilinear $\tilde{Q}_1/Q_0$ finite element approximations [58, 59, 60, 66, 87, 92], it is not obvious what to do in the case of high order finite elements, for instance the pair Q_2/P_1.

2.4.1 FEM upwinding

The main idea is to introduce new edge-centered lumping regions and special lumping operators (for details see [92]).

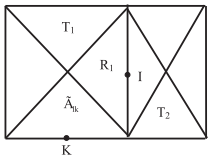

Fig. 2.4. Lumping region R_l around midpoint l (see [92])

Here, the discrete convective operator $\langle \mathbf{N}(\boldsymbol{u})\boldsymbol{v}, \boldsymbol{w}\rangle$ is replaced by:

$$\langle \tilde{\mathbf{N}}(\boldsymbol{u})\boldsymbol{v}, \boldsymbol{w}\rangle := \sum_{l} \sum_{k\in\Lambda_l} \oint_{\Gamma_{lk}} \boldsymbol{u}\cdot\boldsymbol{n}_{lk} d\gamma [1-\lambda_{lk}(\boldsymbol{u})(\boldsymbol{v}(m_k)-\boldsymbol{v}(m_l))]\boldsymbol{w}(m_l). \tag{2.49}$$

Based on the local Reynolds number Re_T on each cell T the following definition holds:

$$\lambda_{lk}(\boldsymbol{u}) = \begin{cases} \dfrac{\frac{1}{2}+\delta^* Re_T}{1+\delta^* Re_T} & \text{if } Re_T \geq 0 \\ \dfrac{1}{2(1-\delta^* Re_T)} & \text{otherwise} \end{cases} \tag{2.50}$$

where h_T is a local mesh parameter on each cell T which can be critical on highly distorted meshes. Moreover, the appropriate choice of the free parameter δ^* is quite sensitive and can significantly influence the resulting accuracy. The convergence in the energy norm is of order $O(h\log(h))$ (see [90] for details).

2.4.2 FEM streamline-diffusion

This method was originally proposed by Johnson [52], and by Hughes and Brooks [49]. The method has been successfully applied to several classes of problems since streamline-diffusion methods can combine both good stability and high accuracy. Due to its simplicity, streamline-diffusion is a common tool used in many (commercial) CFD codes. It mainly consists of adding the following stabilization term to the original convection operator described by $\langle \mathbf{N}(\boldsymbol{u})\boldsymbol{v}, \boldsymbol{w}\rangle$, which means

$$\langle \tilde{\mathbf{N}}(\boldsymbol{u})\boldsymbol{v}, \boldsymbol{w}\rangle = \langle \mathbf{N}(\boldsymbol{u})\boldsymbol{v}, \boldsymbol{w}\rangle + \langle \mathbf{N}_{sd}(\boldsymbol{u})\boldsymbol{v}, \boldsymbol{w}\rangle \quad , \quad \text{where} \tag{2.51}$$

$$\langle \mathbf{N}_{sd}(\boldsymbol{u})\boldsymbol{v}, \boldsymbol{w}\rangle = \sum_{T\in T_h} \delta_T \int_T (\boldsymbol{u}\cdot\nabla\boldsymbol{v})(\boldsymbol{u}\cdot\nabla\boldsymbol{w})\, dx. \tag{2.52}$$

Here, the critical quantity for an efficient computational treatment is the local damping parameter δ_T. A usual setting is described, for instance, in [92]. The local Reynolds number Re_T can be introduced as before and the parameter δ_T can be defined, for instance, as follows

$$\delta_T = \delta^* \frac{h_T}{\|\boldsymbol{u}\|_{\infty,\Omega}} \frac{2Re_T}{1+Re_T} \tag{2.53}$$

The formulation (2.52) adds additional coercivity in the local flow direction. Moreover, the convergence is of order $O(h^{3/2})$ in the streamline-diffusion norm for the $\tilde{Q}_1$ element on rectangular shape-regular tensor-product meshes. This order of convergence is similar to the well known estimate for the conforming case (see [87] for details).

Due to the more complex bilinear form, including numerical integration in certain quadrature points, the numerical cost of the matrix assembling process is increased and, again, the precise definition of δ^* and h_T, particularly on strongly anisotropic meshes containing large aspect ratios, can be critical. Finally, the application to nonsteady problems and the extension to more complex coupled problems or systems, as for instance Boussinesq approximations or multiphase flow problems is not fully clear.

2.5 Conclusions

The two pairs of Stokes elements presented in this chapter constitute the simplest elements in their families (conforming and nonconforming). It is clear that the simplest nonconforming element - that works - is simpler than the simplest conforming element - that works -, furthermore with nonconforming method one easily deals with central method. The more extensive analyses required for nonconforming finite element methods is also reflecting the capability of nonconformity to adapt to new, different and changing requirements for any numerical simulations which is our final aim.

3

Nonlinear and Linear Solvers

A fast and robust solver for nonlinear incompressible flow is the core of this chapter. Based on the result of the critical evaluation of the benchmark computations by Turek and Schäfer [100], multigrid method in conjunction with 'Local Pressure Schur complement' schemes (see [59, 92]) have been proven as efficient solvers for the incompressible Navier-Stokes problem. Here, the investigation is concerned with the flexibility, robustness and efficiency of multigrid solvers with respect to edge-oriented stabilization and the nonlinearities due to the described convective operator $\boldsymbol{u}\cdot\nabla\boldsymbol{u}$ and the nonlinear viscosity function $\nu(D_{\mathrm{II}}(\boldsymbol{u}),p)$.

3.1 Problem formulation

Let us consider the stationary generalized Navier-Stokes problem (1.6) in a bounded domain $\Omega\subset\mathbb{R}^2$. If we restrict the set V of test functions to be divergence-free and take the constitutive laws into account, the (stationary) equations (1.6) lead to:

Find $\boldsymbol{u}\in V$ such that

$$\int_\Omega 2\nu(D_{\mathrm{II}}(\boldsymbol{u}),p)\mathbf{D}(\boldsymbol{u}):\mathbf{D}(\boldsymbol{v})\,dx+\int_\Omega(\boldsymbol{u}\cdot\nabla\boldsymbol{u})\boldsymbol{v}\,dx=\int_\Omega \boldsymbol{f}\boldsymbol{v}\,dx,\ \forall\boldsymbol{v}\in V. \tag{3.1}$$

It is straightforward to penalize the constraint $\operatorname{div}\boldsymbol{u}=0$ to derive the equivalent mixed formulation:

Find $(\boldsymbol{u},p)\in X\times M$ such that

$$\begin{aligned}\int_\Omega 2\nu(D_{\mathrm{II}}(\boldsymbol{u}),p)\mathbf{D}(\boldsymbol{u}):\mathbf{D}(\boldsymbol{v})\,dx+\int_\Omega(\boldsymbol{u}\cdot\nabla\boldsymbol{u})\boldsymbol{v}\,dx\quad&+\int_\Omega p\operatorname{div}\boldsymbol{v}\,dx\\ =\int_\Omega \boldsymbol{f}\boldsymbol{v}\,dx,\qquad&\forall\boldsymbol{v}\in X,\\ \int_\Omega q\operatorname{div}\boldsymbol{u}\,dx=0,\qquad&\forall q\in M,\end{aligned} \tag{3.2}$$

with spaces $X=H_0^1(\Omega)$ and $M=L^2(\Omega)$ for the Newtonian case. In general these spaces depend on the function ν (see [4] for the precise definition of X and M). Also, the related Stokes problems to be considered, which means that the convective term $\int_\Omega(\boldsymbol{u}\cdot\nabla\boldsymbol{u})\boldsymbol{v}\,dx$ to be omitted. For the following analysis, let us introduce the bilinear forms:

$$\langle L(\boldsymbol{w},q)\boldsymbol{u},\boldsymbol{v}\rangle = \int_\Omega 2\nu(D_{\mathrm{II}}(\boldsymbol{w}),q)\mathbf{D}(\boldsymbol{u}) : \mathbf{D}(\boldsymbol{v})\,dx, \tag{3.3}$$

$$\langle N(\boldsymbol{w})\boldsymbol{u},\boldsymbol{v}\rangle = \int_\Omega (\boldsymbol{w}\cdot\nabla\boldsymbol{u})\boldsymbol{v}\,dx \quad \text{and} \quad \langle \mathbf{B}q,\boldsymbol{v}\rangle = \int_\Omega q\,\mathrm{div}\,\boldsymbol{v}\,dx. \tag{3.4}$$

Then, we can rewrite our generalized flow problem in the following compact form:

Find $(\boldsymbol{u},p)\in X\times M$ *such that*

$$\begin{aligned} \langle L(\boldsymbol{u},p)\boldsymbol{u},\boldsymbol{v}\rangle + \langle N(\boldsymbol{u})\boldsymbol{u},\boldsymbol{v}\rangle + \langle Bp,\boldsymbol{v}\rangle &= \int_\Omega \boldsymbol{f}\boldsymbol{v}dx, \quad \forall \boldsymbol{v}\in X,\\ \langle Bq,\boldsymbol{u}\rangle &= 0, \qquad\qquad \forall q\in M. \end{aligned} \tag{3.5}$$

3.2 Nonlinear solvers

3.2.1 Discrete Newton solver

After applying the discretization method to the system (3.5) where the approximations belong to the finite dimensional spaces (2.27) and (2.28), a system for the residual of nonlinear algebraic equations is obtained:

$$\mathcal{R}(\boldsymbol{x}) = \mathbf{0}, \tag{3.6}$$

where $\boldsymbol{x}$ represents the vector of the coefficients corresponding to the unknowns $(\boldsymbol{u}_h,p_h)$.

To solve this system, let us apply a Newton method with damping which results in iterations of the form

$$\boldsymbol{x}^{n+1} = \boldsymbol{x}^n + \omega^n \left[\frac{\partial\mathcal{R}(\boldsymbol{x}^n)}{\partial\boldsymbol{x}}\right]^{-1}\mathcal{R}(\boldsymbol{x}^n). \tag{3.7}$$

This iteration is repeated until a certain conditions on the quality of the solution are met, which means a certain norm of the residue $\|\mathcal{R}(\boldsymbol{x}^n)\|$ is small enough. The damping parameter $\omega^n\in(-1,0)$ is chosen such that

$$\mathcal{R}(\boldsymbol{x}^{n+1})\cdot\boldsymbol{x}^{n+1} \le \mathcal{R}(\boldsymbol{x}^n)\cdot\boldsymbol{x}^n. \tag{3.8}$$

The damping greatly improves the robustness of the Newton iteration in the case when the current approximation $\boldsymbol{x}^n$ is not close enough to the final solution since the Newton method without damping is not guaranteed to converge.

The Jacobian matrix $\left[\frac{\partial\mathcal{R}(\boldsymbol{x}^n)}{\partial\boldsymbol{x}}\right]$ can be approximated using finite differences as

$$\left[\frac{\partial\mathcal{R}(\boldsymbol{x}^n)}{\partial\boldsymbol{x}}\right]_{ij} \approx \frac{\mathcal{R}_i(\boldsymbol{x}^n+\varepsilon\boldsymbol{e}_j)-\mathcal{R}_i(\boldsymbol{x}^n-\varepsilon\boldsymbol{e}_j)}{2\varepsilon}, \tag{3.9}$$

where the vector $\boldsymbol{e}_j=(\delta_{ij})$ and δ_{ij} is the standard Kronecker symbol. The parameter ε can be fixed or can be modified according to some norm of the solution $\|\boldsymbol{x}^n\|$ or the norm of the update in the previous step $\|\boldsymbol{x}^n-\boldsymbol{x}^{n-1}\|$.

3.2.2 Continuous Newton solver

Diffusive term

In this approach, the nonlinearity is first handled on the continuous level. Let $(\boldsymbol{u}^l, p^l)$ be the initial state, then the (continuous) Newton method consists of finding $(\boldsymbol{u}, p) \in V \times M$ such that

$$\begin{aligned}\int_\Omega 2\nu(D_{\mathrm{II}}(\boldsymbol{u}^l), p^l)\mathbf{D}(\boldsymbol{u}) : \mathbf{D}(\boldsymbol{v})dx \\ + \int_\Omega 2\partial_1\nu(D_{\mathrm{II}}(\boldsymbol{u}^l), p^l)[\mathbf{D}(\boldsymbol{u}^l) : \mathbf{D}(\boldsymbol{u})][\mathbf{D}(\boldsymbol{u}^l) : \mathbf{D}(\boldsymbol{v})]dx \\ + \boxed{\int_\Omega 2\partial_2\nu(D_{\mathrm{II}}(\boldsymbol{u}^l), p^l)[\mathbf{D}(\boldsymbol{u}^l) : \mathbf{D}(\boldsymbol{v})]pdx} \\ = \int_\Omega \boldsymbol{f}\boldsymbol{v} - \int_\Omega 2\nu(D_{\mathrm{II}}(\boldsymbol{u}^l), p^l)\mathbf{D}(\boldsymbol{u}^l) : \mathbf{D}(\boldsymbol{v})dx, \quad \forall \boldsymbol{v} \in V\,, \end{aligned} \tag{3.10}$$

where $\partial_i\nu(\cdot,\cdot); i = 1, 2$ is the partial derivative of ν related to the first and second variables, respectively (see [46] for shear dependent viscosity only). To see this, set $\boldsymbol{X} = \mathbf{D}(\boldsymbol{u}^l), \boldsymbol{x} = \mathbf{D}(\boldsymbol{u}), Y = p^l, y = p, F(\boldsymbol{x}, y) = \nu(\frac{1}{2}|\boldsymbol{x}|^2, y)\boldsymbol{x}$ and $f(t) = F(\boldsymbol{X} + t\boldsymbol{x}, Y + ty)$, so that

$$\begin{aligned}\partial_{x_j}F_i(\boldsymbol{x}, y) &= \partial_{x_j}\nu(\tfrac{1}{2}|\boldsymbol{x}|^2, y)x_jx_i + \nu(\tfrac{1}{2}|\boldsymbol{x}|^2, y)\delta_{ij} \\ \partial_y F_i(\boldsymbol{x}, y) &= \partial_y\nu(\tfrac{1}{2}|\boldsymbol{x}|^2, y)x_i\end{aligned} \tag{3.11}$$

where δ_{ij} stands for the standard Kronecker symbol. Having

$$\begin{aligned}f_i^{'}(t) &= \textstyle\sum_j \partial_{x_j}F_i(\boldsymbol{X} + t\boldsymbol{x}, Y + ty)x_j + \partial_y F_i(\boldsymbol{X} + t\boldsymbol{x}, Y + ty)y \\ &= \nu(\tfrac{1}{2}|\boldsymbol{X} + t\boldsymbol{x}|^2, Y + ty)\boldsymbol{x}_i \\ &+ \partial_1\nu(\tfrac{1}{2}|\boldsymbol{X} + t\boldsymbol{x}|^2, Y + ty)\langle\boldsymbol{X} + t\boldsymbol{x}, \boldsymbol{x}\rangle(\boldsymbol{X}_i + t\boldsymbol{x}_i) \\ &+ \partial_2\nu(\tfrac{1}{2}|\boldsymbol{X} + t\boldsymbol{x}|^2, Y + ty)y(\boldsymbol{X}_i + t\boldsymbol{x}_i)\end{aligned} \tag{3.12}$$

then decrease t towards zero, to obtain the Frechet derivative:

$$\begin{aligned}\nabla \cdot[\ & 2\nu(D_{\mathrm{II}}(\boldsymbol{u}^l), p^l)\mathbf{D}(\boldsymbol{u}) \\ &+ 2\partial_1\nu(D_{\mathrm{II}}(\boldsymbol{u}^l), p^l)(\mathbf{D}(\boldsymbol{u}^l) : \mathbf{D}(\boldsymbol{u}))\mathbf{D}(\boldsymbol{u}^l) \\ &+ 2\partial_2\nu(D_{\mathrm{II}}(\boldsymbol{u}^l), p^l)p\mathbf{D}(\boldsymbol{u}^l)].\end{aligned} \tag{3.13}$$

Finally, the weak formulation of (3.13) leads to the relation given in (3.10). Therefore, the resulting auxiliary subproblems in each Newton step consist of finding $(\boldsymbol{u}, p) \in X \times M$ as solutions of the linear systems

$$\begin{cases} L(\boldsymbol{u}^l, p^l)\boldsymbol{u} + \delta_d L^*(\boldsymbol{u}^l, p^l)\boldsymbol{u} + B\,p + \delta_p B^*(\boldsymbol{u}^l, p^l)p = R_u(\boldsymbol{u}^l, p^l), \\ B^T\boldsymbol{u} \qquad\qquad\qquad\qquad\qquad\qquad\qquad\qquad\quad = R_p(\boldsymbol{u}^l, p^l), \end{cases} \tag{3.14}$$

where $R_u(\cdot,\cdot)$ and $R_p(\cdot,\cdot)$ denote the corresponding nonlinear residual terms for the momentum and continuity equations. The operators $L^*(\boldsymbol{u}^l, p^l)$ and $B^*(\boldsymbol{u}^l, p^l)$ are defined as follows:

$$\langle L^*(\boldsymbol{u}^l, p^l)\boldsymbol{u}, \boldsymbol{v}\rangle = \int_\Omega 2\partial_1\nu(D_{\mathrm{II}}(\boldsymbol{u}^l), p^l)[D(\boldsymbol{u}^l) : D(\boldsymbol{u})][D(\boldsymbol{u}^l) : D(\boldsymbol{v})]\,dx, \tag{3.15}$$

$$\langle B^*(\boldsymbol{u}^l, p^l)\boldsymbol{v}, p\rangle = \int_\Omega 2\partial_2\nu(D_{\mathrm{II}}(\boldsymbol{u}^l), p^l)[D(\boldsymbol{u}^l) : D(\boldsymbol{v})]p\,dx. \tag{3.16}$$

Convective term

The corresponding Newton linearization applied to the convective term $\langle N(\boldsymbol{u})\boldsymbol{u}, \boldsymbol{v}\rangle$ leads to the additional bilinear form

$$\langle N(\boldsymbol{u}^l)\boldsymbol{u}, \boldsymbol{v}\rangle + \delta_c \langle N^*(\boldsymbol{u}^l)\boldsymbol{u}, \boldsymbol{v}\rangle \quad \forall \boldsymbol{v} \in X \quad , \quad \text{where} \tag{3.17}$$

$$\langle N^*(\boldsymbol{u}^l)\boldsymbol{u}, \boldsymbol{v}\rangle = \int_\Omega (\boldsymbol{u} \cdot \nabla \boldsymbol{u}^l)\boldsymbol{v} dx \quad \forall \boldsymbol{v} \in X. \tag{3.18}$$

Stabilization terms

It is well-known that the 'standard' discretization of the convective term with central discretization, may lead to numerical problems:

- Stiffness matrices not of positive type ('M-matrix properties'), hence the iterative schemes such as multigrid will not give efficient convergence results.
- Oscillations and deteriorations of the discrete solutions which have purely numerical character.

To stabilize the convective term in the FEM context, there are two approaches which are widely used in the CFD community: *Upwind* schemes and *Streamline-diffusion* techniques. However, these two stabilization methods may annihilate the (potentially) quadratic convergence of the Newton methods unless the Jacobian matrix for the stabilization terms is computed too. The Newton method for the streamline-diffusion terms (2.52) consists of the following addition:

$$\langle \mathbf{N}_{sd}(\boldsymbol{u}^l)\boldsymbol{u}, \boldsymbol{v}\rangle + \delta_{sd} \langle \mathbf{N}^*_{sd}(\boldsymbol{u}^l)\boldsymbol{u}, \boldsymbol{v}\rangle \quad \forall \boldsymbol{v} \in V_h \quad , \quad \text{where} \tag{3.19}$$

$$\begin{aligned} \langle \mathbf{N}^*_{sd}(\boldsymbol{u}^l)\boldsymbol{u}, \boldsymbol{v}\rangle = & \sum_{T \in T_h} \delta_T \int_T (\boldsymbol{u}^l \cdot \nabla \boldsymbol{u}^l)(\boldsymbol{u} \cdot \nabla \boldsymbol{v})\, dx \\ & + \sum_{T \in T_h} \delta_T \int_T (\boldsymbol{u}^l \cdot \nabla \boldsymbol{u})(\boldsymbol{u}^l \cdot \nabla \boldsymbol{v})\, dx \\ & + \sum_{T \in T_h} \delta_T \int_T (\boldsymbol{u} \cdot \nabla \boldsymbol{u}^l)(\boldsymbol{u}^l \cdot \nabla \boldsymbol{v})\, dx \end{aligned} \tag{3.20}$$

while upwind stabilization techniques require special treatment of $\langle \mathbf{N}^*(\boldsymbol{u}^l)\boldsymbol{u}, \boldsymbol{v}\rangle$.

Once the Newton step $(\boldsymbol{u}, p)$ has been determined, the current approximation can be updated, with ω^l as an appropriate relaxation parameter, that is

$$(\boldsymbol{u}^{l+1}, p^{l+1}) = (\boldsymbol{u}^l, p^l) + \omega^l (\boldsymbol{u}, p). \tag{3.21}$$

Altogether, the complete algorithm of the approximate linearized problem may have the following algebraic system form:

Compute $\mathbf{u}$ *and* p *by solving*

$$(\mathbf{A} + \mathbf{J})\boldsymbol{u} + \tilde{\mathbf{B}} p = \mathbf{Res}_u(\boldsymbol{u}^l, p^l) \quad , \quad \mathbf{B}^T \boldsymbol{u} = \mathbf{Res}_p(\boldsymbol{u}^l, p^l) \quad , \quad \text{where} \tag{3.22}$$

$\mathbf{Res}_u(\cdot,\cdot)$ and $\mathbf{Res}_p(\cdot,\cdot)$ denote the corresponding nonlinear residual terms for the momentum and continuity equations, $-\mathbf{B}^T$ is the discrete divergence operator and $\mathbf{J}$ is the edge-oriented stabilization matrix. Furthermore,

$$\begin{aligned} \mathbf{A}\boldsymbol{u} &= \left[(\mathbf{L} + \delta_d \mathbf{L}^*)(\boldsymbol{u}^l, p^l) + (\tilde{\mathbf{N}} + \delta_c \mathbf{N}^*)(\boldsymbol{u}^l)\right] \boldsymbol{u}, \\ \tilde{\mathbf{B}} p &= \left[\mathbf{B} + \delta_p \mathbf{B}^*(\boldsymbol{u}^l, p^l)\right] p \end{aligned} \tag{3.23}$$

where $\mathbf{L}(\boldsymbol{u}, p)$ is the discrete linearized Laplacian, $\tilde{\mathbf{N}}(\boldsymbol{u})$ is the stabilized discrete linearized transport operator, $\mathbf{L}^*(\boldsymbol{u}, p), \mathbf{B}^*(\boldsymbol{u}, p)$ and $\mathbf{N}^*(\boldsymbol{u})$ are the discrete matrices corresponding to the operators in (3.15), (3.16) and (3.18). Furthermore it admits the following matrix representation

$$\begin{pmatrix} \mathbf{A} + \mathbf{J} & \tilde{\mathbf{B}} \\ \mathbf{B}^T & 0 \end{pmatrix} \begin{bmatrix} \boldsymbol{u} \\ p \end{bmatrix} = \begin{bmatrix} \mathbf{Res}_u \\ \mathbf{Res}_p \end{bmatrix}. \tag{3.24}$$

Some remarks: The full Newton method is performed for $\delta_d = 1$, $\delta_c = 1$ and $\delta_p = 1$, while the Fixpoint method corresponds to $\delta_d = 0$, $\delta_c = 0$ and $\delta_p = 0$. For $\delta_p = 0$, the linear problem behaves similar to the classical saddle point problem for power law models, while for $\delta_p \neq 0$ a non-standard type of problem involving the nonsymmetric pressure matrix $\mathbf{B}^*$ is obtained. The strategy to apply Newton method is to use a few iterations only with the Fixpoint method and as soon as the solution reaches some given tolerance, the full Newton is applied with no damping.

3.3 Linear multigrid solver

The basic idea behind the success of multigrid is the efficiency of the basic solvers **(smoothers)** at damping the short wavelength error components. This requirement is fulfilled by basic iterative methods namely, Gauß-Seidel or Jacobi. Moreover the poor convergence of these basic iterative solvers for long wavelength error components is reduced by solving the original problem on different grids with the object to suppress the error components on different grids. Therefore, the main concept in the local MPSC approach is to solve **'exactly'** on patches and to perform an outer Gauß-Seidel iteration. This approach can be interpreted as generalization of block-Jacobi/Gauß-Seidel methods for saddle point problems which contains modifications of classical schemes like the Vanka smoother [103]. The necessary stabilization on anisotropic meshes can be obtained via adaptive patching.

To handle the arising enlarged stencil, due to jump terms in the edge-oriented stabilization, the local MPSC smoothers are modified. Firstly, by splitting the contributions from the new stabilization techniques with respect to matrix-vector multiplication and local assembling routines. Secondly, by decreasing the block size of block-Jacobi/Gauß-Seidel methods to contain only the degree of freedom that are connected with one edge instead of those which are connected with one element and use the full jump matrix. Furthermore the storage of the stiffness matrix is done with two strategies. Firstly, the stiffness matrix will only contains the partial stabilization matrix which fits into the same standard FEM data structure, while the complementary part can be assembled via elementwise operations only. Secondly, a special edge-oriented data structure is developed by extending the matrix to support the additional contributed elements.

3.3.1 Two level algorithm

The linearization and discretization of the generalized Navier-Stokes problem leads to a large saddle point problem (3.24) which can be rewritten in the following manner

$$A_N u_N = f_N. \tag{3.25}$$

Let us assume the existence of a hierarchy of levels $k = 1, ..., N$ associated with the triangulation $\mathcal{T}_{h_k}$ with mesh size h_k. On each level k the matrix A_k and the right-hand side f_k need to be assembled, the multigrid linear solver is described as follows:

The k^{th} level iteration $MG(k, z_0, g)$ of the multigrid algorithm with initial guess z_0 yields an approximation to z_k, the solution of

$$A_k z = g \tag{3.26}$$

One step can be described in the following way:
For $k = 1$ on the coarsest level, the direct solver is used

$$MG(1, z_0, g) = A_1^{-1} g. \tag{3.27}$$

- **Smoothing step $k > 1$:** let $z_l \in V_l (1 \leq l \leq m)$ be defined by

$$z_l = z_{l-1} + \Lambda_k{}^{-1} (g - A_k z_{l-1}) \;\; 1 \leq l \leq m \tag{3.28}$$

  where $\rho(\Lambda_k) \leq C h_k^{-2}$.
- **Correction step:** Let $\tilde{g} = I_k^{k-1}(g - A_k z_m)$ and let $g_i \in V_{k-1}$ be defined as

$$\begin{aligned} g_0 &= 0 \\ g_i &= MG(k-1, g_{i-1}, \tilde{g}) \;\; 1 \leq i \leq p. \end{aligned} \tag{3.29}$$

Final output:

$$MG(k, z_0, g) = z_m + I_{k-1}^k g_p. \tag{3.30}$$

The efficiency of the multigrid solver mainly depends on the efficiency of its components which are

(a) the matrix-vector multiplication routines for the operators $A_k, k \leq N$,

(b) the smoothers on finer levels and the coarse grid solver,

(c) the grid transfer operators: the prolongation I_{k-1}^k and the restriction I_k^{k-1}.

These ingredients of a multigrid solver incorporated with edge-oriented stabilization will be discussed in the next sections.

3.3.2 Sparsity of the matrix

Sparse matrices are an integral part of the finite element analysis for incompressible flow problems which may lead to huge and ill-conditioned systems for such Oseen-type problems so that very fast solvers of Krylov-space or particularly of multigrid type are required. In addition the introduced edge-oriented stabilization techniques destroy the typical local sparsity properties since this approach involves more than the adjacent elements as can be seen in Fig. 3.1 which shows the increased local support of the nonconforming basis functions: The corresponding rows and columns for the new stiffness matrices $\mathbf{J}$ may contain 25 nonzero matrix elements, in contrast to the usual 7 for the non-stabilized case in 2D and 61 nonzero matrix elements, in contrast to the usual 11 for the non-stabilized case in 3D.

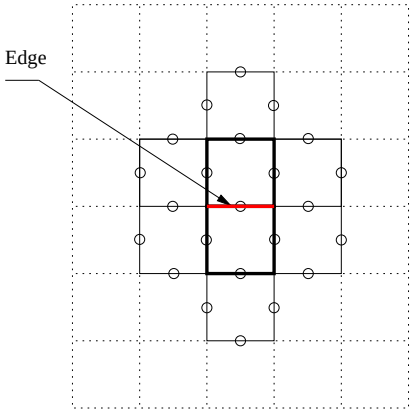

Fig. 3.1. Involved edges for each nonconforming basis function

3.3.3 Storage in the same FEM data structure

To overcome the problem of storing the new matrix $\mathbf{J}$ – coming from $\langle \mathbf{J}\boldsymbol{u}, \boldsymbol{v}\rangle$ – with regard to the standard FEM data structures, the matrix $\mathbf{J}$ is written as a sum of two matrices $\mathbf{J}^*$ and $\mathbf{J}_{rest}$,

$$\mathbf{J} = \mathbf{J}^* + \mathbf{J}_{rest} \tag{3.31}$$

where $\mathbf{J}^*$ has the same sparsity structure as the usual corresponding finite element matrix; then, $\mathbf{J}_{rest} = \mathbf{J} - \mathbf{J}^*$. Hence, $\mathbf{J}^*$ can be handled with the same linear algebra techniques which are typically used for the treatment of the standard nonconforming finite element approach; $\mathbf{J}_{rest}$ is the complementary part and will be used as a correction for the calculation of the residuals inside of the linear solvers only. Then, given any approximation $\boldsymbol{v}$ and $\mathbf{A}$ denoting the stiffness matrix without the new stabilization matrices, we can write the complete residual as:

$$\boldsymbol{f} - (\mathbf{A} + \mathbf{J})\boldsymbol{v} = \boldsymbol{f} - (\mathbf{A} + \mathbf{J}^*)\boldsymbol{v} - \mathbf{J}_{rest}\boldsymbol{v}. \tag{3.32}$$

Consequently, only the partial matrix $\mathbf{A} + \mathbf{J}^*$ is stored in the complete stiffness matrix so that the first part of the residual can be obtained via standard matrix-vector multiplication while the second part is assembled via elementwise operations. Moreover, the construction of preconditioners for the corresponding linear systems may only include parts of the (sub)matrix $\mathbf{A} + \mathbf{J}^*$, too, which will be explained in the following (see also [98] for more details).

3.3.4 Storage in a special edge-oriented data structure

A data structure for the storage of the stiffness matrix for edge-oriented stabilization is not common in FEM community. Fortunately, it is not difficult to develop one from the available FEM storage techniques. In fact, each edge E_i has two surrounding elements with n_i edges $(E_{i,j})_{j=1}^{n_i}$, then by the intermediate of the edges $(E_{i,j})_{j=1}^{n_i}$ the other contributed elements and edges $(E_{i,j_k})_{k=1}^{m_j}$ required for edge-oriented stabilization techniques are obtained (see Fig. 3.2). This is exactly the graph of the extended matrix: In fact, let the index i be assimilated to any matrix row and the index j be the corresponding nonzero columns in the standard FEM data structure, the extension will consist of the corresponding nonzero columns j_k to the rows j (see Fig. 3.2).

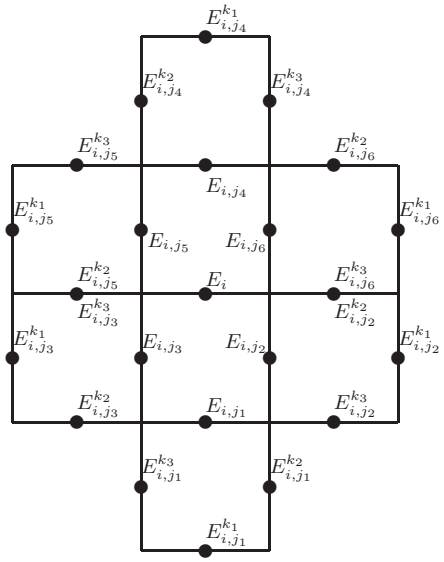

Fig. 3.2. An illustration for edge-oriented storage technique

Edge-oriented storage algorithm

Based on the standard Compressed Sparse Row CSR-FEM storage technique, let N_A be the number of entries in the matrix A, N_{Eq} be the number of equations, $P_c(N_A)$ vector with dimension N_A be the column pointer and $P_r(N_{Eq}+1)$ vector with dimension $N_{Eq}+1$ be the pointer row. Then, the edge-oriented storage technique is deduced from the standard FEM storage technique as following

$$\begin{aligned} \tilde{N}_A &= 1 \\ l_1 &= 1. \end{aligned} \tag{3.33}$$

For each $i = 1, .., N_{eq}$ the corresponding nonzero columns are given by the following nested loops

$$\tilde{P}_r(i) = l_i. \tag{3.34}$$

1. In standard FEM storage we get

$$i_j = P_c(l), \quad P_r(i) \le l \le P_r(i+1) - 1. \tag{3.35}$$

2. For each i_j the extension consists of the nonzero corresponding column in standard FEM storage which is given by

$$\begin{aligned} k_{i_j} &= P_c(l), \quad P_r(i_j) \le l \le P_r(i_j+1) - 1 \\ \tilde{N}_A &= \tilde{N}_A + 1 \\ l_i &= l_i + 1 \\ \tilde{P}_c(l_i) &= k_{i_j}. \end{aligned} \tag{3.36}$$

Here, $\tilde{N}_A$ denotes the number of entries in the matrix A, $\tilde{P}_r$ is the row pointer and $\tilde{P}_c$ is the column pointer in the edge-oriented storage.

3.4 Coupled multigrid solver

Coupled multigrid method or Local Pressure Schur complement schemes (see [59, 92]) compute the solution for velocity and pressure of (3.24) simultaneously. In the following, a details on the individual components of these schemes and how they were adapted to support the extended stencil arising from jump terms are presented.

3.4.1 The grid transfer operators

The multigrid method requires inter-grid transfer operators, but for nonconforming finite element approximations the finite element space of coarser level is not a subspace of the finite element space on a finer level: $V_{k-1} \nsubseteq V_k$. Therefore, the natural injection does not work and the restriction I_k^{k-1} from V_k to V_{k-1} must explicitly be constructed. This leads to what is known as non-nested multigrid methods. A simple scheme like piecewise linear interpolation and L^2-projection operator are popular candidates. The choice of each of these operators can have an immense effects on convergence rates.

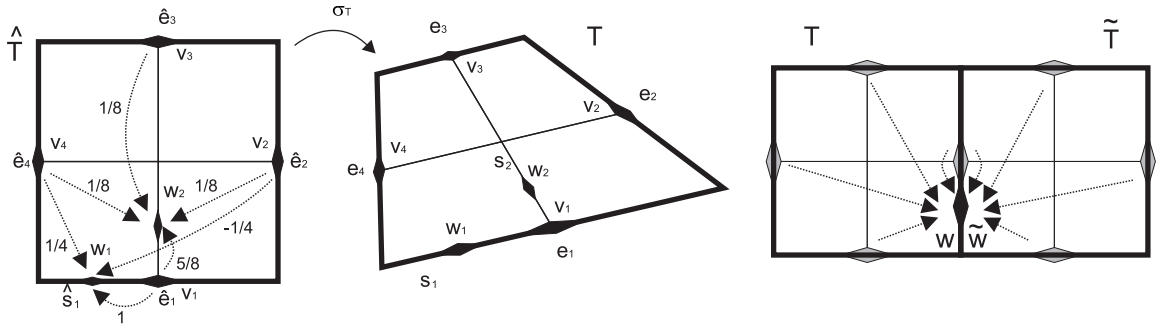

Fig. 3.3. Configuration for local grid transfer operators (from [57])

Adaptive prolongation for $\tilde{Q}_1$

The adaptive prolongation for the rotated $\tilde{Q}_1$ element calculates on all fine edges the corresponding interpolant values due to the given function v_{2h} which is defined via the coefficient $v_i, i = 1, .., 4$ (see Fig. 3.3). Let us introduce the Aspect-Ratio (AR): the ratio of largest to smallest dimension in an element, for instance one may use the following definition (for further details see [54, 55])

$$AR = \max\left(\frac{\|m_3 - m_1\|_{Eu}}{\|m_4 - m_2\|_{Eu}}, \frac{\|m_3 - m_1\|_{Eu}}{\|m_4 - m_2\|_{Eu}}\right), \tag{3.37}$$

where $\| \ \|_{Eu}$ is the Euclidean norm and $m_i, i = 1, .., 4$ are the midpoints of the quadrilateral element (see Fig. 2.2). Then, define the following options for the interpolation operator [92]

1. **Full interpolation:** If $AR \leq AR_0$ the full interpolation is used which reads:
   (a) mean-value on edges as degrees of freedom (d.o.f.)
   $$w_1 = v_1 + \tfrac{1}{4}v_2 + \tfrac{1}{4}v_4 \quad , \quad w_2 = \tfrac{5}{8}v_1 + \tfrac{1}{8}(v_2 + v_3 + v_4)$$
   (b) midpoint on edges as d.o.f.
   $$w_1 = \tfrac{15}{16}v_1 - \tfrac{3}{16}v_2 - \tfrac{1}{16}v_3 + \tfrac{5}{16}v_4 \quad , \quad w_2 = \tfrac{9}{16}v_1 + \tfrac{3}{16}v_2 + \tfrac{1}{16}v_3 + \tfrac{3}{16}v_4$$
2. **Constant interpolation:** If $AR > AR_0$ simply use the constant interpolation which reads:
   $$w_1 = v_1 \quad , \quad w_2 = v_1$$

For the values belonging to the "macro" edges w_1 (for instance in Fig. 3.3) one may take a mean-value by

(a) Simple averaging
$$\frac{w + \tilde{w}}{2} \tag{3.38}$$

(b) Weighted averaging
$$\frac{1}{|T| + |\tilde{T}|}(|T|w + |\tilde{T}|\tilde{w}). \tag{3.39}$$

It is recorded in Turek [92] that AR_0 should belong to the interval $(10, 100)$. For more numerical investigation we refer to [57].

3.4.2 Coarse grid discretization

Similar to the grid transfers, coarse grid discretization can be categorized in two categories. First, schemes that rediscretize the continuous operator using the application program on the coarse grid (FE approach). Second, methods which project automatically the fine grid discretization (e.g. Galerkin coarse grid operators) onto the coarse grid without requiring further consultation of the application (Galerkin approach).

3.4.3 The smoothers

Pressure Schur Complement Approach

The Pressure Schur Complement (PSC) matrix is obtained by elimination of the velocity first, then deduction of the equation for the pressure which acts as Lagrange multiplier for the incompressibility constraint for the saddle point problem (3.24). In fact, if the operator A is nonsingular, the velocity can be expressed as

$$\boldsymbol{u} = (\mathbf{A} + \mathbf{J})^{-1}(\mathbf{Res}_u - \tilde{\mathbf{B}}p) \tag{3.40}$$

and plugged into the discretized continuity equation

$$\mathbf{B}^T \boldsymbol{u} = \mathbf{Res}_p \tag{3.41}$$

which gives the scalar **Schur complement** equation for the pressure

$$\mathbf{B}^T(\mathbf{A}+\mathbf{J})^{-1}\tilde{\mathbf{B}}p = B^T(\mathbf{A}+\mathbf{J})^{-1}\mathbf{Res}_u + \mathbf{Res}_p. \tag{3.42}$$

Thus, the coupled system (3.24) can be handled as follows

1. Solve the Pressure Schur Complement (PSC) equation (3.42) for p.

2. Substitute p into relation (3.40) and compute the velocity $\boldsymbol{u}$.

Because of decoupling of velocity and pressure the use of the matrix $\mathbf{B}^*$ will be ineffective. Consequently, the idea of solving coupled small problems in an additive manner and perform an outer block Jacobi/Gauss-Seidel iteration is more attractive which leads to the so-called Local Pressure Schur Complement approach.

Local Pressure Schur Complement Approach

Local Pressure Schur complement schemes (see [59, 92]) as generalization of so-called Vanka smoothers [103] are simple iterative relaxation methods for such coupled systems (3.24) of saddle point type which are acting directly on element level and which are embedded into an outer block Jacobi/Gauss-Seidel iteration. The local character of this procedure together with a global defect-correction mechanism is crucial for our approach. If $\mathbf{Res}_u$ and $\mathbf{Res}_p$ denote the residuals for the (complete) discrete momentum and continuity equations which include the complete stabilization term due to $\mathbf{J}$ as described in (3.32). Then, two types of Vanka smoothers can be applied with respect to the decomposition of the domain Ω to a patches $\Omega_i, i = 1, ..., I$. This decomposition is not required to be disjoint.

Cell-oriented Vanka smoother

In this case the *patches* Ω_i may consist of only one element and the index I is the total number of elements, which means that the global stiffness matrix is restricted to the single cells/quadrilaterals of the mesh and, then the corresponding algebraic problem to be solved.

It is straightforward to deduce the element stiffness matrix from the global stiffness matrix as follows

$$K = \sum_{T \in \mathcal{T}_h} K_T \tag{3.43}$$

where K and K_T denote the global and element stiffness matrices respectively. It follows that

$$\begin{aligned}
[K_T]_{ij} &= \left[\mathbf{A}_{|T}\right]_{ij} + \left[\mathbf{J}_{|T}\right]_{ij} \qquad \text{for} \quad 1 \le i,j \le 4 \\
[K_T]_{i5} &= \left[\tilde{\mathbf{B}}_{|T}\right]_i \qquad \text{for} \quad 1 \le i \le 4 \\
[K_T]_{5i} &= \left[\mathbf{B}^T_{|T}\right]_i \qquad \text{for} \quad 1 \le i \le 4 \\
[K_T]_{55} &= 0.
\end{aligned} \tag{3.44}$$

With the standard FEM data structure (without the extension of the matrix) the contribution of the jump term will be restricted to $\mathbf{J}^*$. Then

$$[K^*_T]_{ij} = \left[\mathbf{A}_{|T}\right]_{ij} + \left[\mathbf{J}^*_{|T}\right]_{ij} \quad \text{for} \quad 1 \le i,j \le 4. \tag{3.45}$$

The basic iteration step which means one smoothing step can be described as follows:

$$\begin{bmatrix} \boldsymbol{u}^{n+1} \\ p^{n+1} \end{bmatrix} = \begin{bmatrix} \boldsymbol{u}^{n} \\ p^{n} \end{bmatrix} + \omega^n \sum_{T\in\mathcal{T}_h} \left[\tilde{K}_T^*\right]^{-1} \begin{bmatrix} \mathbf{Res}_u(u^n, p^n) \\ \mathbf{Res}_p(u^n, p^n) \end{bmatrix}_{|T} \tag{3.46}$$

where the matrix $\tilde{K}_T^*$ is easily invertible and remains close to K_T^*. Related to the choice of the matrix $\tilde{K}_T^*$ two types of Vanka smoothers are prescribed, namely diagonal Vanka smoother and full Vanka smoother.

(a) *Diagonal Vanka smoother:* The diagonal Vanka smoother updates the velocity and the pressure values connected to the element T by

$$\begin{bmatrix} \boldsymbol{u}^{n+1} \\ p^{n+1} \end{bmatrix} = \begin{bmatrix} \boldsymbol{u}^{n} \\ p^{n} \end{bmatrix} + \omega^n \sum_{T\in\mathcal{T}_h} \left[\mathrm{diag}(K_T^*)\right]^{-1} \begin{bmatrix} \mathbf{Res}_u(u^n, p^n) \\ \mathbf{Res}_p(u^n, p^n) \end{bmatrix}_{|T}. \tag{3.47}$$

(b) *Full Vanka smoother:* The full Vanka smoother updates the velocity and the pressure values connected to the element T by

$$\begin{bmatrix} \boldsymbol{u}^{n+1} \\ p^{n+1} \end{bmatrix} = \begin{bmatrix} \boldsymbol{u}^{n} \\ p^{n} \end{bmatrix} + \omega^n \sum_{T\in\mathcal{T}_h} \left[K_T^*\right]^{-1} \begin{bmatrix} \mathbf{Res}_u(u^n, p^n) \\ \mathbf{Res}_p(u^n, p^n) \end{bmatrix}_{|T}. \tag{3.48}$$

As can be seen, for the preconditioning step only parts of the matrix (here: $\mathbf{A}+\mathbf{J}^*$) are involved while the residual contains all parts of the matrix. Consequently, when this approach converges, the result is the solution of the stabilized version while the preconditioning steps only determine the speed of the overall iteration procedure.

Edge-oriented Vanka smoother

To incorporate the full jump $\mathbf{J}$ into the preconditioning step let us consider the so-called ***edge-oriented patches*** Ω_i which consist of the neighboring element sharing the same edge:

$$\Omega_i = \cup \{T, T \in \mathcal{T}_h \wedge \cap_{T\in\mathcal{T}_h} = E_i\}. \tag{3.49}$$

Here, I is the total number of edges. This will keep the size of the local problem small and the full matrix $\mathbf{J}$ will be used for the preconditioning steps.

The extension of the matrix to support the jump term leads to a 5×5 FEM matrix block of the type (3.44). To keep the size of the local problem small the element matrix is disassembled to its edge contributions [22]

$$K_T = \sum_{i=1}^{m} K_T^{E_i} \tag{3.50}$$

where $K_T^{E_i}$ is the contribution of the edge E_i to K_T and m is the number of the edges on the cell T.

From the definition of edge-oriented patches (3.49), the edge stiffness matrix may contain the contributions of all sharing elements

$$K^{E_i} = \sum_{T\in\Omega_i} K_T^{E_i} = K_{\Omega_i}^{E_i}. \tag{3.51}$$

Then, one basic iteration can be described as follows

$$\begin{bmatrix} \boldsymbol{u}^{n+1} \\ p^{n+1} \end{bmatrix} = \begin{bmatrix} \boldsymbol{u}^{n} \\ p^{n} \end{bmatrix} + \omega^n \sum_{i\in I} \left[K_{\Omega_i}^{E_i}\right]^{-1} \begin{bmatrix} \mathbf{Res}_u(u^n, p^n) \\ \mathbf{Res}_p(u^n, p^n) \end{bmatrix}_{|\Omega_i}. \tag{3.52}$$

This blocking strategy is different from that used in [82, 92] to generate isotropic subdomains for stabilizing strong mesh anisotropy. Indeed, for the edge-oriented patches the number of block matrices is only depending on the number of edges and not on the number of patches itself.

In 3d one may consider to use the face-oriented patches which should be enough for the rotated $\tilde{Q}_1$ element, but for elements with unknown components along the edges one may then consider the edge-oriented patches. The edge-based FEM data structure was used earlier to improve the computational efficiency, for details see for instance [22, 64, 77].

The global defect restricted to a single patch Ω_i is given by

$$\begin{bmatrix} \mathbf{Res}_u(u^n, p^n) \\ \mathbf{Res}_p(u^n, p^n) \end{bmatrix}_{|\Omega_i} = \left(\begin{bmatrix} \mathsf{L} + \tilde{\mathsf{N}} + \mathsf{J} & \mathsf{B} \\ \mathsf{B}^T & 0 \end{bmatrix} \begin{bmatrix} \boldsymbol{u}^n \\ p^n \end{bmatrix} - \begin{bmatrix} \mathbf{f} \\ 0 \end{bmatrix} \right)_{|\Omega_i}. \tag{3.53}$$

In practice the following auxiliary problem

$$\begin{bmatrix} K_{\Omega_i}^{E_i} \end{bmatrix} \begin{bmatrix} \boldsymbol{v}_i^{n+1} \\ q_i^{n+1} \end{bmatrix} = \begin{bmatrix} \mathbf{Res}_u(u^n, p^n) \\ \mathbf{Res}_p(u^n, p^n) \end{bmatrix}_{|\Omega_i} \tag{3.54}$$

is solved and then the new iterates $\boldsymbol{u}^{n+1}$ and p^{n+1} are computed

$$\begin{bmatrix} \boldsymbol{u}^{n+1} \\ p^{n+1} \end{bmatrix} = \begin{bmatrix} \boldsymbol{u}^n \\ p^n \end{bmatrix} + \omega^n \sum_{i \in I} \begin{bmatrix} \boldsymbol{v}_i^{n+1} \\ q_i^{n+1} \end{bmatrix}. \tag{3.55}$$

The resulting local MPSC method corresponds to a simple block-Jacobi iteration for the mixed problem (3.24) and to a block-Gauss-Seidel method by using the updated solution for the computation of the local defect (3.53).

3.5 Uniqueness of the problem

The question of uniqueness of the stationary problem (1.6) is not trivial to solve. Hron et al. [45] showed that non-unique solutions are possible for fluids flows with pressure dependent viscosity. Generally, the complete closure of equations in an incompressible fluids can be achieved by fixing the pressure in the following way

$$\int_\Omega p dx = C \tag{3.56}$$

In contrast to the standard Navier-Stokes equations, the viscosity in equations (1.6) depends on the pressure and the effect of the choice of the constant C in (3.56) is not negligible. The following Table 3.1 shows the influence of variation of the constant C on the global solution.

Table 3.1. The effect of fixing the pressure on the global solution

$\nu(\boldsymbol{u}, p) = exp(\beta p), \beta = 10^{-1}$				
C	0	2	4	6
$\|\nu\|_\infty$	0	3.31×10^{-1}	7.31×10^{-1}	13.80×10^{-1}
$\|\boldsymbol{u}\|_\infty$	0	2.07×10^{-4}	4.72×10^{-4}	8.15×10^{-4}

The results of Table 3.1 lead one to think of an appropriate physical choice. Franta et al. in [31] considered a slightly compressible flow

$$\epsilon \Delta p^{\epsilon} + \epsilon p^{\epsilon} + \operatorname{div} \boldsymbol{u}^{\epsilon} = 0 \quad \text{in } \Omega \quad , \quad \frac{\partial p^{\epsilon}}{\partial \boldsymbol{n}} = 0 \quad \text{on } \partial\Omega. \tag{3.57}$$

For the same reason Tardos et al. [89] introduced the so-called normality condition in the frame of compressible granular material which can be generalized as follows

$$\nabla \cdot \boldsymbol{u} = \frac{\partial \nu \left(\frac{1}{2} \operatorname{tr}(\mathbf{D} - \frac{1}{2} \nabla \cdot \boldsymbol{u} I)^2, p \right)}{\partial p}. \tag{3.58}$$

In orther to examine the behavior of the linear solver, the matrix of the linear problem is written in the following form

$$M_{\delta_p, \tilde{\delta}_p}(\tilde{\boldsymbol{u}}, \tilde{p}) = \begin{pmatrix} \mathbf{A} + \mathbf{J} & \mathbf{B} + \delta_p \mathbf{B}^* \\ \mathbf{B}^T + \tilde{\delta}_p \mathbf{B}^{*T} & 0 \end{pmatrix}. \tag{3.59}$$

The nullspace of the the matrix $M_{\delta_p,0}$ is nontrivial and dependent on the solution itself. The introduction of the term $\tilde{\delta}_p \mathbf{B}^{*T}$ is motivated by the work of Franta et al. [31] and Tardos et al. [89] in order to not impose any condition on the pressure. This has no effect on the solution since the matrix $M_{\delta_p, \tilde{\delta}_p}$ is used only for preconditioning. Table 3.2 summarize the multigrid behavior of the linear problem with and without the fixation of the pressure.

Table 3.2. The convergence rate of F-cycle multigrid type with and without the fixation of the pressure

Level/ β	1×10^{-4}	1×10^{-3}	1×10^{-2}	1×10^{-1}
	convergence rate for the matrix $M_{0,0}$			
3	0.22	0.22	0.14	0.26
4	0.23	0.24	0.23	0.36
5	0.26	0.25	0.24	0.37
	convergence rate for the matrix $M_{1,0}$			
3	0.22	0.22	0.15	0.27
4	0.23	0.24	0.23	0.37
5	0.26	0.25	0.24	0.38
	convergence rate for the matrix $M_{1,1}$			
3	0.22	0.22	0.15	0.27
4	0.23	0.24	0.23	0.44
5	0.26	0.25	0.24	0.50

The multigrid convergence shows excellent behavior with and without fixing the pressure with the eventual consideration of slightly compressible model. So, the linear solver is ready to handle both compressible and incompressible flow with the same efficiency.

3.6 Numerical results

Let us present some results from numerical experiments with different physical models in which the computational domain is the channel geometry with an obstacle as shown in Fig. 3.4.

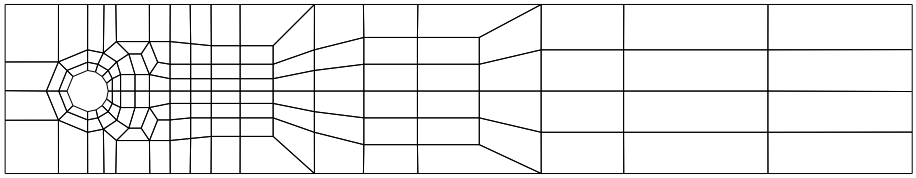

Fig. 3.4. The coarse mesh for flow around cylinder benchmark

On the boundaries, we prescribe no-slip conditions on the walls and on the cylinder while a parabolic inflow profile is defined on the upstream boundary. At the downstream part, we prescribe natural boundary conditions (see [41]) which leads to the well-known outflow boundary condition $\nu \mathbf{D}(u) \cdot \boldsymbol{n} - p\boldsymbol{n} = 0$. An extensive analysis of the asymptotically precise estimates for the truncation error for linear and nonlinear problem with small data can be found in [85, 6].

3.6.1 Numerical study of the accuracy

First of all, we want to check if the new stabilization term $\mathbf{J}$ preserves the accuracy of the nonconforming finite element in CFD simulations. Therefore, we calculate in Table 3.3 the corresponding lift and drag forces acting on the cylinder for different Reynolds numbers (here: for different viscosity parameters ν) and different formulations (gradient, tensor and stabilized tensor formulation). Table 3.3 only shows the results on level 5 (after 4 successive refinements of the given coarse mesh) since no major differences occur for finer or coarser meshes; we choose $\gamma = 0.5$.

Table 3.3. Lift and drag forces

$1/\nu$	force	Gradient	Tensor	Stab. Tensor
1	lift	0.31252×10^4	0.31221×10^4	0.31231×10^4
	drag	0.30898×10^2	0.30924×10^2	0.30936×10^2
10	lift	0.31258×10^3	0.31227×10^3	0.31237×10^3
	drag	0.36832×10^1	0.36851×10^1	0.36864×10^1
100	lift	0.32016×10^2	0.31981×10^2	0.31990×10^2
	drag	0.79786×10^0	0.79758×10^0	0.79770×10^0
1000	lift	0.55657×10^1	0.55531×10^1	0.55535×10^1
	drag	0.10180×10^{-1}	0.10259×10^{-1}	0.10277×10^{-1}

In addition, we give the corresponding approximation results when we approximate a prescribed polynomial solution for u and p.

Surprisingly, we do not see any significant difference between the different formulations! The discussed kernel function and hence the failure of Korn's inequality has - more or less - no visible influence on the approximation properties which is understandable in our case of (partial) Dirichlet boundary conditions:

Table 3.4. L^2- and H^1-errors for a given polynomial solution

Level	Norm	Tensor	Stabilized Tensor
3	$\|u-u_h\|_1$	$0.1878073305586 \times 10^{0}$	$0.1890389708704 \times 10^{0}$
	$\|u-u_h\|_0$	$2.1924276705200 \times 10^{-2}$	$2.2278915655013 \times 10^{-2}$
4	$\|u-u_h\|_1$	$9.3418000771639 \times 10^{-2}$	$9.3755096686689 \times 10^{-2}$
	$\|u-u_h\|_0$	$5.4160542751463 \times 10^{-3}$	$5.4675714354466 \times 10^{-3}$
5	$\|u-u_h\|_1$	$4.6624024860649 \times 10^{-2}$	$4.6711662913404 \times 10^{-2}$
	$\|u-u_h\|_0$	$1.3482613994813 \times 10^{-3}$	$1.3552529532575 \times 10^{-3}$
6	$\|u-u_h\|_1$	$2.3298314874403 \times 10^{-2}$	$2.3320634187601 \times 10^{-2}$
	$\|u-u_h\|_0$	$3.3659558203381 \times 10^{-4}$	$3.3750809473889 \times 10^{-4}$

Then, no 'free' rigid body movement can occur. However, as the following calculations will show, the problem with Korn's inequality is clearly visible if we look at the corresponding behavior of the (multigrid) solvers.

3.6.2 Numerical study of the influence of the convection

The following numerical experiments investigate the influence of the convective term. For this purpose we increase the Reynolds number and list the number of resulting nonlinear iterations (NNL) and the averaged number of multigrid sweeps per nonlinear iteration (AVMG). Table 3.5 shows that increasing the Re number leads to 'improvements' for the multigrid solver for the (unstabilized) deformation tensor formulation (keep in mind that the case of $1/\nu = 1000$ corresponds to $Re = 20$ only, compare with the settings for the 'DFG-Benchmark' [100]). However, in the case of very low Re numbers, the failure of Korn's inequality gets clearly visible since the averaged number of linear multigrid sweeps AVMG has to be massively increased to satisfy a desired stopping criterion.

Table 3.5. Nonlinear iterations (NNL)/Averaged multigrid sweeps (AVMG) per nonlinear iteration for different Re numbers ($1/\nu$), various formulations (gradient, deformation tensor, stabilized tensor (stab. tensor 1) with diagonal 'Vanka smoother' and stabilized tensor (stab. tensor 2) with modified full 'Vanka smoother'), several levels of refinement (LEV) and varying number of smoothing steps (NSM)

$1/\nu$		1				1000 (Re=20)			
formulation		gradient	tensor	stab.	stab.	gradient	tensor	stab.	stab.
LEV	NSM	form.	form.	tensor 1	tensor 2	form.	form.	tensor 1	tensor 2
3	2	3/5	4/57	3/7	3/6	10/7	10/6	10/7	10/7
	4	3/3	4/29	3/4	3/3	10/5	10/5	10/5	10/5
4	2	3/6	4/167	3/7	3/6	11/6	11/10	11/5	11/5
	4	3/3	4/86	3/4	3/3	11/4	11/5	10/4	11/4
5	2	3/7	4/478	3/7	3/6	12/5	12/23	12/4	12/4
	4	3/4	4/231	3/4	3/4	12/4	12/10	12/4	12/4
6	2	3/9	6/382	3/16	3/7	12/4	12/4	12/4	12/4
	4	3/5	5/326	3/8	3/4	12/3	12/3	12/3	12/3

The main result is that for Re numbers of moderate size ($Re \geq 10$) the presence of the convective term seems to stabilize the multigrid behavior since the influence of the kernel function due to the deformation tensor formulation is weakened. However, since the corresponding 'elliptic' differential operator - being of second order - is the dominating operator for small mesh width, we can see that the convergence behavior deteriorates with finer mesh widths. This can be shown much better in the case of very small Re numbers ('Stokes' case) where the multigrid convergence behavior is extremely mesh dependent so that the multigrid solver looses all favorable properties. In contrast, the introduced edge-oriented stabilization techniques together with the described multigrid smoothers and data structures lead to significant improvements so that no differences between 'stable' gradient formulation and stabilized tensor formulation are visible.

However, we also have to remark that the inclusion of the partial matrix $\mathbf{J}^*$ into the preconditioning matrix $\mathbf{A} + \mathbf{J}^*$ is necessary. It might appear to be much easier for the implementation procedure to employ only the partial matrix $\mathbf{A}$ in the preconditioning step since this approach does not require any modification of the 'Vanka smoother'; only the defect calculation has to be adapted. However, in this case, the solver behaves more like an (incomplete) block-Jacobi iteration so that convergence problems may arise as soon as significant mesh anisotropies occur. Therefore, we strongly recommend to include the partial matrix $\mathbf{J}^*$ from the stabilization procedure into the preconditioning approach.

3.6.3 Numerical study of stabilization parameter size

Non-Newtonian case: Shear-dependent viscosity

In the next simulations, let us consider the case of non-Newtonian flow in which we employ the standard *Power Law* model for the viscosity function ν. However, we are confronted with the question of how to choose a value for ν, and also for $\mathbf{D}(\boldsymbol{u})$ due to $\nu = \nu(D_{\mathrm{II}}(\boldsymbol{u}))$ on the edges of the mesh cells which is required in the edge-oriented stabilization approach. In the following, we prescribe $\nu(D_{\mathrm{II}}(\boldsymbol{u})) = \nu_0(\epsilon + D_{\mathrm{II}}(\boldsymbol{u}))^{\frac{r}{2}-1}$ which leads to 'shear-thickening' ($\frac{r}{2} - 1 \geq 0$) or 'shear-thinning' ($\frac{r}{2} - 1 \leq 0$). For the special parameter choices $\epsilon = 10^{-1}, \nu_0 = 1$ and $|\frac{r}{2} - 1| = 0.35$, the viscosity function ν varies locally by a factor of 10 ($\frac{r}{2} - 1 = 0.35$) or even 30 ($\frac{r}{2} - 1 = -0.35$). Figure 3.5 shows corresponding plots of the resulting viscosity function $\nu(D_{\mathrm{II}}(\boldsymbol{u}))$ for the converged solution $\boldsymbol{u}$ of these nonlinear problems.

Looking at this locally changing behavior of the viscosity function, the question arises of how to choose the stabilization parameters $\gamma \cdot \nu$ in (2.42) on each edge. Table 3.6 shows results for the version ν_{const} in this case ν was fixed to be the minimum value of the (global) viscosity. In contrast, the approach ν_{local} is based on the local size of the viscosity ν on every edge and takes into account the local variations due to changes with respect to the value of $D_{\mathrm{II}}(\boldsymbol{u})$. As expected, the locally adapted choice ν_{local} shows a better nonlinear convergence behavior (number of nonlinear iterations NL), and the corresponding linear multigrid behavior (averaged number of multigrid sweeps per nonlinear cycle AVMG) is significantly better, due to a possible underestimation of the value ν_{const} in the stabilization procedure; the case of no stabilization at all shows the expected problems due to the failure of Korn's inequality.

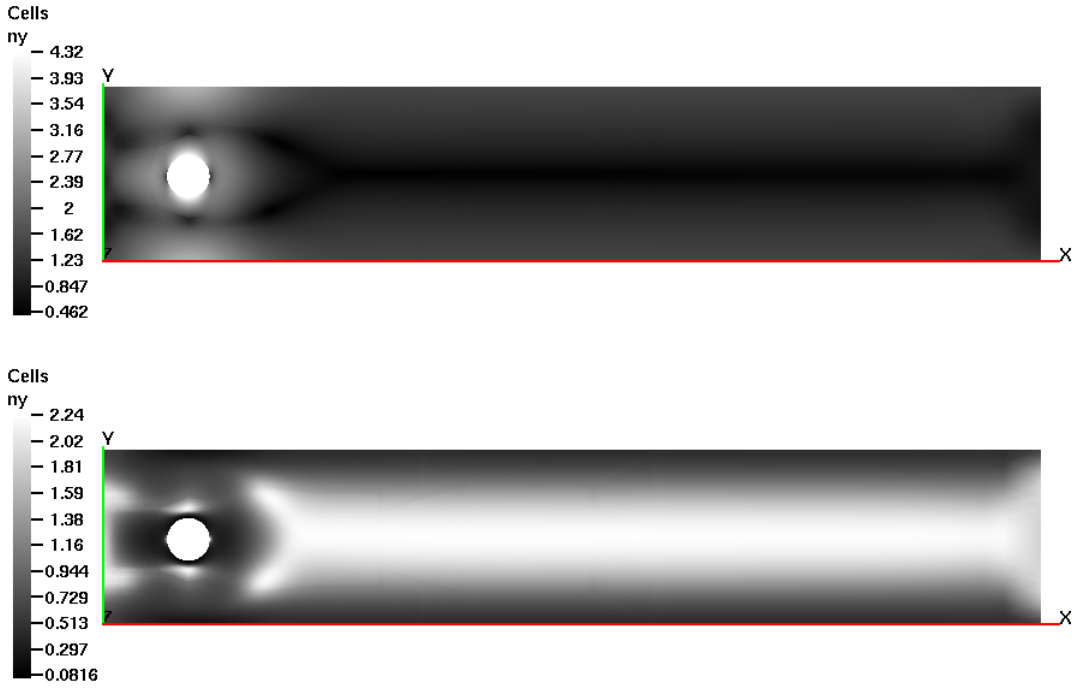

Fig. 3.5. The resulting viscosity for the described cases of shear thickening/thinning

Additionally, we discuss the aspect of selecting the appropriate stabilization parameter γ in $\gamma \cdot \nu_{const}$, respectively, $\gamma \cdot \nu_{local}$. The results in Table 3.6 demonstrate again the improved behavior of the locally adaptive stabilization parameter ν_{local}, and that γ can be chosen from a quite wide range.

Table 3.6. NL/AVMG for different choices of stabilization ($\epsilon = 10^{-1}, \nu_0 = 1$) for $\nu = \nu_0(\epsilon + D_{II}(\boldsymbol{u}))^{\frac{r}{2}-1}$

	$\frac{r}{2}-1=-0.35$			$\frac{r}{2}-1=0.35$		
Level	no stab	ν_{const}	ν_{local}	no stab	ν_{const}	ν_{local}
3	26/48	24/4	24/3	17/7	17/6	17/5
4	26/140	25/5	25/3	18/15	17/8	17/5
5	27/414	24/6	24/3	50/212	17/10	17/5
6	–	24/7	24/3	–	17/12	17/5
			level 4			
γ	0.1	0.01	0.001	0.1	0.01	0.001
$\gamma \cdot \nu_{const}$	25/4	25/11	25/15	17/6	17/14	17/27
$\gamma \cdot \nu_{local}$	25/3	25/3	25/8	17/5	17/10	17/23

3.6.4 Efficiency of the nonlinear solver: Pressure and shear dependent viscosity

Finally, let the nonlinear (pseudo) viscosity has the form $\nu(p,z) = \frac{\exp(\beta p)}{\epsilon + \|\mathbf{D}\|}$, and list the number of resulting nonlinear iterations and the averaged number of multigrid sweeps per nonlinear iteration for both Newton and Fixpoint methods. Table 3.7 shows that the presence of the new linear operator $\mathbf{B}^*$ cannot be ignored; otherwise, we destroy the efficiency of the Newton method which is necessary for the robust treatment of the significant nonlinearity.

Table 3.7. Corresponding results for the number of nonlinear iterations and the averaged number of linear sweeps per nonlinear cycle (couette configuration see figure 6.2).

$\nu(z,p) = \frac{\exp(\beta p)}{\epsilon + \|\mathbf{D}\|}$		Fixpoint		Newton $\delta_p = 0.0$		Full Newton	
Level	β	0.5	1.0	0.5	1.0	0.5	1.0
4	grad. tensor	35/2	38/2	14/2	34/2	11/2	11/2
5	grad. tensor	49/2	55/2	13/2	25/2	10/3	10/3
4	stab. tensor	13/2	18/2	11/2	18/2	8/2	8/2
5	stab. tensor	15/2	23/2	12/2	27/2	8/3	9/3

3.7 Concluding remarks and outlook

The aim of this chapter was to highlight the flexibility, robustness and efficiency of multigrid solvers for stabilized nonconforming finite element discretization to simulate general incompressible flow problems involving the deformation tensor. Based on the work by Brenner [9] and Hansbo and Larson [39] who have introduced and analyzed appropriate edge-oriented stabilization techniques by discontinuous Galerkin approaches in the context of Nitsche's method. The investigation has been concentrated on the corresponding (multigrid) solver and aspects of appropriate data structures to include these discretization techniques in standard FEM codes. The results are very promising and show that the typical efficiency of multigrid solvers for the gradient formulation can be transferred to formulations including the deformation tensor. The major task was to modify the existing local Multilevel Pressure Schur Complement smoothers ('Vanka smoother') [92] in the framework of defect correction approaches and to split the contributions from the new stabilization techniques with respect to matrix-vector applications and local assembling routines.

Additionally, the nonlinear viscosity flow models for both cases pressure and shear dependent viscosity has been successfully treated. Since in that case the corresponding viscosity function $\nu = \nu(D_{II}(u), p)$ depends on the solution $(\boldsymbol{u}, p)$ itself, the corresponding stabilization parameter has to be locally adapted since the resulting (local) viscosity ν exhibits significant changes of several orders of magnitude. Nevertheless, the new stabilization techniques lead to very robust and accurate approximation results

- The full Newton method seems to be necessary for this type of nonlinear problem.
- The multigrid convergence for this new class of auxiliary linear subproblems shows the typical excellent convergence behavior.

Altogether, appropriate discretization and solution concepts for nonconforming finite elements have been realized which are able to simulate more complex flow models including the deformation tensor formulation for general viscosities and configurations. Nevertheless, further research is required on the following aspects:

- Improved locally adaptive stabilization parameters which take into account the quantitative changes due to the nonlinear solution behavior.
- Better nonlinear Newton-like solvers which are adapted to the additional nonlinearity due to the nonlinear stabilization parameters.
- More robust and efficient smoothing operators which use the full jump matrix **J** by using the proposed edge-oriented Vanka smoother.
- Beside the nonlinear solution procedure, more investigation should focus on the linear algebraic problem due to the involved pressure for both Fixpoint and Newton methods.

4

A Computational Comparison of two FEM Solvers

This chapter compares the two different FEM discretization techniques (conforming Q_2/P_1, nonconforming $\tilde{Q}_1/Q_0$ elements) and solution procedures (various nonlinear Newton variants and multigrid versus Krylov-space solvers for the linear subproblems) onto the approximation properties and particularly the total efficiency of corresponding simulation tools for incompressible fluids. We discuss algorithmic details and give numerical results for laminar incompressible flow examples including Newtonian and non-Newtonian behavior of *Power Law* type (1.3).

4.1 Introduction

The Stokes element Q_2/P_1, being potentially of 3^{rd} order accuracy due to the biquadratic polynomials for the velocity (and the linear pressure approximation), is one of the most popular discretization techniques in the CFD community [11, 47]. In most applications, it is employed in a fully coupled approach which applies an outer Newton-like iteration for the discretized Navier-Stokes equations while the resulting linear subproblems of Oseen-type (as a nonsymmetric generalization of Stokes problems) are treated with (single-grid) Krylov-space methods: Due to the indefinite and particularly nonsymmetric character of the equations, preconditioned BICGSTAB [101] and GMRES [78] variants are the most popular solvers for the corresponding linear systems.

As an alternative, see for instance the realization in the FEATFLOW software package [91], special nonconforming FEM elements like the rotated multilinear/piecewise constant $\tilde{Q}_1/Q_0$ Stokes element have been developed which provide an optimal approximation error of one order less. However, for such finite elements, special hierarchical multigrid techniques have been realized which show a much more efficient behavior with respect to the solution of the resulting huge linear systems.

While such 'linear' (low order) finite elements seem to require much more degrees of freedom to satisfy a prescribed accuracy than compared with the quadratic Q_2/P_1 ansatz, they show at the same time a much superior behavior with respect to the efficiency of the involved solvers. Therefore, the aim of this chapter is to analyze the numerical characteristics of both popular approaches and to give a comparison for non-trivial flow configurations in 2D which are based on the (nonlinear) incompressible Navier-Stokes equations: 'What is the total efficiency in terms of CPU timing, if we take into account the different numbers of unknowns and iteration steps which are required for a comparatively accurate simulation?'

4.2 Linear Solvers

Here we give a brief description of the involved solution techniques for the resulting linear systems. For the nonconforming Stokes element $\tilde{Q}_1/Q_0$, a 'local pressure Schur complement' preconditioner (see section 3.4 and [92]) as generalization of so-called 'Vanka smoothers' (see [103]) is constructed on patches Ω_i which are ensembles of one single or several mesh cells, and this local preconditioner is embedded as global smoother into an outer block Jacobi/Gauss-Seidel iteration which acts directly on the coupled systems of Stokes, respectively of Oseen type. Other components in the multigrid approach, that means intergrid transfer, coarse grid correction and coarse grid solver, are quite standard and are based on the underlying hierarchical mesh hierarchy and the properties of the nonconforming finite elements [92].

For the biquadratic conforming Stokes Element Q_2/P_1, a standard GMRES method [78] as typical iterative single grid solver with ILU preconditioning is applied. The preconditioner is taken from the library developed in [8]. It is clear that multigrid might be preferable, too, but up to now, corresponding Vanka-like smoothers for this Q_2/P_1 ansatz are not yet available. Anyway, this GMRES solver is probably the most common approach in the CFD community, besides using BiCGSTAB [101], such that it will be very interesting to perform these comparisons.

4.3 Numerical Comparisons

Now we present the results from our numerical experiments with various parameters settings and also different physical models for the both proposed discretization and solution frameworks. The computational domain is always a channel geometry with an interior circle as shown via the coarsest mesh in Table 4.1; this configuration is following the standard CFD benchmark 'Flow around a cylinder' [100]. The reader should know the position of the circle is slightly nonsymmetric with respect to the height such that the lift coefficient is non-homogeneous.

Table 4.1. Coarse mesh and geometrical details for the 'Flow around a cylinder' configuration for the both elements $\tilde{Q}_1/Q_0$ and Q_2/P_1 on the different levels of mesh refinement.

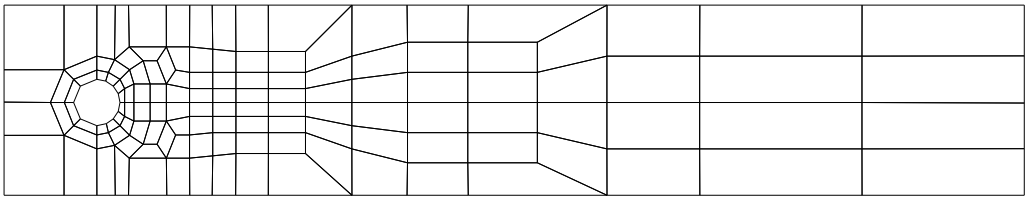

	Mesh information			$\tilde{Q}_1/Q_0$	Q_2/P_1
Level	Elements	Vertices	Midpoints	Total unknowns	Total unknowns
1	156	130	286	702	1 533
2	572	520	1 092	2 686	5 927
3	2 184	2 080	4 264	10 608	23 295
4	8 528	8 320	16 848	42 016	92 351
5	33 696	33 280	66 976	16 7232	367 743
6	133 952	133 120	267 072	66 7264	–

4.3.1 Newtonian test case

The first computational tests are performed for the Newtonian Navier-Stokes equations, i.e. with constant viscosity, in this case the only source of nonlinearity is the convective term. To remain in the limit of steady flows, the Reynolds number - by variations of the viscosity parameter only - is kept to be less than $Re = 50$ which is near the critical point to turn into (periodically) oscillating flow behavior. Although the cases $Re = 20$ (the standard test in [100]) and also $Re = 50$ appear to be far away from transport-dominated flows, nevertheless the involved convective term requires special treatment: While the simulations show that the approximation results for such 'medium' Reynolds numbers seem to be the best for no stabilization at all, that means applying central differencing or the pure Galerkin formulation, the involved multigrid routines are much more sensitive. Therefore, in the case of the rotated bilinear nonconforming Stokes element $\tilde{Q}_1/Q_0$, we apply the two standard techniques of streamline-diffusion (SD) and upwind (UPW) stabilization (see [92] for details of the discretization). However, such methods require additional 'free' parameters as the local mesh width, the relation to the local Re number and an additional relaxation parameter, which lead to the non-trivial task of parameter tuning, particularly in the case of nonlinear flow models and/or on non-uniform meshes. In contrast, the conforming Q_2/P_1 element is employed - as usually - without any stabilization which seems to be sufficient in our case of low up to medium Re numbers. However, we also have to state that, up to now, it is by far not clear of how to develop corresponding stabilization techniques which can be adapted to the potentially available higher order accuracy of this Stokes element in the case of much larger Re numbers.

The following tables show the resulting approximation properties with respect to the measured drag and lift coefficients on the different refinement levels, the required nonlinear iteration numbers #NN to gain 8 digits of accuracy (here we compare the continuous, respectively discrete Newton solvers with the simpler fixpoint approach) and the corresponding averaged number #NL of linear iterations per nonlinear cycle to gain 2 digits. We apply the described multigrid solver for the $\tilde{Q}_1/Q_0$ element, while for the conforming Q_2/P_1 element, the preconditioned GMRES solver has been used. These approximation and solution properties are shown with the corresponding CPU times.

Table 4.2. Drag coefficient (top) and lift coefficient (below) for different Re numbers and for various levels of mesh refinement for the $\tilde{Q}_1/Q_0$ (with streamline-diffusion and upwinding for the stabilization of the convective term) and the Q_2/P_1 approach (with no stabilization at all).

Level	Stokes	$Re = 20$	$Re = 50$
		$\tilde{Q}_1/Q_0$ - SD - Drag	
3	3.0231×10^3	6.3836×10^0	4.4529×10^0
4	3.0991×10^3	5.9574×10^0	3.9194×10^0
5	3.1251×10^3	5.7269×10^0	3.8728×10^1
6	3.1349×10^3	5.6285×10^0	3.7629×10^0
		$\tilde{Q}_1/Q_0$ - UPW - Drag	
3	3.0231×10^3	4.6383×10^0	4.4529×10^0
4	3.0991×10^3	5.9574×10^0	3.7409×10^0
5	3.1252×10^3	5.5657×10^0	3.6970×10^0
6	3.1349×10^3	5.5721×10^0	3.6922×10^0
		Q_2/P_1 - central - Drag	
2	3.1237×10^3	5.5569×10^0	3.6677×10^0
3	3.1374×10^3	5.5728×10^0	3.6867×10^0
4	3.1411×10^3	5.5777×10^0	3.6925×10^0
5	3.1421×10^3	5.5791×10^0	3.6940×10^0
		$\tilde{Q}_1/Q_0$ - SD - Lift	
3	2.9877×10^1	1.1740×10^{-3}	-1.6618×10^{-2}
4	3.0734×10^1	4.3426×10^{-3}	-1.2063×10^{-2}
5	3.0898×10^1	7.8140×10^{-3}	-1.1941×10^{-2}
6	3.0907×10^1	9.4495×10^{-3}	-1.1459×10^{-2}
		$\tilde{Q}_1/Q_0$ - UPW - Lift	
3	2.9871×10^1	4.8388×10^{-3}	-1.3512×10^{-2}
4	3.0733×10^1	9.1197×10^{-3}	-1.0155×10^{-2}
5	3.0898×10^1	1.0170×10^{-2}	-1.0173×10^{-2}
6	3.0907×10^1	1.0428×10^{-2}	-1.0775×10^{-2}
		Q_2/P_1 - central - Lift	
2	2.9854×10^1	0.9512×10^{-2}	-1.1764×10^{-2}
3	3.0578×10^1	1.0609×10^{-2}	-1.0894×10^{-2}
4	3.0788×10^1	1.0616×10^{-2}	-1.0739×10^{-2}
5	3.0846×10^1	1.0617×10^{-2}	-1.0730×10^{-2}

Table 4.3. Corresponding results for the total number of nonlinear iterations (#NN) and the averaged number of linear sweeps (#NL) per nonlinear iteration step together with the elapsed CPU time.

models		Stokes		$Re = 20$		$Re = 50$	
Level		#NN/#NL	CPU	#NN/#NL	CPU	#NN/#NL	CPU
				$\tilde{Q}_1/Q_0$ - SD			
3	fixpoint	4/2	9	11/3	19	17/4	41
	Newton	4/3	9	8/3	18	9/3	19
4	fixpoint	4/3	26	10/3	59	16/3	110
	Newton	4/3	27	6/3	41	7/3	53
5	fixpoint	4/3	113	9/3	206	14/3	346
	Newton	4/3	109	5/2	114	6/3	137
6	fixpoint	4/4	551	8/3	671	12/2	989
	Newton	4/4	522	5/3	562	6/3	601
				$\tilde{Q}_1/Q_0$ - UPW			
3	fixpoint	4/3	9	10/4	35	16/4	53
	Newton	4/3	9	8/4	26	11/5	46
4	fixpoint	4/3	25	10/3	78	15/3	143
	Newton	4/3	25	6/3	47	7/3	71
5	fixpoint	4/3	106	10/3	246	14/3	386
	Newton	4/3	107	5/3	116	6/3	174
6	fixpoint	4/4	505	8/2	633	12/3	1194
	Newton	4/4	516	5/3	525	6/3	535
				Q_2/P_1 - central			
2	fixpoint	4/24	8	12/35	26	18/38	40
	Newton	4/24	7	6/32	11	7/44	14
3	fixpoint	4/52	49	12/67	172	17/78	271
	Newton	4/51	42	6/69	76	7/81	102
4	fixpoint	4/134	400	11/116	1029	16/149	1878
	Newton	4/135	393	6/122	534	7/163	885
5	fixpoint	5/586	9726	11/348	12457	16/315	16193
	Newton	4/541	7184	6/302	6326	6/330	6250

The results from these tables are quite prototypical for similar configurations with low up to medium Re numbers and can be concluded as follows:

1. Both discretizations lead to the same results if we apply sufficiently many grid refinement steps; as expected, the quadratic Q_2/P_1 approach is much more accurate which can be summarized by the following thumb rules:

   'The linear $\tilde{Q}_1/Q_0$ approach requires about 1 or 2 further levels of grid refinement to produce a comparable accuracy as the quadratic Q_2/P_1 ansatz. That means, the required number of elements is about 5 - 20 times larger which results in approximately up to 10 times more unknowns (see Table 4.1). However, keep in mind that the corresponding differences regarding the amount of RAM storage are much smaller since the matrix stencil for the higher-order FEM is significantly bigger!'

2. We clearly see the typical effect of 'optimal' multigrid: the linear convergence rates are in the range of $\rho_{MG} \approx 0.1$ (only 2 - 4 steps to gain two digits are required) and quite independent of the mesh size and also the underlying Re numbers. It is remarkable that the solution of the nonsymmetric Oseen equations is often 'easier' than solving symmetric Stokes problems!
   In contrast, the GMRES solver shows the expected mesh-dependent convergence behavior which is quantitatively much worse than the corresponding multigrid approach. Refining the mesh does not only lead to bigger problem sizes, but also to significantly more linear iteration sweeps due to the increasing condition number of the discrete matrices.
3. The advantage of the more complex Newton solvers in comparison to the 'simple' fixpoint approach is not so obvious: Even in the $Re = 50$ case, the required number of nonlinear fixpoint steps is only 2 - 3 times larger than compared with the Newton variants. However, in contrast to the linear solvers, the nonlinear convergence behavior is only related to the properties of the underlying continuous (!) problem, that means the Re number in our case, which is in contrast to the linear problems which are mainly depending on the condition numbers of the matrices and hence on the mesh width, respectively the mesh topology.

Table 4.4. Direct comparison of the Q_2/P_1 approach versus the $\tilde{Q}_1/Q_0$ Stokes element (with upwinding) for $Re = 20$ (standard stationary CFD benchmark configuration in [100]).

Level	Drag	Lift	#NN/#NL	CPU
		Q_2/P_1 - central		
2	0.9512×10^{-2}	5.5569×10^{0}	6/32	11
3	1.0609×10^{-2}	5.5728×10^{0}	6/69	76
4	1.0616×10^{-2}	5.5777×10^{0}	6/122	534
5	1.0617×10^{-2}	5.5791×10^{0}	6/302	6326
		$\tilde{Q}_1/Q_0$ - UPW		
3	4.7543×10^{-3}	5.5833×10^{0}	8/4	26
4	9.5360×10^{-3}	5.5737×10^{0}	6/3	47
5	1.0455×10^{-3}	5.5769×10^{0}	5/3	116
6	1.0593×10^{-2}	5.5788×10^{0}	5/3	525

As a first summary, we can state that - as expected - the quadratic Q_2/P_1 is more accurate for the considered low up to medium Re numbers which lead to steady state solutions. That means, the 'simpler' $\tilde{Q}_1/Q_0$ approach requires approximately 5 - 20 times more grid points, respectively cells. On the other hand, the corresponding direct multigrid solver for the $\tilde{Q}_1/Q_0$ element pair shows the typical 'optimal' convergence behavior which is in contrast to the preconditioned GMRES solver: The single-grid approach shows convergence rates which clearly depend on the mesh width and which are quantitatively much worse.

Moreover, we have to keep in mind that the use of the stabilization in the case of $\tilde{Q}_1/Q_0$ leads to the reduction of the order of error to $h^{\frac{3}{2}}$ for FEM streamline-diffusion stabilization and h for FEM upwinding stabilization [81] in contrast to the the order of h^3 for the central Q_2/P_1 which make the reliability of this comparison under question for Newtonian law with low and medium Re number !.

Therefore, concerning the total efficiency, the '$\tilde{Q}_1/Q_0$ + multigrid' combination is (still) preferable. It is obvious that such a higher order discretization has a high potential for the future, but the comparisons demonstrate that discretization and solver aspects have to be treated as a unity. Hence, the analogous development of robust and efficient multigrid techniques for the Q_2/P_1 and similar high-order Stokes elements is a must for future research.

4.3.2 Non-Newtonian test case

Since the examined nonlinearity related to the convective term in the case of a steady state solution is quite moderate, our next tests are concerned with the discussed nonlinear viscosity functions. As a first consequence, the equivalence between the gradient and the deformation tensor formulations for the diffusive part are not valid any more, so the stabilized version of the rotated bilinear element pair $\tilde{Q}_1/Q_0$ is required.

The following tables show the results for the *Power Law* model, that means $\nu(\boldsymbol{u}) = (\epsilon + D_{II}(\boldsymbol{u}))^{\frac{r}{2}-1}$, $\epsilon = 10^{-2}$, which has been integrated into both described Navier-Stokes solvers; the geometrical configuration corresponds to the previous 'Flow around cylinder' configuration. Again, we calculate the lift and drag coefficients, and additionally the pressure difference $\triangle\ p$ on the cylinder (see [100]). Due to the fact that the considered flow is very slow, the computation was done without the convective term such that - for numerical test reasons - the nonlinear viscosity is the only source of nonlinearity. However, the calculations show that the strength of the nonlinear behavior for the chosen parameters $r = 1.5$ and particularly $r = 1.1$ is quite significant.

The results for these non-Newtonian test cases are quite similar as those for the Newtonian flow model: Again, the quadratic Q_2/P_1 approach is more accurate while the corresponding GMRES solver for the linear subproblems in each Newton step shows the well known grid dependent convergence behavior. In contrast, the performed multigrid solver in the $\tilde{Q}_1/Q_0$ context is robust against variations in the mesh width and also with respect to the problem-specific parameter r which mainly determines the corresponding nonlinear behavior.

Table 4.5. Comparison of approximation results (drag, lift pressure difference) and of the total number of nonlinear iterations (#NN) and the averaged number of linear sweeps (#NL) per Newton step.

		$\nu(\boldsymbol{u}) = (\epsilon + D_{II}(u))^{\frac{r}{2}-1}$			
Level	Stokes element	Drag	Lift	$\triangle\ p$	#NN/#NL
		$r = 1.5$			
2	$\tilde{Q}_1/Q_0$	1409.60	11.86	22.41	6/2
	Q_2/P_1	1607.10	14.48	25.38	6/27
3	$\tilde{Q}_1/Q_0$	1554.10	13.70	23.99	8/2
	Q_2/P_1	1629.10	14.27	25.16	8/65
4	$\tilde{Q}_1/Q_0$	1594.20	14.25	24.56	9/2
	Q_2/P_1	1635.80	14.39	25.09	8/140
5	$\tilde{Q}_1/Q_0$	1615.60	14.43	24.81	8/2
	Q_2/P_1	1637.60	14.44	25.07	9/723
6	$\tilde{Q}_1/Q_0$	1626.20	14.46	24.94	8/2
		$r = 1.1$			
2	$\tilde{Q}_1/Q_0$	819.49	2.5201	14.22	13/2
	Q_2/P_1	920.59	2.1805	16.76	17/37
3	$\tilde{Q}_1/Q_0$	917.89	3.1958	15.54	14/2
	Q_2/P_1	941.51	3.3310	16.02	14/93
4	$\tilde{Q}_1/Q_0$	916.02	3.7381	15.74	12/2
	Q_2/P_1	953.94	3.9217	15.82	19/294
5	$\tilde{Q}_1/Q_0$	935.13	3.9954	15.82	15/3
	Q_2/P_1	957.64	4.0587	15.87	18/1162
6	$\tilde{Q}_1/Q_0$	946.22	4.0592	15.85	13/5

4.3.3 Examination of the Newton variants

In the final simulations, we will examine the characteristics of the chosen nonlinear solvers of Newton type. To be precise, we demonstrate in the case of the continuous Newton approach the importance of including all terms of the Jacobi matrix in contrast to the simpler fixpoint approach which utilizes the partial differential operator only, hereby evaluated for the results of the last nonlinear iteration step (see in (3.22)).

Table 4.6. Direct comparison of continuous Newton versus fixpoint method for the treatment of the nonlinearity with the $\tilde{Q}_1/Q_0$ Stokes element.

	Newton ($r = 1.5$)		fixpoint ($r = 1.5$)		Newton ($r = 1.1$)		fixpoint ($r = 1.1$)	
Level	#NN/#NL	CPU	#NN/#NL	CPU	#NN/#NL	CPU	#NN/#NL	CPU
2	6/2	11	19/2	37	13/2	60	74/2	228
3	8/2	46	18/2	126	14/2	215	114/2	1359
4	9/2	199	16/2	389	12/2	740	125/2	5871
5	8/2	707	14/2	1517	15/3	3957	119/2	21735
6	8/2	2885	12/2	5047	13/5	25926	−/−	−−

The results in Table 4.6 show the corresponding comparison for the nonconforming $\tilde{Q}_1/Q_0$ element. In both cases, for the full Newton and the simplified fixpoint approach, the described multigrid solvers for the linear auxiliary problems have been applied to gain 2 digits of relative accuracy. While for the moderate case of $r = 1.5$, the differences are not so significant, the harder test case $r = 1.1$ shows the importance of a full Newton solver: Differences of order 6 - 7 with respect to the number of nonlinear iterations occur while the averaged number of linear sweeps remains constant such that differences in the total efficiency of size 6 and more are typical for such flow problems.

Finally, we discuss the sensitivity of the discrete Newton approach via divided differences regarding the involved step-length parameter ε, the mesh width h and the problem-dependent parameter r which is responsible for the strength of the nonlinearity. As explained in (3.9), the discrete Jacobi matrix is calculated via:

$$\left[\frac{\partial \mathcal{R}(\boldsymbol{x}^n)}{\partial \boldsymbol{x}}\right]_{ij} \approx \frac{\mathcal{R}_i(\boldsymbol{x}^n + \varepsilon \boldsymbol{e}_j) - \mathcal{R}_i(\boldsymbol{x}^n - \varepsilon \boldsymbol{e}_j)}{2\varepsilon}. \tag{4.1}$$

Therefore, in the following tables (Table 4.7 and Table 4.8) we examine more carefully the resulting discrete Jacobi matrices with respect to the discussed parameter ε, h and r, and we show how the 'outer' nonlinear convergence behavior as well as the 'inner' linear solution behavior involving the resulting matrices is influenced.

The results clearly indicate that the right choice of the step-length parameter ε might be a delicate task: Choosing ε too big, then the advantageous quasi-quadratic convergence behavior may not appear, while very small parameter values for ε may lead to divergence, due to numerical instabilities. Additionally, the range of 'good' parameter values ε may also depend on the mesh width h and much more significantly on the nonlinearity of the problem itself, which is determined in our case via the parameter r; being outside of this range of admissible values, the increase in necessary CPU time can be extremely big.

Additionally, we examined the influence of the prescribed tolerance parameter TOL which determines the relative accuracy for solving the linear subproblems. Here, the consequences are not so dramatic: Choosing 'big' values for TOL might destroy the quadratic nonlinear convergence properties, while very small parameters will not further improve the global convergence behavior. However, the 'non-optimal' choice can significantly increase the total CPU time such that the recommendation is to gain between 2 - 4 digits of relative defect improvement in each nonlinear iteration as stopping criterion for the linear problems.

Table 4.7. Direct comparison of the results for the discrete Newton approach with the Q_2/P_1 Stokes element for $r = 1.5$; the parameters ϵ and TOL as step-length parameter, respectively as stopping criterion are varied. The results are shown for grid refinement level 2 (top) up to level 5 (bottom). We always provide the total number of nonlinear iterations (#NN), the averaged number of linear sweeps (#NL) per Newton step and the elapsed CPU time in seconds. The maximum number of nonlinear Newton steps is **40**.

$\varepsilon \setminus$ TOL	10^{-1}	10^{-2}	10^{-3}	10^{-4}
		Level 2		
10^{-2}	**40**/ 4 [60]	32/ 7 [49]	30/ 13 [48]	21/ 20 [36]
10^{-3}	14/ 12 [22]	10/ 16 [16]	8/ 24 [14]	8/ 29 [15]
10^{-4}	10/ 15 [16]	8/ 19 [13]	6/ 27 [11]	7/ 29 [13]
10^{-5}	10/ 15 [16]	8/ 19 [13]	6/ 27 [11]	7/ 29 [13]
10^{-6}	10/ 15 [16]	8/ 19 [13]	6/ 27 [11]	7/ 29 [13]
10^{-7}	10/ 15 [16]	8/ 19 [13]	6/ 27 [11]	7/ 29 [13]
10^{-8}	10/ 15 [16]	8/ 19 [13]	6/ 27 [11]	7/ 29 [13]
		Level 3		
10^{-2}	**40**/ 7 [280]	**40**/ 14 [305]	**40**/ 22 [335]	37/ 36 [358]
10^{-3}	33/ 24 [288]	14/ 35 [134]	10/ 57 [120]	11/ 67 [145]
10^{-4}	11/ 40 [113]	10/ 40 [103]	8/ 65 [105]	8/ 70 [114]
10^{-5}	11/ 38 [113]	9/ 43 [99]	8/ 65 [109]	8/ 70 [110]
10^{-6}	11/ 38 [114]	9/ 43 [97]	8/ 65 [105]	8/ 70 [111]
10^{-7}	21/ 25 [189]	21/ 35 [212]	13/ 58 [167]	14/ 78 [207]
10^{-8}	21/ 23 [185]	15/ 40 [160]	11/ 62 [146]	15/ 82 [234]
		Level 4		
10^{-2}	**40**/ 11 [1306]	**40**/ 23 [1548]	**40**/ 51 [2055]	**40**/ 84 [2720]
10^{-3}	**40**/ 33 [1745]	31/ 48 [1561]	16/ 102 [1314]	18/ 129 [1877]
10^{-4}	15/ 85 [1124]	11/ 104 [983]	9/ 134 [999]	9/ 199 [1399]
10^{-5}	11/ 101 [976]	9/ 100 [807]	8/ 140 [941]	9/ 204 [1423]
10^{-6}	11/ 100 [954]	9/ 100 [798]	8/ 139 [920]	9/ 204 [1426]
10^{-7}	10/ 104 [898]	15/ 97 [1320]	10/ 138 [1148]	13/ 219 [2241]
10^{-8}	**40**/ 29 [1814]	**40**/ 156 [5174]	**40**/ 199 [6244]	**40**/ 274 [8108]
		Level 5		
10^{-2}	diverge	**40**/ 57 [10153]	**40**/ 122 [17075]	**40**/ 45 [31638]
10^{-3}	**40**/ 35 [8251]	**40**/ 82[13550]	26/ 214 [18679]	22/ 348 [25640]
10^{-4}	20/ 181 [13244]	16/ 264 [14637]	14/ 432 [20002]	9/ 755 [22325]
10^{-5}	11/ 296 [11331]	8/ 492 [12978]	9/ 723 [22105]	8/ 944 [25220]
10^{-6}	25/ 148 [13947]	10/ 374 [12388]	14/ 383 [18271]	11/ 590 [22030]
10^{-7}	**40**/ 255 [37031]	27/ 479 [44067]	20/ 757[50167]	19/ 811 [50788]
10^{-8}	**40**/ 252 [36063]	**40**/ 245[28289]	**40**/356 [47587]	**40**/ 472[62539]

Table 4.8. Direct comparison of the results for the discrete Newton approach with the Q_2/P_1 Stokes element for $r = 1.1$; the parameters ϵ and TOL as step-length parameter, respectively as stopping criterion are varied. The results are shown for grid refinement level 2 (top) up to level 5 (bottom). We always provide the total number of nonlinear iterations (#NN), the averaged number of linear sweeps (#NL) per Newton step and the elapsed CPU time in seconds. The maximum number of nonlinear Newton steps is **40**. ($*$ - maximal CPU time exceeded)

$\varepsilon \setminus$ TOL	10^{-1}	10^{-2}	10^{-3}	10^{-4}
		Level 2		
10^{-2}	**40**/ 6 [62.0]	**40**/ 15 [67.1]	**40**/ 27 [74.4]	**40**/ 34 [79.8]
10^{-3}	26/ 15 [43]	19/ 23 [34]	20/ 35 [39]	19/ 43 [40]
10^{-4}	16/ 20 [28]	15/ 28 [28]	18/ 37 [37]	19/ 43 [40]
10^{-5}	15/ 20 [26]	14/ 27 [26]	17/ 37 [35]	19/ 43 [40]
10^{-6}	16/ 21 [28]	14/ 27 [26]	17/ 37 [34]	19/ 43 [40]
10^{-7}	16/ 21 [28]	14/ 27 [26]	17/ 37 [35]	19/ 43 [40]
10^{-8}	16/ 22 [28]	14/ 27 [26]	17/ 37 [35]	19/ 43 [41]
		Level 3		
10^{-2}	diverge	**40**/ 24 [353]	**40**/ 43 [435]	**40**/ 69 [547]
10^{-3}	**40**/ 10 [297]	26/ 44 [286]	21/ 75 [305]	18/ 99 [326]
10^{-4}	**40**/ 21 [352]	17/ 70 [243]	16/ 92 [275]	15/ 114 [304]
10^{-5}	35/ 33 [354]	15/ 70 [219]	14/ 93 [243]	14/ 115 [286]
10^{-6}	33/ 37 [348]	15/ 70 [220]	14/ 93 [244]	14/ 115 [296]
10^{-7}	**40**/ 34 [411]	29/ 79 [461]	29/ 88 [495]	18/ 104 [342]
10^{-8}	**40**/ 32 [403]	**40**/ 50 [483]	31/ 89 [525]	32/ 115 [656]
		Level 4		
10^{-2}	diverge	diverge	**40**/ 86 [3047]	**40**/ 158 [5078]
10^{-3}	diverge	**40**/ 70 [2726]	**40**/ 119 [4015]	37/ 214 [6100]
10^{-4}	31/ 63 [2113]	**40**/ 78 [3050]	20/ 263 [4055]	20/ 431 [6486]
10^{-5}	**40**/ 82 [3060]	16/ 208 [2721]	19/ 294 [4380]	18/ 454 [6198]
10^{-6}	**40**/ 82 [3087]	16/ 214 [2733]	19/ 296 [4435]	18/ 454 [6314]
10^{-7}	21/ 86 [1831]	18/ 205 [3058]	19/ 296 [4532]	18/ 455 [6472]
10^{-8}	diverge	diverge	diverge	diverge
		Level 5		
10^{-2}	**40**/ 13 [5997]	**40**/ 68 [12117]	**40**/ 239 [35923]	**40**/678 [119583]
10^{-3}	**40**/ 32 [8081]	**40**/179 [28095]	**40**/ 334 [44798]	**40**/ 661[86097]
10^{-4}	**40**/ 71 [13974]	33/ 368 [45204]	24/ 795 [70727]	18/1429 [82560]
10^{-5}	**40**/ 90 [14493]	37/ 476 [59433]	18/1162 [77307]	17/1818 [112571]
10^{-6}	**40**/902 [133602]	31/1250 [127105]	37/1387 [132800]	35/1798 [169726]
10^{-7}	**40**/820 [120798]	**40**/1128 [119128]	39/862 [102043]	31/1450 [127530]
10^{-8}	$*$	$*$	$*$	$*$

Table 4.9. Summarized presentation of the results for the discrete Newton approach with the Q_2/P_1 Stokes element for $r = 1.5$ and $r = 1.1$ on the different mesh levels. The calculations are performed for our 'preferred' configuration $\varepsilon = 10^{-5}$ and $TOL = 10^{-3}$ which seems to give the most robust convergence behavior.

	$r = 1.5$		$r = 1.1$	
Level	#NN/#NL	CPU	#NN/#NL	CPU
2	6/27	11	17/37	35
3	8/65	109	14/93	243
4	8/140	941	19/294	4 380
5	9/723	22 105	18/1 162	77 307

4.4 Conclusions

In this comparative study, we have analyzed the influence of two different FEM discretization techniques (conforming Q_2/P_1, nonconforming $\tilde{Q}_1/Q_0$ elements) and solution procedures (various nonlinear Newton variants and multigrid versus Krylov-space solvers for the linear subproblems) onto the approximation properties and particularly the total efficiency of corresponding simulation tools for incompressible fluids. We have discussed algorithmic details and provided numerical results for laminar steady-state incompressible flow examples including Newtonian and non-Newtonian behavior of *Power Law* type.

The following two approaches have been compared which both are quite popular in the CFD community; additionally, both of them are representative for typical methodologies which are in use for such types of flow simulations:

1. The Q_2/P_1 Stokes element with central differencing for the convective, term with a discrete nonlinear Newton solver based on 'Divided Differences' together with a preconditioned single-grid GMRES method for the auxiliary linear problems of Oseen type:

This pair of FEM functions leads due to the involved biquadratic polynomials to a higher order of accuracy than compared with linear approaches, at least for the considered low up to medium Re numbers; in contrast, for higher Re numbers, the question of stabilizing the discretized convective terms in the FEM context while maintaining the higher order accuracy has not been discussed and is one of the current research topics in the mathematical CFD community.

While the discrete Newton method leads in most cases - up to the optimal parameter choice for the 'Divided Differences' approach - to quite satisfying results concerning the numerical stability and efficiency, the involved GMRES solver as prototype for a non-multigrid Krylov-space method shows the expected dependence of mesh size which leads to huge numbers of linear iteration steps if the mesh size has to be decreased by accuracy reasons.

2. The nonconforming rotated bilinear $\tilde{Q}_1/Q_0$ Stokes element with upwinding, respectively streamline-diffusion stabilization for the convective term and with a continuous nonlinear Newton solver together with an adapted multigrid method for the resulting Oseen-type subproblems:

The resulting accuracy of this 'linear' approach is lower such that up to 5 - 10 times more grid points are needed to produce results of similar quality as with the Q_2/P_1 approach. However, highly sophisticated FEM discretization techniques for the convective terms are available which can be directly applied for

convection-dominated flows while maintaining a similar accuracy and robustness as for the considered steady-state flow configurations.

The advantages of this approach are - beside the continuous Newton solver for the nonlinearity which however can be performed for the Q_2/P_1 scheme, too - the realized multigrid solver for the linearized problems. After a careful optimization of all multigrid components in relation to the underlying FEM spaces, the typical robust and very efficient convergence behavior of the multigrid approaches can be obtained such that the linear problems can be solved with a numerical efficiency which is more or less independent of the problem size, the mesh topology and also the type of problems, as for instance Stokes or Oseen problem for different Re numbers, coming from Newtonian and non-Newtonian models.

Concerning the question of the 'total efficiency', that means the amount of CPU seconds to provide a certain accuracy for a given flow problem, the answer due to our massive test calculations should be as follows: the higher order Q_2/P_1 approach requires about 5 - 20 times less grid points, however due to the missing multigrid solvers, the corresponding CPU time is huge. Altogether, the simpler nonconforming $\tilde{Q}_1/Q_0$ Stokes element together with the already realized multigrid components seems to be the better compromise at the moment, if we analyze the available flexibility and efficiency of this combination: 'Multigrid is a must for incompressible flow problems!'

As an outlook, it is clear that the examined Q_2/P_1 approach shows a huge potential for future improvement for complex fluid simulations, but the potentially high order approximation properties have to be combined with adequate multigrid solvers. This must be one of the main tasks for Mathematics and Numerics in the CFD community and should be one of the major future research topics. Realizing the vision of a 'robust and flexible higher order FEM discretization' with 'accurate FEM treatment of the convective terms' together with 'adaptive local grid refinement' on the basis of 'rigorous a posteriori error control for user-specified functionals' in combination with efficient nonlinear Newton-like and linear multigrid-like solvers', that should be the aim for future work!

5

Unified edge-oriented stabilization

This chapter deals with different aspects of edge-oriented stabilization techniques for nonconforming finite element methods for the numerical solution of incompressible flow problems. We discuss two separate classes of problems which require appropriate stabilization techniques: First, the lack of coercivity for nonconforming low order approximations for treating problems with the symmetric deformation tensor instead of the gradient formulation in the momentum equation ('Korn's inequality') which particularly leads to convergence problems of the iterative solvers for small Reynolds (Re) numbers. Second, numerical instabilities for high Re numbers or whenever convective operators are dominant such that the standard Galerkin formulation fails and leads to spurious oscillations . We show that the right choice of edge-oriented stabilization is able to provide simultaneously excellent results regarding robustness and accuracy for both seemingly different cases of problems, and we discuss the sensitivity of the involved parameters with respect to mesh distortions and variations of the Re number. Moreover, we explain how efficient multigrid solvers can be constructed to circumvent the problems with the arising 'non-standard' FEM data structures, and we provide several examples for the numerical efficiency for realistic flow configurations with benchmarking character.

5.1 Introduction

Stabilization techniques for (nonconforming) FEM discretizations in the context of incompressible flow problems, for instance described by the Navier-Stokes equations or appropriate extensions in multiphase problem settings, are still a challenging task. In this chapter, particularly from a practical point of view, we want to analyze special edge-oriented stabilization techniques regarding the following three aspects:

I. Necessity. There are two well-known situations for nonconforming finite element methods when severe numerical problems may arise: the lack of coercivity for nonconforming low order approximations for symmetric deformation tensor formulations, mainly visible for small Re numbers, and whenever convective operators are dominant, for instance for medium and high Re numbers or for the treatment of pure transport problems. Then, the standard Galerkin formulation fails and may lead to numerical oscillations or convergence problems of the iterative solvers, too.

II. Robustness. To analyze the ability of edge-oriented stabilization terms for a wide range of Re numbers and for different problems is one of the central aims for the use of edge-oriented stabilization techniques as black box tools in future CFD codes. Here, the question of appropriate parameter settings and stabilization coefficients is always a delicate task, particularly on general meshes.

III. Efficiency. One disadvantage of edge-oriented stabilization is the contribution of an additional layer of neighboring elements via jumps across the edges. So, a new sparsity pattern for the resulting stiffness matrix is introduced which may contradict to the usual data structures of finite element methods. In the context of preconditoned Krylov-space or multigrid solvers, we show how suitable preconditioners, for instance in the framework of defect-correction schemes, can be applied.

Our contribution has the goal to critically discuss these 3 aspects via a numerical analysis which we restrict to the incompressible Navier-Stokes equations since they contain already most of the typical difficulties. Extensions to more complex problems, for instance multiphase flow or nonlinear viscosities (granular, non-Newtonian, visco-elastic flow) are possible and are described, for instance, in [71].

5.2 Short review on edge-oriented stabilization methods

The main idea is to augment the original finite element discretization by an interior penalty term involving the jump of the function values or of (part of) the gradient of the approximate FEM solution. In the literature, several jump terms were introduced for different situations:

I. Jump terms including function values

$$j_1(\boldsymbol{u},\boldsymbol{v}) = \sum_{\text{edge E}} \gamma\nu \frac{1}{|E|} \int_E [\boldsymbol{u}][\boldsymbol{v}] d\sigma \tag{5.1}$$

John et al. [51] introduced the jump term in the nonconforming streamline-diffusion method for convection dominated problem to achieve the same accuracy as with conforming streamline-diffusion FEM methods. Moreover, to satisfy the discrete Korn's inequality, variants have been presented by Hansbo and Larson in [39] and by Turek, Ouazzi and Schmachtel in [98]. And, in a similar way, an analogous approach for a general Korn's inequality for piecewise H^1-functions has been introduced by Brenner in [9].

II. Jump terms including the gradient

$$\begin{aligned}
j_{2,\alpha}(\boldsymbol{u},\boldsymbol{v}) &= \sum_{\text{edge E}} \gamma|E|^\alpha \int_E [\nabla\boldsymbol{u}][\nabla\boldsymbol{v}] d\sigma \\
j_{3,\alpha}(\boldsymbol{u},\boldsymbol{v}) &= \sum_{\text{edge E}} \gamma|E|^\alpha \int_E [\boldsymbol{n}\cdot\nabla\boldsymbol{u}][\boldsymbol{n}\cdot\nabla\boldsymbol{v}] d\sigma \\
j_{4,\alpha}(\boldsymbol{u},\boldsymbol{v}) &= \sum_{\text{edge E}} \gamma|E|^\alpha \int_E [\boldsymbol{t}\cdot\nabla\boldsymbol{u}][\boldsymbol{t}\cdot\nabla\boldsymbol{v}] d\sigma \\
j_{5,\alpha}(\boldsymbol{u},\boldsymbol{v}) &= \sum_{\text{edge E}} \gamma|E|^\alpha \int_E [(\boldsymbol{t}\cdot\nabla\boldsymbol{u})\cdot\boldsymbol{n}][(\boldsymbol{t}\cdot\nabla\boldsymbol{v})\cdot\boldsymbol{n}] d\sigma
\end{aligned} \tag{5.2}$$

These terms (with different values for α) for stabilizing convection dominated problems have been introduced by Douglas and Dupont in [25], Burman, Hansbo et al. in [16, 18], see also [14] and [17].

III. Jump terms including the divergence

$$j(\boldsymbol{u},\boldsymbol{v}) = \sum_{\text{edge E}} \gamma |E|^2 \int_E [\nabla \cdot \boldsymbol{u}][\nabla \cdot \boldsymbol{v}] d\sigma \tag{5.3}$$

This approach was originally proposed by Burman, Hansbo et al. in [18] to control the incompressibility condition.

IV. Jump terms including the normal component of function values

$$j(\boldsymbol{u},\boldsymbol{v}) = \sum_{\text{edge E}} \gamma \nu \frac{1}{|E|} \int_E [\boldsymbol{n} \cdot \boldsymbol{u}][\boldsymbol{n} \cdot \boldsymbol{v}] d\sigma \tag{5.4}$$

To control the nonconformity arising from the pressure term in Darcy's law, this term has been introduced by Burman and Hansbo in [15].

The techniques proposed in III. and IV. will not be discussed in the following since they are not essential for the stabilization of Korn's inequality, respectively of convection dominated flow which is the main aim of our studies in this chapter. So, summarizing this overview, it shows that for different types of problems corresponding jump terms with "free" constant γ and order $|E|^\alpha$ have been introduced. Our aim is to analyze a new variant which uses only one jump term and only (almost) one choice for the free parameter γ, and which is nevertheless able to simultaneously treat both types of problems. To be precise, we propose the following jump term, respectively discrete stabilization term (with $h_E = |E|$)

$$\langle \mathbf{J}\boldsymbol{u}, \boldsymbol{v} \rangle = \sum_{\text{edge E}} \max(\gamma^* \nu h_E, \gamma h_E^2) \int_E [\nabla \boldsymbol{u}][\nabla \boldsymbol{v}] d\sigma \tag{5.5}$$

which will be added to the original bilinear form, respectively discretized stiffness matrices, and which uses only the gradient of the approximate solution. This approach is based on a blending of (5.1), applying an appropriate scaling with $|E|^2$ due to the gradient of the discrete solution, together with the formula in (5.2), applying $\alpha = 2$. In the case of nonlinear viscosity ν, this stabilization term may depend in a nonlinear way on the solution, too. The parameters γ, γ^* can be chosen - more or less arbitrarily as the subsequent tests will show - in the interval $[0.0001, 0.1]$, with no significant influence on the resulting accuracy, robustness and efficiency.

Summarizing, we can distinguish between the following situations:

1. In the case of treating the convection, $\boldsymbol{u} \cdot \nabla \boldsymbol{u}$, the upwinding and the streamline-diffusion approach modify the original discrete convective operator $\langle \mathbf{N}(\boldsymbol{u})\boldsymbol{v}, \boldsymbol{w} \rangle$ by an operator $\langle \tilde{\mathbf{N}}(\boldsymbol{u})\boldsymbol{v}, \boldsymbol{w} \rangle$ which may depend in a nonlinear way on the solution $\boldsymbol{u}$ itself via the local Re number; in contrast, the edge-oriented technique always adds a linear operator $\langle \mathbf{J}\boldsymbol{u}, \boldsymbol{v} \rangle$, unless an additional shock-capturing term is used.
2. In the case of treating the deformation tensor formulation, $\mathbf{D}(\boldsymbol{u})$, the edge-oriented stabilization employs an additional stabilization term which mainly depends on the size of the viscosity ν; if ν depends on the solutions $\boldsymbol{u}$ and p, then this stabilization can become nonlinear. In the case of upwinding and streamline-diffusion, a corresponding stabilization is only performed if the convective operator is getting dominant. That means that for very low Re numbers, but with deformation tensor, no stabilization is applied since the local Re number vanishes. Moreover, if the viscosity ν is nonlinear, then the stabilization is (even more) nonlinear due to the local Re number which then depends on the unknown solution $\boldsymbol{u}$, respectively p.

Looking more carefully at the resulting matrix stencils for the terms $\int_E [\nabla\phi_i][\nabla\phi_j] d\sigma$, the matrix structure can be seen in Fig. 5.1. While the matrix stencils are always increased, leading to couplings between FEM basis functions which do not have common local support, it is also visible that reduced integration may lead to a different amount of additional memory requirements.

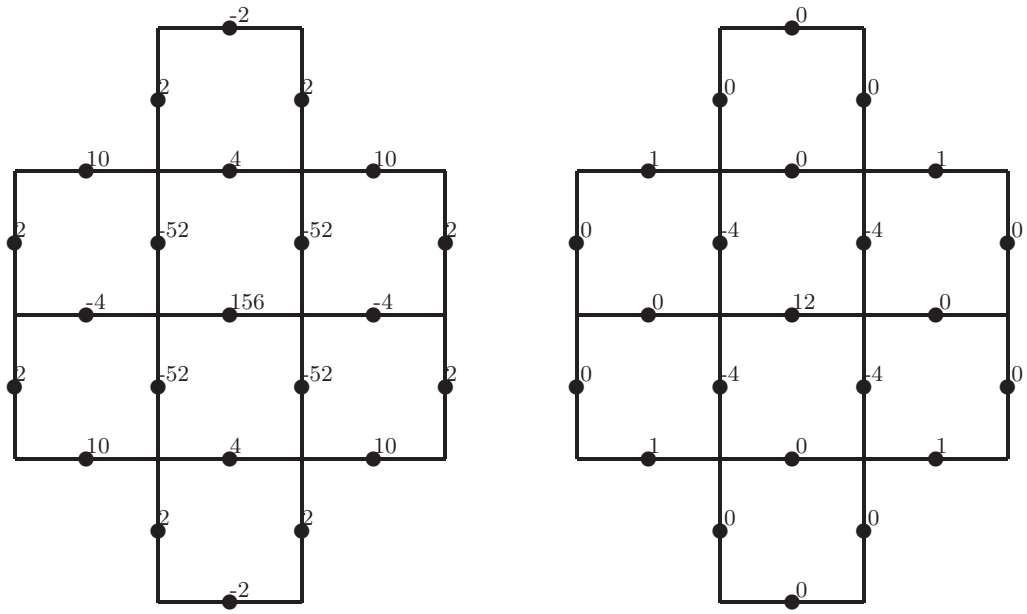

Fig. 5.1. Stencil for $\int_E [\nabla\phi_i][\nabla\phi_j] d\sigma$ with exact (left) and with 1x1 Gauss quadrature (right)

5.3 Error estimates

In this section we present results of a priori error estimates for the Newtonian case. Then the non-Newtonian case can be treated in the same manner following Baranger and Najib [4].

Lemma 1. *For the interior penalty term (5.5) there holds for all* $\boldsymbol{v} \in V_h$

$$\sum_{edges E} \nu h_E^{-1} \int_E [\boldsymbol{v}][\boldsymbol{v}]\, ds \leq c\, \langle \mathbf{J}\boldsymbol{u}, \boldsymbol{v}\rangle \quad \textit{and} \tag{5.6}$$

$$\langle \mathbf{J}\boldsymbol{v}, \boldsymbol{v}\rangle \leq c_{\gamma^*} \|v\|_h^2 . \tag{5.7}$$

Proof. The proof is an immediate consequence of the equivalence between the jumps in the solution and the jumps in the tangential gradient. Furthermore, the $H(div, \Omega)$ consistency of the formulation is achieved without adding the jump of the normal velocity for the same reason. The second claim is directly deduced for the trace inequality.

Lemma 2. *There exists a constant c, indendent of h and* ν *such that*

$$\|\boldsymbol{v}\|_h^2 \leq c\, \|\boldsymbol{v}\|^2 \qquad \textit{for all} \quad \boldsymbol{v} \in V_h. \tag{5.8}$$

Proof. See Brenner [9], Hansbo and Larson [39] and Lemma 1.

Theorem 3. *There exist constants α, β and c strictly positive and independent of h such that*

$$\alpha \left\| \boldsymbol{v} \right\|^2 \leq \left((\mathbf{A}(\boldsymbol{v}) + \mathbf{J})\boldsymbol{v}, \boldsymbol{v} \right), \tag{5.9}$$

$$\beta \leq \inf_{q \in Q_h} \sup_{v \in V_h} \frac{(q, \nabla \cdot v)}{\left\| \boldsymbol{v} \right\| \left\| q \right\|_{Q_h}}, \tag{5.10}$$

moreover, we have the bound for errors

$$\left\| u - u_h \right\|_h + \left\| p - p_h \right\|_0 \leq c\, h \left\{ \left\| \boldsymbol{u} \right\|_2 + \left\| p \right\|_1 \right\}. \tag{5.11}$$

Proof. Note that

$$\mathbf{N}(\boldsymbol{u}, \boldsymbol{v}, \boldsymbol{w}) = -\mathbf{N}(\boldsymbol{u}, \boldsymbol{w}, \boldsymbol{v}) \qquad \text{for all } \boldsymbol{u}, \boldsymbol{v}, \boldsymbol{w} \in V_h \tag{5.12}$$

and also

$$\mathbf{N}(\boldsymbol{u}, \boldsymbol{v}, \boldsymbol{v}) = 0 \qquad \text{for all } \boldsymbol{u}, \boldsymbol{v} \in V_h \tag{5.13}$$

Then, Theorem 3 is an immediate consequence from Lemma 1 and Lemma 2 in conjunction with the properties of the approximate spaces of Rannacher and Turek [75, 90].

5.4 Numerical examples

5.4.1 Flow around a cylinder

In the subsequent sections, we will analyze the numerical behavior of edge-oriented stabilization techniques, particularly of our proposed choice in (5.5), in comparison to upwinding and streamline-diffusion, hereby regarding the following aspects:

- problems with medium and high Reynolds number,
- problems with discrete Korn's inequality for low Re numbers,
- problems with variable (nonlinear) viscosity.

The incompressible flow problem to be dealt with is the well-known benchmark 'flow around a cylinder' developed in 1995 for the priority research program "Flow simulation on high-performance computers" under the auspices of the DFG, the German Research Association [100]. This project was intended to facilitate the evaluation of various numerical algorithms for the incompressible Navier-Stokes equations in the laminar flow regime. A quantitative comparison of simulation results is possible on the basis of relevant flow characteristics such as drag and lift coefficients, for which sufficiently accurate reference values can be obtained. Moreover, the efficiency of different solution techniques can be analyzed in an objective manner.

Stationary flow around a cylinder: $Re = 1$

One of the reasons why edge-oriented stabilization was becoming so attractive for low order nonconforming finite element methods is its ability to handle flow problems in the range of very small Re numbers, that means more or less Stokes flow, if formulated in terms of the symmetric gradient $\mathbf{D}(\boldsymbol{v})$ of velocity [9, 39, 98]. Therefore, we start our computational tests to demonstrate the efficiency of the proposed edge-oriented stabilization for this situation. However, in this case we mainly concentrate on the solver aspects, that means the robustness of the multigrid solver with respect to Korn's inequality since the accuracy is not the critical case (see [98]) for these flow configurations. Nevertheless, we apply the different stabilization techniques, including upwinding and streamline-diffusion, also for this low Re number problem, hereby formulated in terms of the gradient of velocity, too. In principle, there is no need for any stabilization in this case, but as it becomes clear from Table 5.1, there is also no negative side effect such that edge-oriented stabilization is a black box candidate for low and medium Re numbers, despite the fact that there is no local Re number for an explicit control of the amount of involved convection.

Table 5.1. Drag and lift coefficients and convergence results for $Re = 1$ for gradient formulation

Stab.	$j_{2,1}$ (γ)		SD (δ^*)		UPW (δ^*)		Central
Level	0.001	0.01	0.1	0.5	0.1	1.0	no stab.
			Drag ($C_D = 3142.4$)				
3	3084.7	3084.7	3084.6	3084.6	3084.7	3084.7	3084.6
4	3127.4	3127.4	3127.4	3127.4	3127.4	3127.4	3127.4
5	3138.6	3138.6	3138.6	3138.6	3138.6	3138.6	3138.6
6	3141.5	3141.5	3141.5	3141.5	3141.5	3141.5	3141.5
			Lift ($C_L = 30.865$)				
3	29.556	29.556	29.561	29.561	29.556	29.555	29.561
4	30.525	30.525	30.526	30.526	30.525	30.525	30.526
5	30.780	30.780	30.780	30.780	30.780	30.780	30.780
6	30.844	30.844	30.844	30.844	30.844	30.844	30.844
			NL/AVMG				
3	4/3	4/3	4/3	4/3	4/3	4/3	4/3
4	3/2	3/2	3/2	3/2	3/2	3/2	3/2
5	4/2	4/2	4/2	4/2	4/2	4/2	4/2
6	4/2	4/2	4/2	4/2	4/2	4/2	4/2

Next, we apply the different stabilization techniques for $Re = 1$, but now formulated in terms of the symmetric gradient of the velocity. Table 5.2 shows that applying edge-oriented stabilization techniques, with the jump of function values (5.1) in conjunction with upwinding or streamline-diffusion or central differencing, or purely with our proposed jump of the gradient, leads to optimal results.

Moreover, in order to examine the correct order α in $|E|^\alpha$ (see (5.2)) for low Re numbers, we perform tests with different values for α and γ with the deformation formulation. Table 5.3 shows that the multigrid solver for the variant $j_{2,1}$ (behaving like γh) is independent of the refinement in contrast to variant $j_{2,2}$ (behaving like γh^2) which significantly depends on the refinement level due to under-stabilization.

Table 5.2. Drag and lift coefficients and convergence results for $Re = 1$ with the symmetric gradient

Stab.	$j_{2,1}(\gamma)$		SD ($\delta^* = 0.1$) and $j_1(\gamma)$		UPW ($\delta^* = 0.1$) and $j_1(\gamma)$		central
Level	0.001	0.01	0.0	0.1	0.0	0.1	no stab.
			Drag ($C_D = 3142.4$)				
3	3104.5	3110.5	3103.8	3106.4	3103.9	3106.4	3103.8
4	3132.5	3133.6	3132.4	3133.1	3132.4	3133.1	3132.4
5	3139.9	3139.9	3139.9	3140.1	3139.9	3140.1	3139.9
6	3141.8	3141.6	3141.8	3141.8	3141.8	3141.8	3141.8
			Lift ($C_L = 30.8657$)				
3	30.060	30.132	30.055	30.087	30.052	30.084	30.055
4	30.658	30.668	30.658	30.667	30.657	30.666	30.658
5	30.813	30.810	30.813	30.816	30.813	30.816	30.813
6	30.852	30.849	30.853	30.853	30.853	30.853	30.853
			NL/AVMG				
3	4/3	3/2	4/11	4/2	4/9	4/2	4/11
4	4/3	4/2	4/29	4/2	4/29	4/2	4/29
5	4/3	4/2	5/98	4/2	4/99	4/2	5/98
6	4/3	4/2	5/154	4/2	5/154	4/2	5/154

Table 5.3. Nonlinear iterations (NL)/Averaged multigrid sweeps (AVMG) per nonlinear iteration for $Re = 1$ with deformation tensor formulation and edge-oriented stabilizations $j_{2,1}$ (with order h) and $j_{2,2}$ (with order h^2)

Stab.		$j_{2,2}$			$j_{2,1}$	
γ	0.0001	0.1	1.0	0.001	0.01	0.1
			Drag ($C_D = 3142.4$)			
4	3132.4	3132.7	3134.9	3132.5	3133.6	3147.7
5	3139.9	3139.9	3140.1	3139.9	3139.9	3142.2
6	3141.8	3141.8	3141.8	3141.8	3141.6	3141.5
			Lift ($C_L = 30.8657$)			
4	30.657	30.660	30.687	30.658	30.668	30.908
5	30.813	30.814	30.816	30.813	30.810	30.863
6	30.853	30.853	30.853	30.852	30.849	30.857
			NL/AVMG			
4	4/2	4/4	4/3	4/3	4/2	3/6
5	4/51	4/6	4/2	4/3	4/2	3/6
6	4/81	4/10	4/3	4/3	4/2	4/6

				NL/AVMG				
γ	0.01	0.05	0.1	0.5	0.01	0.05	0.1	0.5
4	4/14	4/6	4/4	4/2	4/2	4/2	4/5	–
5	4/19	4/10	4/7	4/3	4/2	4/2	4/5	–
6	4/24	4/16	4/11	4/6	4/2	4/2	4/6	–

Stationary flow around a cylinder: $Re = 20$

We consider the steady incompressible flow around a cylinder with circular cross-section which at $Re = 20$ is mainly dominated by diffusion and could be simulated even by the standard Galerkin method without any extra stabilization. However, a certain stabilization is necessary for solving the resulting linear systems with iterative solvers while the central differencing scheme, that means the standard Galerkin approach, usually leads to divergence if using the multigrid solvers. The drag and lift coefficients should approach the reference values $C_D = 5.5795$ and $C_L = 0.01061$ during mesh refinement. The examined stabilization techniques for the convective term have employed the described streamline-diffusion, the FEM upwinding and the edge-stabilization via $j_{2,2}$. Here, we list the number of resulting nonlinear iterations (NL) and the averaged number of multigrid sweeps per nonlinear iteration (AVMG) to gain a prescribed tolerance (here: 1 digit).

Table 5.4. Drag and lift coefficients for gradient formulation with various stabilization techniques for $Re = 20$

Stab.	$j_{2,2}$ (γ)			SD (δ^*)		UPW (δ^*)		Central
Level	0.0001	0.001	0.01	0.1	0.5	0.1	1.0	no stab.
				Drag ($C_D = 5.5795$)				
3	5.5874	5.5940	5.6186	5.7144	6.0354	5.6700	6.1152	5.6470
4	5.5855	5.5864	5.5901	5.6417	5.7977	5.6005	5.7460	5.6040
5	5.5813	5.5815	5.5823	5.6020	5.6655	5.5841	5.6197	5.5862
6	5.5800	5.5800	5.5803	5.5868	5.6092	5.5806	5.5882	5.5812
				Lift ($C_L = 0.01061$)				
3	0.007328	0.007907	0.008874	0.006933	0.004884	0.005699	-0.002169	0.006237
4	0.009698	0.009806	0.010022	0.008633	0.007506	0.009697	0.007025	0.008604
5	0.010382	0.010398	0.010436	0.009914	0.009227	0.010483	0.010232	0.010043
6	0.010560	0.010562	0.010566	0.010394	0.010065	0.010598	0.010733	0.010471
				NL/AVMG				
3	12/3	12/3	12/13	11/3	11/3	10/3	10/3	34/2
4	12/3	12/3	12/11	12/3	11/2	11/3	10/3	17/2
5	12/2	12/2	12/9	12/2	12/2	12/2	11/3	12/2
6	12/2	12/2	12/8	12/2	12/2	12/2	12/2	12/2

From Tables 5.4 and 5.5 the following conclusions can be drawn:

- **Streamline-diffusion and upwinding:**
  - The accuracy depends significantly on the user-defined parameter δ^*.
  - The multigrid solver behaves much better, in the case of the deformation tensor formulation, with the additional edge stabilization j_1 since the influence of the kernel function due to the discrete Korn's inequality has been neutralized (see [98]).
- **Edge-oriented stabilization:**
  - The accuracy is much less sensitive with respect to the value of the user-defined parameter γ.
  - For both gradient and deformation tensor formulations, the multigrid solver is only slightly sensitive with respect to over and under-stabilization.
  - There is no need for the additional edge-oriented stabilization j_1.

Table 5.5. Corresponding drag and lift coefficients for deformation tensor formulation for $Re = 20$

Stab.	$j_{2,2}$ (γ)			SD($\delta^* = 0.1$) and $+j_1(\gamma)$		UPW ($\delta^* = 0.1$) and $+j_1(\gamma)$		central
Level	0.0001	0.001	0.01	0.0	0.1	0.0	0.1	no stab.
				Drag ($C_D = 5.5795$)				
3	5.5913	5.5906	5.6060	5.6764	5.6772	5.5914	5.5921	5.5970
4	5.5846	5.5838	5.5811	5.6261	5.6264	5.5847	5.5850	5.5865
5	5.5810	5.5807	5.5790	5.5974	5.5975	5.5810	5.5811	5.5814
6	5.5799	5.5798	5.5793	5.5856	5.5856	5.5799	5.5799	5.5800
				Lift ($C_L = 0.01061$)				
3	0.007993	0.008350	0.009084	0.008197	0.008219	0.007932	0.007964	0.008013
4	0.009893	0.009956	0.010120	0.009402	0.009412	0.009883	0.009894	0.009581
5	0.010432	0.010441	0.010464	0.010170	0.010173	0.010431	0.010434	0.010330
6	0.010572	0.010573	0.010574	0.010465	0.010465	0.010572	0.010573	0.010545
				NL/AVMG				
3	12/3	12/3	12/14	12/3	12/3	12/5	12/3	52/2
4	12/3	12/2	12/12	12/2	12/2	12/5	12/2	19/2
5	12/3	12/2	12/8	12/5	12/2	12/11	12/2	21/2
6	12/4	12/2	12/8	12/9	12/2	12/12	12/2	26/2

The 'classical' stabilization techniques may be analyzed in the framework of artificial diffusion methods, and it is immediately clear that the gain of more stabilization is coupled with loss of accuracy if too much diffusion is added (see for instance [12]). Therefore, a very important factor is the local Re number which measures the ratio between diffusive and convective terms with respect to the mesh size, and hence the need of additional diffusion in certain flow directions. In contrast, the edge-oriented stabilization can be seen in the framework of strengthening the continuity for the nonconforming space, so that the adding of the stabilization terms is more related to the structure of the FEM space, rather than to the local Reynolds number. Moreover, another interpretation is that - in contrast to this local Re number approach - the additional stabilization is mainly due to the smoothness of the (discrete) solution such that not the amount of convection, but of smoothness of the solution is the driving force. This could explain why the accuracy achieved for the computation of the drag and lift coefficients is much higher since the solution is quite smooth for this flow configuration.

For summarizing these tests for stationary flow configurations with low Re numbers, we finally test our proposed unified stabilization term in (5.5) with a wide range of 'free' constants γ for both flow around cylinder configurations, that means again for $Re = 1$ and $Re = 20$: Here, we set $\gamma^* = 10\gamma$ (see (5.5)). Then, Table 5.6 illustrates for the proposed edge-oriented stabilization that:

- the accuracy is surprisingly quite independent of the 'free' parameter γ which means that variations of γ between 0.0001 and 0.01 are permissible.
- the multigrid solver is also working perfectly up to a 'small' sensitivity with respect to over-stabilization, which means $\gamma \geq 0.01$.

Table 5.6. Drag and lift coefficients and multigrid convergence results with the proposed unified jump term $\sum_{\text{edge E}} \gamma \max(10\nu h_E, h_E^2) \int_E [\nabla \boldsymbol{u}][\nabla \boldsymbol{v}] d\sigma$

Level		drag			lift			solver	
γ	0.0001	0.001	0.01	0.0001	0.001	0.01	0.0001	0.001	0.01
deformation formulation, $Re = 1$									
3	3104.5	3110.5	3171.5	30.060	30.132	31.049	4/3	3/2	3/4
4	3132.5	3133.6	3147.7	30.658	30.668	30.908	4/3	4/2	3/6
5	3139.9	3139.9	3142.2	30.813	30.810	30.863	4/3	4/2	3/6
6	3141.8	3141.6	3141.5	30.852	30.849	30.857	4/4	4/2	4/12
gradient formulation, $Re = 1$									
3	3085.4	3091.6	3153.0	29.583	29.803	31.186	4/3	4/2	3/10
4	3127.5	3128.2	3140.7	30.535	30.613	31.066	4/2	4/2	3/9
5	3138.6	3138.2	3139.2	30.783	30.813	30.966	4/2	4/2	3/9
6	3141.4	3141.0	3140.2	30.846	30.858	30.914	4/2	4/2	3/7
deformation formulation, $Re = 20$									
3	5.5911	5.5886	5.5949	0.007992	0.008344	0.009213	12/3	12/3	12/13
4	5.5844	5.5815	5.5688	0.009890	0.009934	0.010087	12/2	12/2	12/11
5	5.5809	5.5795	5.5725	0.010430	0.010417	0.010375	12/2	12/2	12/8
6	5.5799	5.5793	5.5759	0.010571	0.010559	0.010501	12/2	12/2	12/8
gradient formulation, $Re = 20$									
3	5.5865	5.5865	5.5855	0.007331	0.007938	0.009155	12/3	12/3	12/13
4	5.5850	5.5818	5.5651	0.009698	0.009802	0.010075	12/3	12/3	12/11
5	5.5811	5.5797	5.5709	0.010379	0.010376	0.010376	12/2	12/2	12/9
6	5.5799	5.5794	5.5753	0.010558	0.010548	0.010503	12/2	12/2	12/8

Stationary flow around a cylinder: Non-Newtonian case

We again consider the case of low Re numbers while the viscosity now has the form:

$$\nu(p, D_{\mathrm{II}}(\boldsymbol{u})) = (\epsilon + \frac{1}{\sqrt{\epsilon + \exp(\beta\, p))}} + D_{\mathrm{II}}(\boldsymbol{u}))^{\frac{r}{2}-1} \tag{5.14}$$

Then, the results in Table 5.7 essentially confirm our previous results (see section 3.6.3, [73]), namely that the local evaluation ν_{local} of the (nonlinear) viscosity leads to improved results regarding the nonlinear and particularly the linear solution behavior, and that the 'free' parameter γ does not have a significant influence onto the convergence rates for a wide range of values.

Table 5.7. NL/AVMG for pressure and shear-dependent viscosity

γ	0.0	0.0001	0.001	0.01	0.0001	0.001	0.01
Level	no stab		ν_{local}			ν_{const}	
			r=3.0				
3	7/6	7/2	7/2	6/2	6/2	6/2	5/2
4	7/19	6/2	6/2	6/2	7/2	6/2	6/3
5	7/51	7/2	6/2	6/2	7/3	7/2	6/3
6	9/108	7/2	7/2	6/2	10/1	7/2	5/3
			r=1.5				
3	7/7	6/2	7/2	7/2	6/2	6/2	5/2
4	8/22	7/2	7/2	7/2	7/2	6/2	6/3
5	9/61	7/2	7/2	6/2	7/2	7/2	6/3
6	14/65	11/1	9/1	6/2	10/1	7/2	5/3
			r=1.1				
3	12/6	14/2	15/2	11/2	11/2	9/2	7/3
4	16/11	17/2	15/2	12/2	13/2	9/2	7/4
5	20/23	18/2	15/2	13/3	14/2	10/4	8/6
6	24/44	19/2	14/2	12/3	15/2	11/3	10/7

Nonstationary flow around a cylinder: $Re = 100$

Next we analyze the nonstationary case of periodically oscillating flow for a medium Reynolds number, here $Re = 100$ for the 'flow around cylinder' benchmark [100], with the aim to examine the (spatial) accuracy of the different stabilization techniques. The simulation is performed for $T = [0, 3]$, started with a fully developed solution, for different levels of mesh refinement; here, we perform a fully implicit approach (see [99]) with small time stepping size to minimize the influence of errors coming from the time discretization. Figure 5.2 shows the time-dependent plots for the lift force values - the most critical quantity in these tests [100] - for different mesh levels and for different stabilization techniques, while Table 5.8 provides the maximum amplitudes and the Strouhal number (for the frequencies) of the lift value for this periodically oscillating flow.

Table 5.8. Maximum amplitude and Strouhal number for the lift value for $Re = 100$

stab.	$j_{2,2}$	SD	UPW	$j_{2,2}$	SD	UPW
Level	Maximum amplitude			Strouhal number		
3	0.8750	0.3171	0.2543	0.29126	0.25862	0.23904
4	0.9753	0.6878	0.8214	0.29810	0.26906	0.28436
5	0.9858	0.8864	0.9664	0.30075	0.28708	0.29557
reference values		~ 1.0060			~ 0.3020	

These results clearly show that also in this case of medium Re numbers which lead to self-induced periodically oscillating flow, the edge-oriented stabilization is significantly more accurate than the applied upwinding, respectively streamline-diffusion variants. Particularly on coarse meshes, the differences with respect to the amplitude and especially the frequency ('Strouhal number') of the oscillations are clearly visible and recommend this new approach for fully time-dependent flow configurations in the range of medium Re numbers.

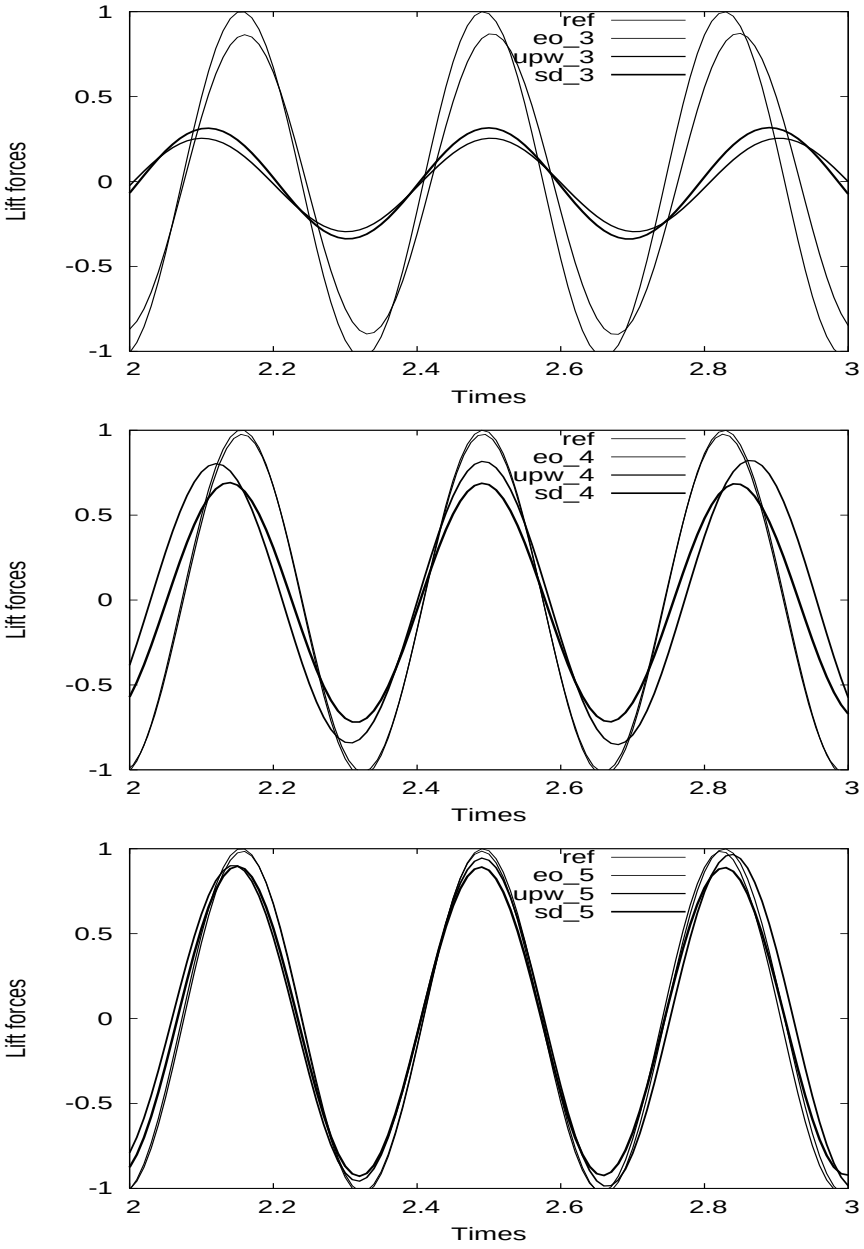

Fig. 5.2. Reference results for lift versus results for the different stabilizations (in gradient formulation) for SD-0.1, UPW-0.1 and edge-oriented stabilization EO-0.1

5.4.2 Driven cavity

Driven cavity flows represent a common benchmark test case for incompressible CFD codes and therefore we would like to present some corresponding results for $Re = 1/\nu = 2,000$ concerning the accuracy of the approximate solution with respect to different stabilization techniques. The accuracy of the approximation is evaluated by comparing the energy for each stabilization. We list in Table 5.9 the energy of the velocity which consist of the L_2-norm of the velocity for different stabilization techniques and different relaxation parameters. The simulation is performed on a unit square with uniformly refined mesh $2^{\text{Level}} \times 2^{\text{Level}}$.

Table 5.9. Energy of the velocity in the driven cavity for $Re = 2,000$

stab.	Upwinding (δ^*)		Streamline diffusion (δ^*)			Edge-oriented (γ)			
Element	mean-value		mean-value			midpoint		mean-values	
	on edges as d.o.f's		on edges as d.o.f's			on edges as d.o.f's		on edges as d.o.f's	
Level	0.1	1.0	0.25	1.0	4.0	0.001	0.01	0.001	0.1
3	0.14613	0.14613	0.22315	0.23691	0.24761	0.22283	0.24853	0.24882	0.25212
4	0.33857	0.34054	0.16449	0.17588	0.16460	0.24668	0.26308	0.28623	0.26757
5	0.34357	0.35334	0.20732	0.20112	0.15907	0.26904	0.33373	0.29941	0.34426
6	0.34402	0.36415	0.23863	0.22649	0.18540	0.28074	0.33573	0.29717	0.34241
7	0.33675	0.36642	0.26850	0.25283	0.21393	0.29078	0.31536	0.29785	0.31799
8	0.32215	0.35579	0.27518	0.27518	0.24328	0.29829	0.30609	0.30066	0.30707
9	0.31081	0.33564	0.29831	0.29068	0.26954	0.30213	0.30415	0.30272	0.30452

As can be seen from Table 5.9, the upwinding approximation overestimates the energy for both relaxation parameter values $\delta^* = 0.1$ and $\delta^* = 1.0$, while the streamline diffusion approximation underestimates the energy for all relaxation parameter values $\delta^* = 0.25$, $\delta^* = 1.0$ and $\delta^* = 4.0$. Similarly to all others benchmark simulations, better results are obtained by the edge-oriented approximation. The unsurpassable degree of accuracy for edge-oriented method is independent of the relaxation parameter values and the type of elements. Moreover, the method neither overestimates nor underestimates the energy.

We now turn our attention to the convergence rates for the edge-oriented stabilization and increase the Reynolds number up to 10 000. Table 5.10 shows the number of nonlinear iteration versus the average number of multigrid sweeps for both linearization methods Newton and fixpoint. The fixpoint simulations has been done with a damping factor which has to be chosen small enough to guarantee the convergence of the iteration procedure. In contrast, the Newton simulations has been performed without any damping furthermore the accuracy for the linear solver was adapted to the nonlinear convergence rate: In fact, if Res^l is the residue on l^{th} nonlinear iteration, with the assumption that Newton gives quadratic convergence the next reduction of the residue should be of order ρ^2 where $\rho = Res^l/Res^{l-1}$. Therfore, we require that the approximation of linear solver to be only of order ρ^2. Moreover, for the first few iterations we only apply fixpoint and switch to full Newton as soon as we reach some given tolerance. This strategy prevents the potential run away for Newton's method.

Table 5.10. Nonlinear convergence results with edge-oriented stabilization for different Reynolds numbers and type of elements for driven cavity benchmark configuration

Scheme	Newton					fixpoint				
Level/ Re	200	1 000	2 000	5 000	10 000	200	1 000	2 000	5 000	10 000
	mean-value on edge as d.o.f's , NL/ANL									
3	5/2	6/3	5/2	5/2	5/2	20/1	29/1	28/1	27/1	26/1
4	5/1	6/3	7/4	6/5	6/6	14/1	45/2	53/2	65/2	66/2
5	5/1	7/3	6/4	6/5	6/7	13/1	40/2	41/2	50/2	55/1
6	5/2	7/2	6/4	6/5	6/8	12/1	34/2	47/1	62/2	52/2
7	4/2	7/2	6/3	7/6	7/5	12/1	30/1	43/1	53/2	80/2
8	4/2	7/2	6/3	6/5	8/5	11/1	27/1	36/1	39/2	90/3
9	4/2	6/1	5/2	6/3	7/3	17/1	37/1	35/1	41/1	56/2
	midpoint on edge as d.o.f's , NL/ANL									
3	5/2	5/2	5/2	5/2	4/2	14/1	18/1	16/1	16/1	15/1
4	5/2	6/5	5/4	5/5	6/5	13/1	26/2	26/2	27/2	26/2
5	5/2	7/5	6/7	6/9	6/11	13/1	36/2	34/2	35/2	34/2
6	5/2	7/3	6/6	6/11	6/15	13/1	34/2	34/2	39/2	39/2
7	4/2	7/3	6/5	7/10	6/11	12/1	31/1	32/2	49/3	59/3
8	4/2	7/2	6/4	6/7	8/4	11/1	27/1	33/2	37/2	94/3
9	4/2	7/2	5/2	6/5	9/6	17/1	37/1	36/1	42/2	53/3
	mean-value on edge as d.o.f's , Energy $\|\boldsymbol{u}\|_0$					midpoint on edge as d.o.f's , Energy $\|\boldsymbol{u}\|_0$				
3	0.26053	0.25045	0.24882	0.24756	0.24708	0.25550	0.24800	0.24726	0.24678	0.24661
4	0.26053	0.28124	0.28623	0.29027	0.29185	0.25785	0.27624	0.28165	0.27835	0.28764
5	0.26166	0.29173	0.29941	0.30803	0.31222	0.26126	0.30649	0.32713	0.35254	0.36586
6	0.26219	0.29301	0.29717	0.30142	0.30442	0.26216	0.30294	0.32048	0.35035	0.37469
7	0.26238	0.29511	0.29785	0.29645	0.29439	0.26238	0.29848	0.30766	0.32516	0.34517
8	0.26244	0.29695	0.30066	0.29873	0.29329	0.26244	0.29781	0.30363	0.30994	0.31792
9	0.26246	0.29788	0.30452	0.30297	0.29848	0.26246	0.29807	0.30349	0.30656	0.30775

The rapid convergence of Newton's method can be appreciated by looking at the number of nonlinear iterations which is in fact independent of the Reynolds numbers. Furthermore, since at least the first two iterations were done with fixpoint we could conclude that we were able to establish the quadratic convergence of this method. In addition we achieved an optimal computational cost associated with solving the linear system: This is due to the fact that we were using the adaptative strategy tuning the accuracy of the linear solver to that required for the nonlinear solver. In contrast, for the fixpoint method the nonlinear convergence rate is strongly depending on the Reynolds numbers.

We would like to mention that the simulations were done with the cell-oriented Vanka smoother which incorporates only a part of the jump matrix in the preconditioning which may be insufficient. Firstly, due to the possible convection dominated effect which occur at high Reynolds numbers. Secondly, because of the additional bilinear forms associated with Newton linearization. As an alternative, one would incorporate the full part of the stabilization in the preconditioning step by using the proposed edge-oriented Vanka smoother. Moreover, it is possible to speed up the quadratic convergence rate of the Newton method to cubic specifically for $\rho > 1 \times 10^{-1}$ [43, 42, 2].

5.4.3 Standing vortex: $Re = \infty$

To verify the advantageous dissipative properties of the edge-oriented stabilization approach, we consider as the next test configuration the well known 'Standing Vortex' problem [36]. In this case the incompressible Navier-Stokes equations for inviscid flow ($Re = \infty$) are solved in a unit square

$$\frac{\partial \boldsymbol{u}}{\partial t} + \boldsymbol{u} \cdot \nabla \boldsymbol{u} + \nabla p = 0, \quad \nabla \cdot \boldsymbol{u} = 0 \qquad \text{in } \Omega = (0,1) \times (0,1). \tag{5.15}$$

The initial condition is an axisymmetric vortex which also represents the exact steady-state solution. In polar coordinates, the velocity $\boldsymbol{u}$ can decomposed into the radial component $\boldsymbol{u}_r$ and the angular component $\boldsymbol{u}_\theta$ which are initialized by

$$\boldsymbol{u}_r = 0, \quad \boldsymbol{u}_\theta = \begin{cases} 5r, & r < 0.2, \\ 2 - 5r, & 0.2 \le r \le 0.4, \\ 0, & r > 0.4, \end{cases} \tag{5.16}$$

where $r = \sqrt{(x-0.5)^2 + (y-0.5)^2}$ denotes the distance from the center. The aim of the following simulations is to check which discretization scheme is able to preserve the original vortex.

The numerical results produced by the different stabilization techniques are compared with the exact solution in Fig. 5.3. They were obtained at $T = 3$ on an equidistant mesh of 64×64, 128×128, and 256×256 quadrilateral elements respectively. A fully implicit time stepping approach (see [99]) with small time steps was used to eliminate the influence of temporal discretization errors. Since in this configuration the local Re number is not defined ($Re_T = \infty$), the upwinding scheme deteriorates towards the simple first-order upwind method which is however monotone and oscillation-free. In the case of the streamline-diffusion scheme, we cancelled the relation to the local Re number. Instead, we multiplied the stabilization term by $\delta_T = \delta^* \cdot h_T$ (compare with (2.53)), and thus we only varied the value of δ^* in the following calculations.

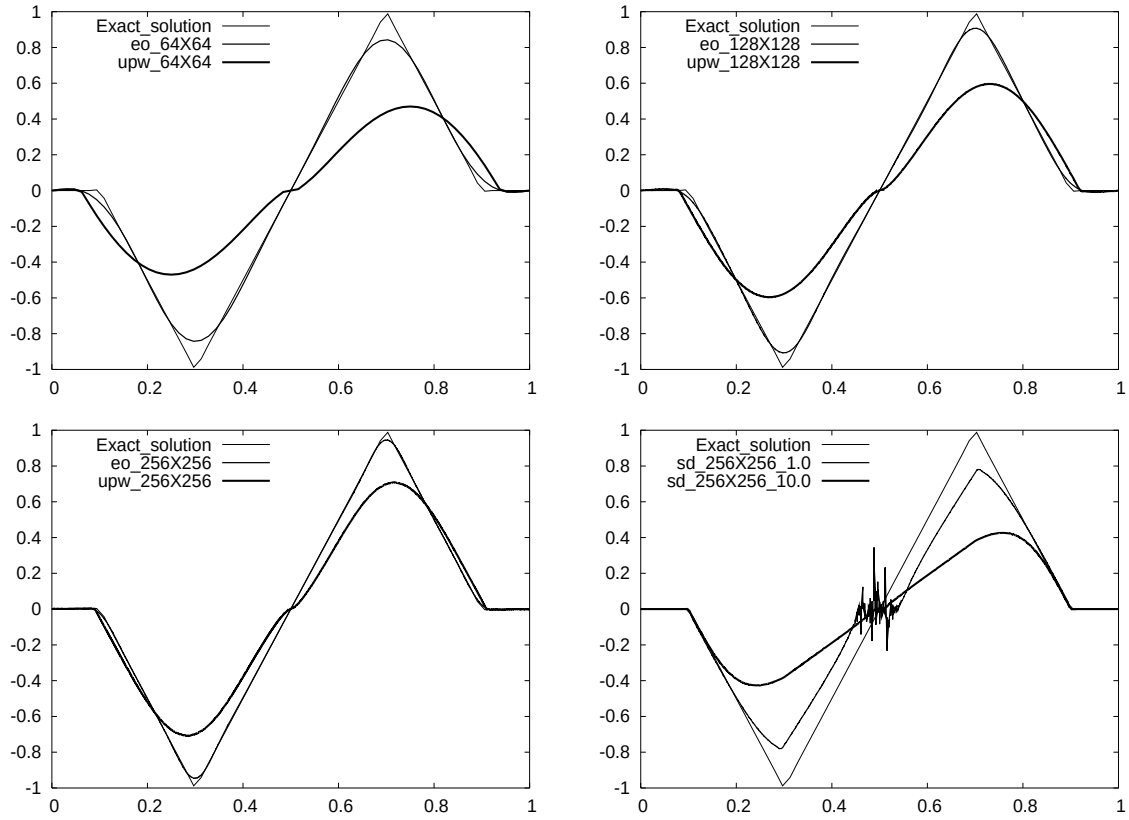

Fig. 5.3. Cutline of the x-velocity component for the 'Standing Vortex' problem: Comparison of the different stabilization techniques for different mesh levels

The results show the enormous potential of the edge-oriented stabilization for this type of flow problems. It is obvious that the (first order) upwinding and also the streamline-diffusion method (here: with $\delta^* = 10$) introduce, as expected, too much artificial diffusion (keep in mind that the exact velocity components should have an absolute value of 1). Therefore, one might try to reduce the amount of numerical diffusion of the streamline-diffusion approach by using smaller values for the parameter δ^*. However, in that case, severe spurious numerical oscillations in combination with massive over- and under-shooting of the solution arise and render the discrete approximation to be worthless (see the corresponding snapshots in Fig. 5.4). Moreover, and very surprisingly for us, massive problems occur in the center of the domain where the exact solution is very smooth and the sign of the velocity components changes. For this configuration the physically correct solution is a so-called *transonic rarefraction* solution [63] where the discrete approximation leads to *entropy violating shocks* which requires special techniques for an entropy fix. This problem can be clearly seen in Fig. 5.3, where at the center ($x = y = 0.5$) the solutions coming from the upwinding, respectively streamline-diffusion approaches cannot reproduce the linear shape. In contrast, the edge-oriented approach does not show any problem in this case which is very amazing and requires more numerical studies.

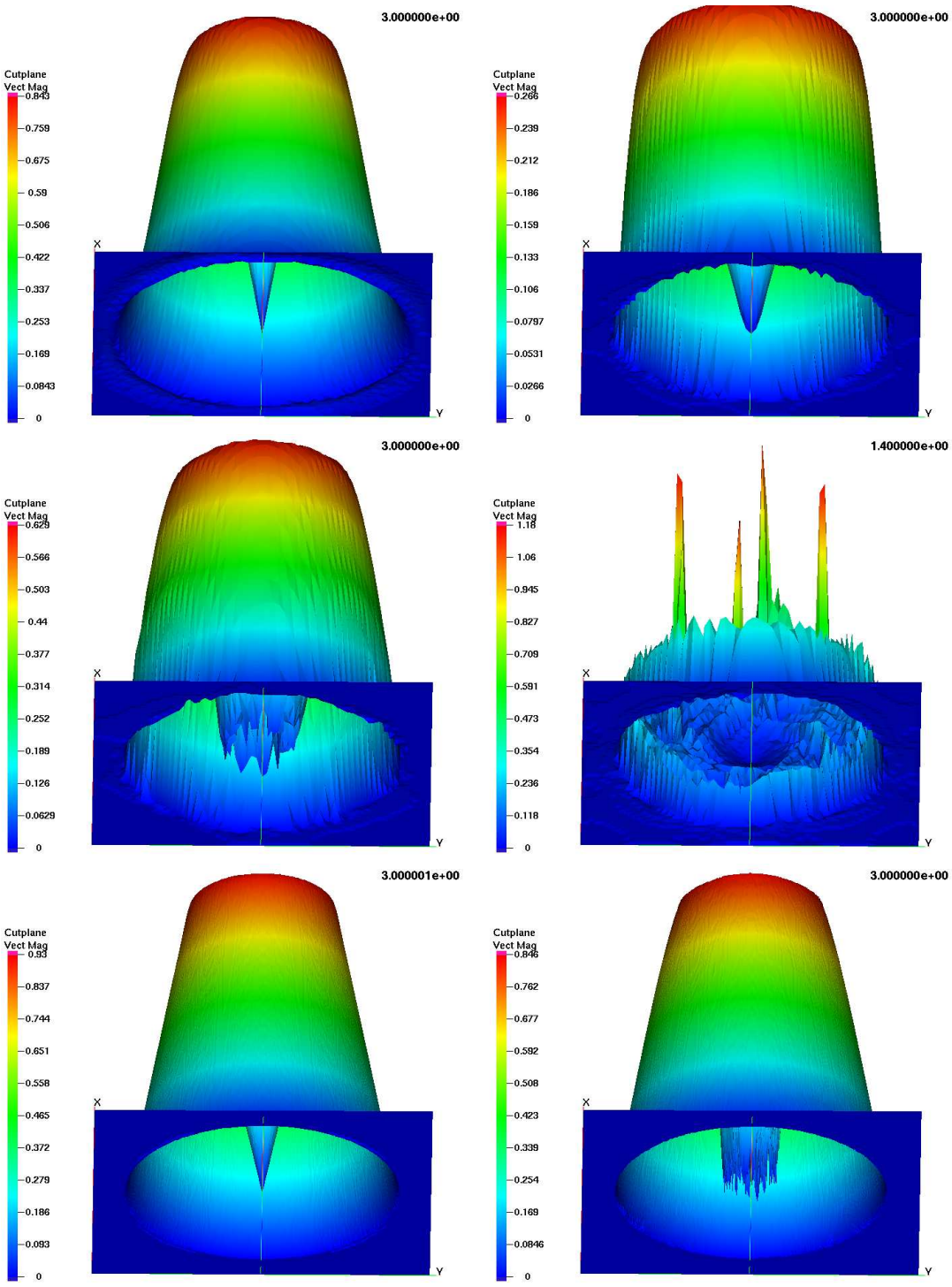

Fig. 5.4. 3D presentation of the norm of the velocity (Vect Mag) for the 'Standing Vortex' problem: edge-oriented versus streamline-diffusion ($\delta^* = 10$) for $h = 1/64$ (top), streamline-diffusion with $\delta^* = 0.5$ and $\delta^* = 0$ (= central differencing) for $h = 1/64$ (middle) and edge-oriented versus streamline-diffusion ($\delta^* = 0.5$) for $h = 1/256$ (bottom)

5.5 Conclusions and outlook

Egde-oriented stabilization approaches, including jump terms of the gradient on the edges of the computational mesh, together with low order nonconforming FEM spaces have been numerically analyzed for incompressible flow problems. The computational tests considered cases of various Re numbers (ranging from $Re = 1$, resp. Stokes flow, over medium Re numbers with periodically oscillating flow phenomena up to the case '$Re = \infty$') and formulations including the gradient as well as the symmetric deformation tensor ('Korn's inequality') of the velocity. We also examined non-Newtonian problems with pressure and shear-dependent viscosity. The proposed edge-oriented stabilization term involves only the gradient of discrete test and trial functions (leading to reduced assembling costs), which together with a special parameter setting taking into account the local size of the viscosity, if available, requires only one 'free' parameter γ. The numerical tests for various prototypical problems settings have shown that, in contrast to classical stabilization schemes of upwinding or streamline-diffusion type, the influence of this parameter onto the resulting accuracy, robustness and efficiency is surprisingly small.

Summarizing these computational tests, we have shown that with this special edge-oriented FEM stabilization method:

- we can stabilize the lack of coercivity ('Korn's inequality') for problems formulated in terms of the symmetric part of the velocity gradient.
- we can handle problems for most relevant Re numbers, even in the limit of inviscid flow.
- we can successfully realize strategies for simulating non-Newtonian flow with pressure and shear-dependent viscosity.
- we can solve the resulting linear generalized Oseen problems in conjunction with standard multigrid components which preserve the original FEM data structure.

Based on these positive results for a wide range of typical flow simulations, we can state that the proposed stabilisation technique may be an interesting candidate for black-box components in CFD codes. Therefore, one future aim is to study the corresponding numerical behavior with respect to accuracy and robustness in cases of the turbulence effects, visco-elastic fluids and multiphase flow settings including pure transport problems which are coupled with the Navier-Stokes equations.

Part II

Applications: Granular and powder flow

6

Incompressible Powder Flow

The flowing of powders brings a new challenging and interesting problem to the CFD community: at very high concentrations and low rate of strain, grains are in permanent contact, rolling on each other. Therefore a frictional stress model must be taken into account. This can be done using plasticity and similar theories in which the granular material behavior is assumed to be independent of the velocity gradient or the rate-of-strain. This is in contrast to viscous Newtonian flow where stress specifically depends on rate-of-strain. Furthermore, unlike fluids, flowing powders do not exhibit viscosity and, again, this shows that a Newtonian rheology cannot describe granular flow accurately.

It is assumed that the material is incompressible, dry, cohesionless, and perfectly rigid-plastic. Based on continuum theories, equations for such material have been derived which closely resemble the generalized Navier-Stokes equations with pressure and shear depend viscosity.

Thus the resulting equations are mathematically more complex than the Navier Stokes equations and are only valid when the material is deforming. In this chapter we apply the numerical algorithms and simulation techniques developed in Part I to approximate these highly nonlinear equations. A Newton linearization technique was applied directly to the corresponding continuous variational formulations. The approximation of incompressible velocity fields was treated by using stabilized nonconforming Stokes elements and we use a Pressure Schur Complement smoother as defect correction inside of a direct multigrid approache to solve the linear saddle-point problems with high numerical efficiency. The results of some computational experiments for realistic flow configurations are provided.

6.1 Physical background

6.1.1 Mohr-Coulomb criterion for friction

The Mohr theory suggests that the shear stress on a failure reaches some unique function of normal stress, $\tau = f(\sigma)$, where τ is the shear stress and σ is the normal stress. Coulomb found that for frictional motion the yield shear stress can be expressed as a combination of a normal stress dependent component and a stress independent component. While the normal stress dependent component is connected with the internal angle of friction ϕ, the former seems to be related to the intrinsic cohesion and is denoted by the symbol c. Then, the Coulomb equation reads

$$\tau = \sigma \tan \phi + c, \tag{6.1}$$

where ϕ and c are the material constants defined as the angle of internal friction and the cohesive strength respectively: A material is called non-cohesive if $c = 0$. Eq. (6.1) represents the simple law of friction of

two solids sliding on each other with the shear force proportional to the normal force where $\eta = \tan\phi$ is the friction coefficient. A similar condition also exists at the interface between the granular material and the walls of the container: here only the angle of internal friction is replaced by the angle of wall friction ϕ_W. The angle satisfies $\phi_W < \phi$ since the wall is usually less rough than a powder layer which is mainly due to the void fraction near the wall.

6.1.2 Regimes of powder flow

Similar to fluid flow, where several characteristic numbers, like Froude number, Reynolds number, etc., can be used to characterize the qualitative flow behavior, the various powder regimes can be represented as a function of a dimensionless shear rate $\gamma^{o*} = \gamma^o[d_p/g]^{1/2}$ which contains a gravitational term g and a particle size d_p (see Tardos et al. [89]). Based on such a characterization, one has the following three different regimes.

Quasi-static regime

This regime is valid when the flow is slow enough so that any movement between two static states can be neglected: In this case the static equilibrium equation can be applied. With this approach only stress and condition of the onset of flow can be computed, while no flow field can be predicted which circumscribes the range of applications of this approach. There is a large number of analytical and numerical solutions to this case and an important number of literature devoted to this regime, see for instance [67],[34].

Slow and frictional regime

In this regime the frictional forces between particles are predominant, so the inertial effect is added to the static equations as well as the consideration of continuity beside a yield condition. The first model invoking a flow rule was introduced by Schaeffer (1987) [79]. This regime is very important since it can be used for modeling a wide range of practical phenomena and industrial applications. However, for the serious challenges which arise in this regime, for instance ill-posed partial differential equations and the prediction of stress fluctuations, there is still a lack of fundamental research so that dealing with these problems requires a multidisciplinary treatment. Our contribution has the goal of supporting this part by modern numerical methods which will be described in the subsequent sections.

Intermediate and rapid granular regimes

For the intermediate regime, additional to inter-particle friction energy, collision energy is also important. For the rapid regime, the short particle-particle contacts are important while frictional forces are neglected. This regime is often described via kinetic models and will not be treated here. It was reported here just to have a complete view on the different regimes of powder flow (see [89] for more details).

6.1.3 Flow rule: Saint Venant principle

The Saint Venant principle of solid mechanics says that stresses cause deformations preferentially in the same direction. This leads to the co-axiality flow rule condition which states that the principal directions of the stress and rate of deformation are parallel and neglects the rotation of a material element during deformation. In two-dimensional Cartesian coordinates, this condition takes the form, for example:

$$\frac{\mathbf{T}_{ii} - \mathbf{T}_{jj}}{\mathbf{T}_{ij}} = \frac{2(\partial u_1/\partial x - \partial u_2/\partial y)}{\partial u_1/\partial x + \partial u_2/\partial y} \tag{6.2}$$

This was postulated by Schaeffer [79] for the deformation of granular material. However, since the deformation of the granular material requires that the stresses in different directions must be different, Schaeffer claimed that ***"the response of the material to such unequal stresses should be to contract in the directions of greater stress and to expand in the directions of smaller stress".*** This reflects the requirement that the eigenvectors of stress tensor and strain rate are aligned and it quantitatively links the deviatoric stress and the strain rate tensor by the formula $\mathbf{S} = \lambda \mathbf{D}$.

6.1.4 Rigid perfect plastic behavior

Plastic deformation

The deformation of a granular material is considered to be plastic in the sense that, if after deformation the shearing stress is reduced, the material would not show any tendency to return to its original state. Plastic deformation was already proposed by E. C. Bingham, in 1922, in the context of non-Newtonian fluids, and in which the rheological behavior is governed by the following equation in modified state introduced by Oldroyd:

$$\mathbf{T} = -p\mathbf{I} + (\frac{\mu_0}{\|\mathbf{D}\|} + \mu)\mathbf{D} \qquad (\mu_0 > 0, \mu \geq 0). \tag{6.3}$$

Dilatancy

A simple manifestation of this phenomenon occurs when one leaves dry footprints while walking along a wet beach: the deformed sand dilates, therefore space between grains increases, allowing for upper water to invade the sand. As a consequence, footsteps get dry and water goes down. This is the phenomenon of dilatancy which was explained by Reynolds in 1885, and demonstrated experimentally: a glass tube attached to a balloon showed that the amount of excess water decreased when the sand was deformed, thus showing that deformation increases the space between grains. Dilatancy is important in the dynamics of granular material, introducing a stick-slip instability at low velocity (see [61]), and it occurs because each grain needs more space in the flowing state than at rest. Then, the flow theory of plasticity must be applied to the constitutive modeling for describing the deformation process of a granular material.

6.2 Constitutive equation for powder flow

6.2.1 Equation of motion

The powder is assumed to be an incompressible continuum that obeys conservation of mass and momentum (density ρ, gravity $\mathbf{g}$, velocity $\boldsymbol{u}$):

Conservation of mass: $\frac{D\rho}{Dt} = \frac{\partial \rho}{\partial t} + \nabla \cdot (\rho \boldsymbol{u}) = 0$.

Incompressible material: The bulk density, ρ, is a constant, so that $\nabla \cdot \boldsymbol{u} = 0$.

Equation of motion: With $\mathbf{T} = \mathbf{S} - p\mathbf{I}$, there holds $\rho \frac{D\boldsymbol{u}}{Dt} = \nabla \cdot \mathbf{T} + \rho \mathbf{g}$.

6.2.2 Constitutive equations

The constitutive equation shall correlate between the deviatoric tensor $\mathbf{S}$ and the velocity, through the second invariant of the rate deformation $D_{\mathrm{II}} = \frac{1}{2}\mathbf{D} : \mathbf{D}$, where the rate of deformation is given by $\mathbf{D} = \frac{1}{2}(\nabla \boldsymbol{u} + (\nabla \boldsymbol{u})^T)$. There are several examples:

Newtonian law: $\mathbf{S} = 2\nu_{\circ}\mathbf{D}$

Power law: $\mathbf{S} = 2\nu(D_{\mathrm{II}})\mathbf{D}, \quad \nu(z) = z^{\frac{r}{2}-1}, \quad r \geq 1 \quad (r = 1\text{: } \textbf{Bingham law})$

Schaeffer's law: For a powder, a constitutive equation was first introduced by Schaeffer [79] which has to obey a

- yield condition: $\|\mathbf{S}\| = \sqrt{2}p\sin\phi$,
- flow rule: $\mathbf{S} = \lambda\mathbf{D}$ with $\lambda \geq 0$.

In fact, the flow rule is based on a yield criterion for granular materials of von Mises type, which is basically derived from a law of sliding friction applied to the individual particles. Specifically in terms of the principal stresses σ_i, this condition is written as

$$\sum_{i=1}^{3}(\sigma_i - p)^2 \leq k^2p^2 \quad \text{with} \quad p = \frac{1}{3}\operatorname{tr}\mathbf{T} \tag{6.4}$$

where $k = \sqrt{2}\sin\phi$ is a characteristic constant of the material, and σ_i are the eigenvectors of $\mathbf{T}_{ij}$. For a material that deforms plastically, equality must hold in Eq. (6.4):

$$\sum_{i=1}^{3}(\sigma_i - p)^2 = k^2p^2 \tag{6.5}$$

Under plane strain $p = \frac{1}{2}(\sigma_1 + \sigma_2)$, we may consider a strictly 2D-yield condition:

$$(\sigma_1 - p)^2 + (\sigma_2 - p)^2 = 2p^2\sin^2\phi. \tag{6.6}$$

A constitutive equation between stress and strain rate was proposed for slow powder by Schaeffer [79]. This equation obeys the von Mises yield condition and the described flow rule:

$$\mathbf{T} = -p\mathbf{I} + \sqrt{2}p\sin\phi\frac{\mathbf{D}}{\|\mathbf{D}\|} \quad \text{if } D \neq 0. \tag{6.7}$$

In fact, the flow rule is assumed to have the form $\mathbf{T} = -p\mathbf{I} + \lambda\mathbf{D}$, where λ is a coefficient. To satisfy the yield condition of the given flow rule in terms of von Mises, i.e. $\|\mathbf{S}\| = \sqrt{2}p\sin\phi$, then there must hold:

$$\lambda = \frac{\sqrt{2}p\sin\phi}{\|\mathbf{D}\|}. \tag{6.8}$$

We use this correlation to obtain finally the constitutive equation $\mathbf{T} = -p\mathbf{I} + \sqrt{2}p\sin\phi\frac{\mathbf{D}}{\epsilon+\|\mathbf{D}\|}$, where ϵ is a typical (small) regularization parameter.

6.2.3 Generalized Navier-Stokes equations

The derived problem formulation can be stated in the framework of the generalized incompressible Navier-Stokes equations (we set $\rho = 1$):

$$\frac{D\boldsymbol{u}}{Dt} = -\nabla p + \nabla\cdot(\nu(p, D_{\mathrm{II}})\mathbf{D}) + \mathbf{g}, \quad \nabla\cdot\,\boldsymbol{u} = 0. \tag{6.9}$$

If we define the nonlinear pseudo viscosity $\nu(\cdot,\cdot)$ as a function of the second invariant of the rate of deformation D_{II} and the 'pressure' p, we can show that various materials can be ranged within different viscosity laws including powder:

- Power law defined for $\nu(z,p) = \nu_o z^{\frac{r}{2}-1}$,
- Bingham law defined for $\nu(z,p) = \nu_o z^{-\frac{1}{2}}$,
- Schaeffer's law (including the 'pressure') defined for $\nu(z,p) = \sqrt{2}\sin\phi\ pz^{-\frac{1}{2}}$.

A comparison of this equation with the Navier-Stokes equations reveals that the ordinary viscous terms, proportional to the viscosity and the velocity gradient, have been replaced by shear-rate independent terms which is quite remarkable, since it implies that an overall increase in the velocity leaves the stress unchanged. This also means that these equations are mathematically more complex than the Navier-Stokes equations and only apply when the material is deforming, for instance for granular flows in hoppers; these equations are only valid for the mass flow where the material is flowing throughout the hopper.

Mathematical challenges

The main mathematical problems of the incompressible powder model (see Eq. (6.9)) can be summarized in the following aspects. Some of the these points will be discussed in the next sections; for more details see Part I.

Mathematical analysis:
There is a lack of further research concerning the existence and regularity of solutions of such fluids except for special cases (see for instance [44]); furthermore the dynamic equations (6.9) show some instabilities (see Schaeffer in [80, 79]) which also requires further studies.

Singular viscosity:
The extra part, $\sqrt{2}p\sin\phi\frac{\mathbf{D}}{\|\mathbf{D}\|}$, of the stress tensor $\mathbf{T}$ is only well defined for non zero values of the rate of strain tensor and for positive pressure. Therefore, some stabilization techniques of singular phenomena due to the nonlinear viscosity are required. For the pressure, one may think about using a positive viscosity function in the pressure variable, described by $\exp(\beta p)$, and a small regularization parameter ϵ, that means $\frac{p}{\epsilon+\|\mathbf{D}\|}$ or $\frac{\exp(\beta p)}{\epsilon+\|\mathbf{D}\|}$.

Discretization method:
It is well known that the computation of solutions of incompressible systems requires that special care is taken in the choice of the approximating spaces in order to make the discrete problem well posed (inf-sup condition). Moreover, since many FEM spaces satisfying the above condition are nonconforming, which however present a locking phenomenon for problems involving the rate of deformation tensor ('Korn's inequality'), some consistent stabilization term is required.

Nonlinear solver:
For this highly nonlinear problem coupling the pressure and velocity even in the viscous term, there is almost no alternative to Newton techniques [72]. However, the derivation of the corresponding Jacobian matrices due to the complex material laws is not clear.

Linear multigrid solver:
Efficient multigrid methods for saddle-point problems are required which however are nonsymmetric due to the Newton linearization and contain a variable viscosity function.

6.3 Ill posedness of the incompressible granular flow equation based on Schaeffer model

The material in this section was originally given by Schaeffer [79]. We report here in a compact form the analysis of instabilities concerning general properties of the partial differential equations analogous

to the classification of equations into elliptic, hyperbolic, and parabolic character. The test for linear instability was performed using the mode analysis and looking for an eigenvalue with a positive real part for a solution with exponential dependence $e^{i(\xi,x)+\lambda(\xi)t}$.

Stokes equation: To guide the analysis, let us consider the linearized equations:

$$\begin{pmatrix} -\mu|\xi|^2 I & \xi \\ \xi^T & 0 \end{pmatrix} \begin{pmatrix} \boldsymbol{u} \\ p \end{pmatrix} = \lambda \begin{pmatrix} \boldsymbol{u} \\ 0 \end{pmatrix}. \tag{6.10}$$

The eigenvalue λ is then obtained as $\lambda = -\mu|\xi|^2$, which means that the Stokes equations are linearly well-posed.

Granular case: In contrast the linearized equations of motion of the granular case lead to the generalized eigenvalue problem [79]

$$\begin{pmatrix} -\frac{k}{\|\mathbf{D}\|}\left[\frac{|\xi|^2}{2} I + (A\xi)(A\xi)^T\right] & (I + kA)\xi \\ \xi^T & 0 \end{pmatrix} \begin{pmatrix} \boldsymbol{u} \\ p \end{pmatrix} = \lambda \begin{pmatrix} \boldsymbol{u} \\ 0 \end{pmatrix} \tag{6.11}$$

where $A = \mathbf{D}/\|\mathbf{D}\|$ and $k = \sqrt{2}\sin\phi$. Similarly computing λ as before, one obtains:

$$\lambda = -\frac{\sqrt{2}\sin\phi}{\|\mathbf{D}\|}\left[\frac{(A\xi,\xi)^2 - \frac{1}{2}|\xi|^2(A\xi,\xi)}{|\xi|^2 + \sqrt{2}\sin\phi(A\xi,\xi)}\right]. \tag{6.12}$$

The presence of the factor $(A\xi,\xi)$ leads to an indefinite quadratic form in the numerator since $\operatorname{tr} A = 0$ and $\operatorname{tr} A^2 = 1$. From this we can conclude that the two-dimensional granular flow equations are linearly ill-posed (see [79] for more details).

6.4 FEM for the numerical simulations

The range of practical real world problems which involve granular materials is growing, and since the considered problems become more complex and experimentally more expensive, one is particularly interested in the development of new and more powerful computational methods for solving these problems numerically. In this section we show that our numerical approaches based on FEM techniques expounded in Part I are well suited to address the illustrated type of nonlinear powder problems and lead to comparative results with related experiments. We consider the following two configurations, powder flow in a Couette device with an obstacle see Fig. 6.1 and granular flow in a hopper see Fig. 6.3.

6.4.1 Boundary conditions

The boundary conditions in any incompressible fluid simulation are expressed either in terms of the fluid velocity or the pressure at the boundary, but generally both of them cannot be used at the same boundary since the velocities are influenced by the pressure gradient (see [41]). For the Navier-Stokes equations with Dirichlet velocity data, the pressure is unique up to a constant which however can be chosen arbitrarily. In contrast, for the flow of the generalized Navier-Stokes equations with pressure dependent viscosity, the choice of fixing the pressure cannot be done by random choice (see Table 6.1).

Remark 1. The choice of boundary condition for higher order models (compared to Navier-Stokes model) is a problem, which is not completly discussed up to now. What can happen for fluids of different type is recounted, for example, in Fosdick and Rajagopal [30].

Table 6.1. The dependence of the drag force from various rotational speed V at different mean pressure values

Speed / pressure	0.5	1	5	10	100
			Stokes law without convection		
0.05	0.62877D+01	0.62877D+01	0.62877D+01	0.62877D+01	0.62877D+01
0.1	0.12575D+02	0.12575D+02	0.12575D+02	0.12575D+02	0.12575D+02
0.2	0.25151D+02	0.25151D+02	0.25151D+02	0.25151D+02	0.25151D+02
0.5	0.62877D+02	0.62877D+02	0.62877D+02	0.62877D+02	0.62877D+02
			Bingham law without convection		
0.05	0.38137D+01	0.38137D+01	0.38137D+01	0.38137D+01	0.38137D+01
0.1	0.38222D+01	0.38222D+01	0.38222D+01	0.38222D+01	0.38222D+01
0.2	0.38252D+01	0.38252D+01	0.38252D+01	0.38252D+01	0.38252D+01
0.5	0.38265D+01	0.38265D+01	0.38265D+01	0.38265D+01	0.38265D+01
			Schaeffer law without convection		
0.05	0.50419D+00	0.10084D+01	0.50419D+01	0.10084D+02	0.10084D+03
0.1	0.50629D+00	0.10126D+01	0.50628D+01	0.10126D+02	0.10126D+03
0.2	0.50756D+00	0.10151D+01	0.50755D+01	0.10151D+02	0.10151D+03
0.5	0.50849D+00	0.10170D+01	0.50849D+01	0.10170D+02	0.10170D+03

Wall boundary conditions

The fundamental assumption in fluid mechanics for flow past solids is a "no-slip" boundary condition, which means that the tangential component of the fluid velocity equals of the solid at the surface. This well-accepted no-slip boundary condition may not be suitable for highly sheared flow, but the error due to the "no-slip" assumption is relatively small in big systems or if we are more interested in the flow far away from the wall. An alternative and more suitable condition is to apply slip with friction parameter β:

$$\boldsymbol{v} \cdot \boldsymbol{\tau} + \beta^{-1} \boldsymbol{n} \cdot (2\nu(D_{\mathrm{II}}, p)\mathbf{D}(\boldsymbol{v}) - p\mathbf{I}) \cdot \boldsymbol{\tau} = 0 \quad \text{on } \Gamma_{wall}. \tag{6.13}$$

Moreover, the closing of the equations is required, because the related Dirichlet problem of Navier-Stokes equations is well known to possess no unique pressure solution due to the constraint $\operatorname{div} \boldsymbol{v} = 0$. The uniqueness is assured by fixing the pressure with the choice of mean pressure to be zero which however cannot be taken for the flow with pressure dependent viscosity, namely the Schaeffer law, since it leads to negative values of the pressure in some parts of the computational domain. The first remedy is to make the choice of mean pressure positive to assure a positive pressure in all regions of the computational domain. However, the question arises of the physical meaning of any choice for the mean pressure to get the closure of the equations with Dirichlet boundary condition since the mean pressure is part of the viscosity and, therefore, influences significantly the global flow behavior.

Inflow and Outflow boundary conditions

Numerical simulations of flow problems usually require the flow out of one or more boundary parts of the computational domain. At such "outflow" boundaries there arises the question of what constitutes a good boundary condition. The simplest and most commonly used outflow condition is that of a "natural" boundary, see [41] for an overview:

$$2\nu(D_{\mathrm{II}}, p)\boldsymbol{n} \cdot \mathbf{D}(\boldsymbol{v}) - p\boldsymbol{n} = 0 \quad \text{on } \Gamma_{out} \tag{6.14}$$

This boundary condition represents a smooth continuation of the flow through the boundary and occurs in the variational formulation of problem if one does not prescribe any boundary condition for the velocity at the outlet, known in the literature by the name "natural" or "do nothing" boundary condition. It must be stressed that the "do nothing" outflow boundary condition has no physical basis, rather it is a mathematical statement that may or may not provide the desired flow behavior. Particularly, "do nothing" boundary conditions have proven to lead to very satisfactory results in modeling parallel flows, see e.g., Turek [92], but they must always be viewed with suspicion since they contain the hidden condition that the mean pressure is zero across the outflow boundary. In particular, the condition of mean pressure to be zero across the outflow leads to negative values of the pressure, which causes problems for the numerical simulation of flow with pressure dependent viscosity, namely the Schaeffer model. As a natural remedy for this situation, one may consider a condition in which the mean pressure across the outflow coincides with the atmospheric pressure, that means $p_{atm} > 0$:

$$2\nu(D_{\mathrm{II}}, p)\boldsymbol{n} \cdot \mathbf{D}(\boldsymbol{v}) - p\boldsymbol{n} = p_{atm}\boldsymbol{n} \quad \text{on } \Gamma_{out}. \tag{6.15}$$

The above examples suggest that the ability to specify a pressure condition at one or more parts of the computational domain is an important aspect. This can be done in terms of *prescribed pressure drops* with corresponding variational formulations of very general type [41].

6.4.2 Drag force in powder flow

As we described before, granular materials can flow like fluids and resist the motion of objects moving through them. Since this retarding force, known as drag force $F_d = (\oint_{C_0} \mathbf{T}\boldsymbol{n}\, ds)_y$ with $(.)_y$ denoting the y-component, see Fig. 6.1, can be easily measured experimentally for a granular medium in a Couette device with an immersed cylinder [1], for this reason we choose this configuration for our computation: Although our simulation is only in 2D, a lot of characteristics of granular flow can be examined numerically such that at least qualitative comparisons can be obtained in future.

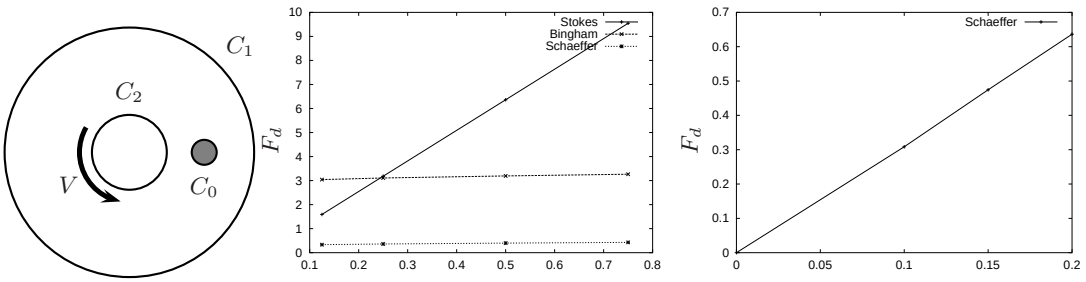

Couette device | Rotational speed V | Cylinder C_0 diameter

Fig. 6.1. Drag force F_d versus rotational speed V of the cylinder walls in a Couette device ('flow around a cylinder') for different material laws and for varying cylinder diameter. The inner cylinder C_2 is rotating with rotational speed V while the outer cylinder C_1 and the inner cylinder C_0 are fixed; all quantities are in non-dimensional form and shall provide qualitative comparisons only.

As expected, the drag force F_d for Schaeffer and Bingham flow acting on the cylinder C_0 is independent of the velocity, contrary to the (Newtonian) Stokes flow, while the drag force increases with larger diameters for the interior cylinder C_0.

"When mechanical ploughs replaced draught animals, it was observed that ploughing at greater speeds does not require greater forces!" (from Schaeffer 1987)

In Table 6.1, we show this behavior in detail: Here, we perform tests for various prescribed mean pressure values to obtain a unique solution, and for several rotational speeds. As explained before, the Stokes and Bingham model lead to drag forces which are independent of the given mean pressure while the Schaeffer model shows the expected dependence since the pressure is part of the viscous term.

Moreover, we also examine the influence of neglecting the convective terms in the Schaeffer model, that means $(\boldsymbol{u} \cdot \nabla \boldsymbol{u})$ in (3.1) which is typically done due to the assumption of "slow" flow. Here, we increase continuously the rotational speed V of the inner cylinder C_2 and plot in Figure 6.2 the behavior of the resulting drag force F_d for the Schaeffer model with and without convection. As can be seen, if we totally neglect the convective term, then the drag force remains constant with an absolute value which is independent of the prescribed velocity. In addition, at least for 'slow' flow, there is no difference between the Stokes and the full Navier-Stokes model, including the convective terms, while from a certain speed on, differences between both models get visible. So, it might be interesting for future experiments to check whether this calculated relation between drag force and increasing velocity can be actually observed, which is at least questionable since the Schaeffer model has only been theoretically derived for 'slow' (?) flow. However, from a numerical point of view, it is reasonable to include this convective part, too, in corresponding numerical modeling and simulation.

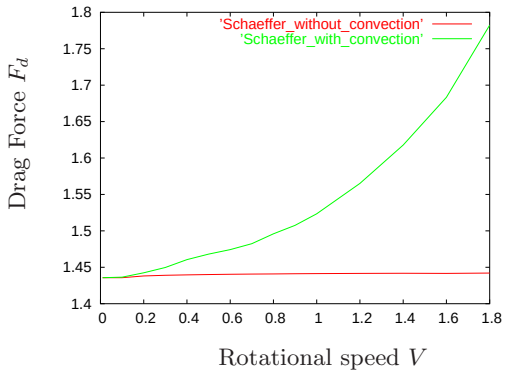

Fig. 6.2. Dependence of the drag force F_d from the rotational speed V for the Schaeffer model with and without convective term

6.4.3 Granular flow in a hopper

Flow of granular material in hoppers under gravity is quite complex and experimental approaches show limitations in understanding some phenomena for this type of geometry. Our current investigation is to understand some typical phenomena related to granular material, namely oscillating phenomena and instabilities, as for instance shear banding instabilities.

For the Schaeffer model, Figure 6.3 shows that the flow is significantly influenced by the pressure in the material law, in contrast to the Bingham model which is independent of it. To go deeper in understanding the instability phenomena we plot for different times the average stress for both models in Figure 6.4. These instabilities may be explained by the stability analysis of Schaeffer [80] who shows the previously illustrated ill-posedness of the problem. However, since we observe that these instabilities arise from the artificial inflow/outflow regions, the influence of the applied boundary conditions is not clear yet. Since the inflow and outflow boundary condition supplied to the hopper do not have any physical meaning, they could be the source of the appearance of the oscillations, too. We also examined a silo geometry with a much longer bin on the bottom and the top of the hopper to diminish the influence of the boundary conditions onto the flow behavior but the oscilations of the pressure in the hopper part remais. Further investigations could be directed toward multi-phase flows.

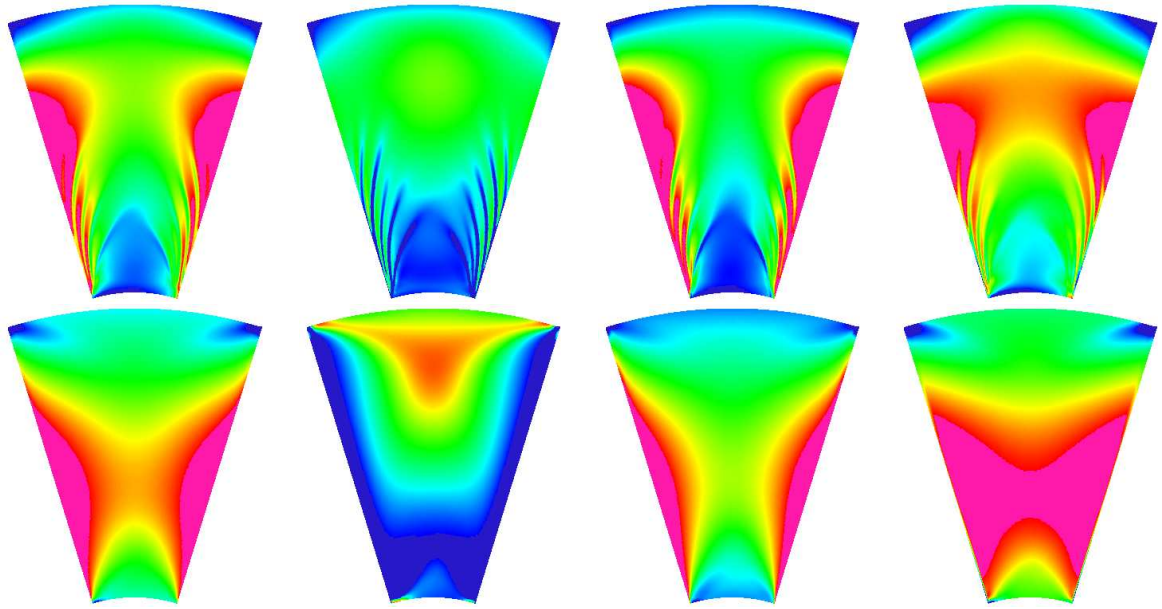

Fig. 6.3. The plot of the pressure, the pseudo viscosity (see (6.9)) and the components σ_{11}, σ_{22} of the stress at t=0.03s for Schaeffer (top) and Bingham law (bottom)

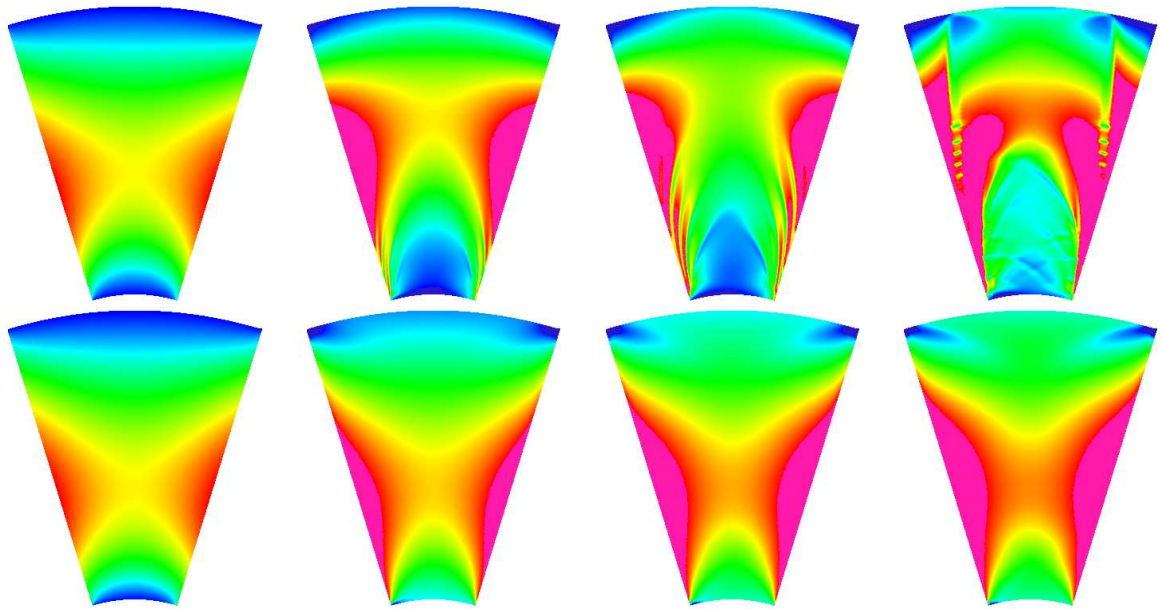

Fig. 6.4. Snapshots of the average stress at t=0.0s, 0.012s, 0.03s and 0.06s for Schaeffer (top) and Bingham law (bottom)

6.5 Conclusions

Our conclusion is that finite element methods together with special material laws can be useful tools for the numerical simulation of incompressible granular powder, since the complete structure of the flow is involved, i.e. the velocity, the pressure as well as the stress. Although our computer simulation is only two-dimensional it can confirm well known physical behavior, namely the independence of the drag force from the velocity grain and the propagation of a pressure wave in the hopper which may lead to a shear banding instability. At first glance, the shear banding phenomenon gives the impression to be treated mathematically as a discontinuity, but this would cause severe problems for numerical algorithms. On the other hand, shear bands might not be a true physical discontinuity, rather than a change in the involved physical system which could be captured with a compressible model.

Furthermore, the proposed incompressible model for granular and powder flow presents some other disadvantages, like for instance the wrong prediction of the flow rate through a symmetric silo by more than a factor of 4 in comparison with experiments [88]. This gives another motivation to proceed toward compressible granular materials which can be specified via the yield condition $q(p, \rho)$ given in Table 6.2 (see the work by Tardos and particularly [89] for the details).

Table 6.2. Yield condition $q(p, \rho)$ for incompressible and compressible powder $(0.001 < \beta < 0.01)$

Powder properties	Non-cohesive	Cohesive
Incompressible	$p \sin \phi$	$p \sin \phi + c \cos \phi$
Compressible	$p \sin \phi \left[2 - \frac{p}{\rho^{\frac{1}{\beta}}} \right]$	$p \sin \phi \rho^{\frac{1}{\beta}} - C \frac{(p - \rho^{\frac{1}{\beta}})^2}{\rho^{\frac{1}{\beta}}}$

Then, the flow can be described by a generalized compressible Navier-Stokes-like equation (6.16) where a mass conservation equation (6.17) must hold. However, this is not enough because the density ρ is now a dependent variable, rather than a constant:

$$\rho \frac{D\boldsymbol{u}}{Dt} = -\nabla p + \nabla \cdot \left[\frac{q(p, \rho)}{\left\| \mathbf{D} - \frac{1}{n} \nabla \cdot \boldsymbol{u} \mathbf{I} \right\|} \left(\mathbf{D} - \frac{1}{n} \nabla \cdot \boldsymbol{u} \mathbf{I} \right) \right] + \rho g \qquad n = 2, 3 \tag{6.16}$$

$$\frac{\partial \rho}{\partial t} + \nabla \cdot (\rho \boldsymbol{u}) = 0. \tag{6.17}$$

In order to complete the system, an additional equation is required in the form of the so-called normality condition:

$$\nabla \cdot \boldsymbol{u} = \frac{\partial q(p, \rho)}{\partial p} \left\| \mathbf{D} - \frac{1}{n} \nabla \cdot \boldsymbol{u} \mathbf{I} \right\|. \tag{6.18}$$

The mathematical and computational methodology presented in Part I can be naturally extended to these compressible granular and powder flow models.

7

Conclusion and outlook

A final concluding note which may help to organize the research priorities and topics to be addressed is pointed out here. In this thesis we have shown that:

Spatial discretization aspects. Nonconforming, rotated multilinear, nonparametric finite elements for the velocity and piecewise constant pressure approximations which are robust with respect to mesh anisotropies and perturbations and satisfy the *inf-sup condition* were our candidates to incorporate edge-oriented stabilization method. We have established a robust stabilization method with respect to parameter weight for both types of CFD's problems: Firstly, the discrete version of *Korn's inequality*, required for problems formulated in terms of the deformation tensor. Secondly, the convection dominated problems were stabilized independenttly of the Reynolds number.

Nonlinear solvers aspects. For this highly nonlinear problem coupling the pressure and velocity even in the viscous term we were applying the continuous Newton method to derive the corresponding continuous Jacobian operators which lead to a rate of convergence independent of mesh refinement. So we avoided the delicate task of choosing the step-length required for a divided difference approach. Moreover, our approach consists of applying fixpoint for the first few nonlinear iterations and switching to full Newton as soon as we reach some given tolerance. This strategy makes our generalized Newton robust with respect to the starting guess. In addition, the accuracy of the linear solver was adapted to the nonlinear one which leads to optimal cost.

Linear solvers aspects. The edge-oriented stabilization involves more than the adjacent elements and the problem of storing the new stabilization matrix arise. We successfully adopted two strategies: First, we store in the stiffness matrix only the partial stabilization matrix which fits with the same standard FEM data structure, while the complementary part only can be assembled via elementwise operations. Moreover, the construction of the preconditioners for the corresponding linear systems will only include parts of the (sub) matrix. Second, we developed a special edge-oriented data structure from the available FEM storage techniques by extending the matrix to support the additional contributed elements. The local matrices can then easily be deduced from the global one which leads to efficient Vanka smoother too, namely the full cell-oriented Vanka smoother. In addition, we treated the velocity-pressure coupling in linearized saddle-point problems, which is nonsymmetric due to the Newton linearization, via local MPSC technique.

It is clear that the usage of edge-oriented techniques will increase in application areas for finite element methods. This is partly due to its ability to stabilize a wide range of problems and to preserve the finite element accuracy and also due to the available modern edge-oriented data structures. Nevertheless, some research topics merit more attention

Based on the extended matrix structures, due to the additional coupling of FEM basis functions by the edge-oriented jump terms, it is needed to improve the linear iterative solvers by employing the complete stiffness matrix: Firstly, by using the edge-oriented Vanka smoother for local MPSC. Secondly, by developing efficient LU decomposition for global MPSC. Then, edge-oriented stabilization technique can find its way to high order finite element method and 3D problems with sufficient efficiency.

The idea of a continuum model for granular materials is of great importance in the food, soil mechanics, and packaging industries. Within these models, some of the characteristics of the flow was successfully captured. Since the simulations of processes, for instance hopper filling and emptying, are of extreme importance for these materials, it is indispensable to incorporate the various surrounding boundaries to derive equations of motion for multi-phase flows. The instability for incompressible powder flow could be regularized by allowing for the changes in density of the media [89, 71] with an extra coupling of the scalar reaction-convection-diffusion equation for the density. The derived techniques in this thesis can successfully be adapted to such coupled problems including further physical models, namely viscoelastic, hypoplastic, and multiphase flow since at least with respect to an algorithmic view the general structure of this coupling is similar.

References

1. Albert, A., Pfeifer, M. A., Brabasi, A. L., and Schiffer, P. Slow drag in granular medium. *Phys. Rev. Lett*, 82:205–208, 1999.
2. Amat, S., Busquier, S., and Candela, V. Third-order iterative methods without using any Fréchet derviative. *J. of Comp. and Appl. Math.*, 158:11–18, 2003.
3. Arnold, D.N., Boffi, D., and Falk, R.S. Approximation by Quadrilateral Finite Elements. *Math. Comput.*, 71(239):909–922, 2002.
4. Baranger, J. and Najib, K. Analyse numerique des écoulements quasi-Newtoniens dont la viscosity obeit la loi puissance ou la loi de carreau. *Numer. Math.*, 58:35–49, 1990.
5. Becker, Ch., Buijssen, S. H. M., Kilian, S., and Turek, S. High Performance FEM Simulation via FEAST and Application to Parallel CFD via FeatFlow. In Horst Rollnik and Dietrich Wolf, editors, *NIC Symposium 2001*, volume 9 of *NIC-Serie*, pages 493–502, 2002. 5.-6. Dezember 2001, Forschungszentrum Jülich.
6. Blazy, S., Nazarov, S., and Specovius-Neugebauer, M. Artificial boundary conditions of pressure type for viscous flows in a system of pipes. *J. math. fluid. mech.*, 2005. to appear.
7. Boffi, D. and Gastaldi, L. On the quadrilateral Q2-P1 element for the Stokes problem. *Int. J. Numer. Meth. Fluids*, 39:1001–1011, 2002.
8. Bramley, R. and Wang, X. *SPLIB: A library of iterative methods for sparse linear systems.* Department of Computer Science, Indiana University, Bloomington, IN, 1997. `http://www.cs.indiana.edu/ftp/bramley/splib.tar.gz`.
9. Brenner, C. S. Korn's Inequalities for Piecewise H^1 Vector Fields. *Math. Comp.*, 73:1067–1087, 2004.
10. Brenner, S. C. and Scoot, L. R. *The Mathematical Theory of Finite Element Methods.* Second edition, Springer, 2002.
11. Brezzi, F. and Fortin, M. *Mixed and Hybrid Finite Element methods.* Springer, Berlin, 1986.
12. Brezzi, F., Franca, L. P., Hughes, T. J. R., and Russo A. Stabilization techniques and subgrid scales capturing. In *In The state of the Art in Numerical Analysis*, IAM Conference Series **63**, pages 391–406. Oxford Univ. Press, 2001. I.S. Duff and G.A. Waston Eds.1 1996.
13. Buijssen, S. H. M. and Turek, S. Sources of Parallel Inefficiency for Incompressible CFD simulation. In B. Monien and R. Feldmann, editors, *Proceedings 8th International Euro-Par Conference*, LNCS, pages 701–704. Springer, 2002. Paderborn, Germany, August 27-30.
14. Burman, E. A unified analysis for conforming and nonconforming stabilized finite element methods using interior penalty. *J. SiNum*, 2004. to appear.
15. Burman, E. and Hansbo, P. Stabilized Crouzeix-Raviart element for the Darcy-Stokes problem . Technical report, Chalmers Finite Element Center, 2003. Preprint 2003-15.
16. Burman, E. and Hansbo, P. Edge stabilization for Galerkin approximations of convection-diffusion-reaction problems . *Comp. Meth. Mech. Eng.*, 193:1437–1453, 2004.
17. Burman, E. and Hansbo, P. A stabilized non-conforming finite element method for incompressible flow. *Comput. Methods. Appl. Mech. Engrg.*, page , 2004. accepted.

18. Burman, E. and Fernández, M. and Hansbo, P., editor. *Edge Stabilization: an Interior Penalty Method for the Incompressible Navier-Stokes Equation*, volume I, 2004. ECCOMAS 4.
19. Chen, Z. Characteristic-Nonconforming Finite-Element Methods for Advection-Dominated Diffusion Problems. *Int. J. Computers & Mathematics with applications*, 48(7-8):1087–1100, 2004.
20. Chorin, A. J. Numerical solution of the Navier–Stokes equations. *Math. Comp.*, 22:745–762, 1968.
21. Ciarlet, P. G. *The finite element method for elliptic problems*. Studies in mathematics and its applications, Vol. 4. North-Holland Publishing Company, Amsterdam, New-York, Oxford, 1978. ISBN 0444850287.
22. Coutinho, L. G. A., Martins, M. A. D., Alves, J. L. D., Landau, L., and Moraes, A. Edge-Based Finite Element Technique for nonlinear Solid Mechanics Problems. *Int. J. Num. Meth. Engng*, 50:2053–2058, 2001.
23. Crouzeix, M. and Raviart, P. A. Conforming and Nonconforming Finite Element Methods for Solving the Stationary Stokes Equations. *RAIRO, Math. Model. Numer. Anal.*, 3:33–75, 1974.
24. Cuvelier, C., Segal, A., and van Steenhoven, A. A. *Finite Element Methods and Navier-Stokes Equations*. Mathematics and Its applications. D. Reidel, Netherland, 1986.
25. Douglas, J. and Dupont, Jr. T. *Interior penalty procedures for elliptic and parabolic Galerkin methods, in: Computing methods in applied sciences (Second Internat. Sympo., Versailles, 1975)*, volume 58. Springer, Berlin, 1976. Lecture Note in Phys.
26. Duan, H. Y. and Liang, G. P. Nonconforming elements in least-squares mixed finite element methods. *Math. comp.*, 93(245):1–18, March 2003. DOI: S0025-5718(03)01520-5.
27. Engelman, M. S., Haroutunian, V., and Hasbani, I. Segregated finite element algorithms for the numerical solution of large–scale incompressible flow problems . *Int. J. Numer. Meth. Fluids*, 17:323–348, 1993.
28. Feistauer, M. Mathematical methods in fluid dynamics. *Pitman Monographs and Surveys in Pure and Applied Mathematics 67, Longman Scientific & Technical*, (67), 1993.
29. Ferziger, J. H. and Peric, M. *Computational Methods for Fluid Dynamics*. Springer Verlag, Berlin–Heidelberg, 1996.
30. Fosdick, R. L. and Rajagopal, K. R. Thermodynamics and stability of fluids of third grade. *Roy. Soc. London Ser. A*, 339(1738):351–377, 1980.
31. Franta, M., Málek, J., and Rajagopal, K. R. On steady flows of fluids with pressure- and shear-dependent viscosities. In *Mathematical, Physical and Engineering Sciences*, volume 461, pages 651–670. The Royal Society, 2005.
32. Fuchs, M. On stationary incompressible Norton fluids and some extension of Korn's second inequality. *J. Analysis Appl. ZAA*, 13:191–197, 1994.
33. Girault, V. and Raviart, P. A. *Finite Element Methods for Navier-Stokes equations*. Springer, 1986. Berlin-Heidelberg .
34. Gremaud, P. and Matthews, J. V. On the Computation of Steady Hopper Flows: I, Stress Determination for Coulomb Materials. Technical report, NCSU-CRSC Tech Report CRSC-TR99-35, 2001.
35. Gresho, P. M. On the theory of semi–implicit projection methods for viscous incompressible flow and its implementation via a finite element method that also introduces a nearly consistent mass matrix, part 1: Theory. *Int. J. Numer. Meth. Fluids*, 11:587–620, 1990.
36. Gresho, P. M. and Chan, S. T. On the theory of semi-implicit projection methods for viscous incompressible flow and its implementation via a finite element method that also introduces a nearly consistent mass matrix. II: Implementation. *Int. J. Numer. Methods Fluids*, 11(5):621–659, 1990.
37. Gresho, P. M. and Sani, R. L. *Incompressible Flow and the Finite Element Method*. Wiley, Chichester, 1998.
38. Grisvard, P. *Elliptic Problems in Non-Smooth Domains*. Pitman, Marshfields, Mass, 1985.
39. Hansbo, P. and Larson, M. G. A Simple Nonconforming Bilinear Element for the Elasticity Problem. Preprint 2001-01, Chalmers Finite Element Center, Chalmers University of Technology, Göteborg Sweden, 2001.
40. Hansbo, P. and Larson, M. G. Discontinous Galerkin and the Crouzeix-Raviat element: Application to elasticity. *M2AN*, 37:63–72, 2001.
41. Heywood, J. P., Rannacher, R., and Turek, S. Artificial boundaries and flux and pressure conditions for incompressible Navier Stokes equations. *Int. J. Numer. Math. Fluids*, 22:325–352, 1996.
42. Homeier, H. H. H. A modified Newton method with cubic convergence: the multivariate case. *J. Comp. Appl. Math.*, 169:161–169, 2004. DOI 10.1016/j.cam.2003.12.041.

43. Homeier, H. H. H. On Newton-Type Methods with Cubic Convergence. *Journal of Computational and Applied Mathematics*, 176:425–432, 2005. DOI: 10.1016/j.cam.2004.07.027.
44. Hron, J., Malék, J., Necãs J., and Rajagopal, K. R. Numerical simulations and global existence of solutions of two-dimensional flows of fluids with pressure- and shear-dependent viscosities. *Mathematics and Computers in Simulation*, 61:297–315, 2003.
45. Hron, J., Málek, J., and Rajagopal, K. R. Simple flows of fluids with pressure dependent viscosities. In *Mathematical, Physical and Engineering Sciences*, volume 457, pages 1603–1622. The Royal Society, 2001.
46. Hron, J., Ouazzi, A., and Turek, S. A Computational Comparison of two FEM Solvers For Nonlinear Incompressible Flow. In *Challenges in Scientific Computing*. Springer, 2004. Cisc 2002.
47. Hron, J. and Turek, S. A Monolithic FEM Solver for ALE Formulation of Fluid Structure Interaction with Configurations for Numerical Benchmarking. In M. Papadrakakis, E. Onate, and B. Schrefler, editors, *Computational Methods for Coupled Problems in Science and Engineering*, volume First Edition, page 148, 2005. Konferenzband 'First International Conference on Computational Methods for Coupled Problems in Science and Engineering' (Santorini, May 25th - 27th).
48. Hughes, T. J. R. *The Finite Element Method: Linear Static and Dynamic Finite Element Analysis*. Prentice-Hall, 1987. New Jersy.
49. Hughes, T. J. R. and Brooks, A. N. A multidimensional upwind scheme with no crosswind diffusion. In *Finite element methods for convection dominated flows*, 1979. New York: ASME 1979.
50. John, V. Higher order finite element methods and multigrid solvers in a benchmark problem for the 3-D Navier-Stokes equations. *Int. J. Numer. Meth. Fluids*, 40:775–798, 2002.
51. John, V., Maubach, J. M., and Tobiska, L. Nonconforming streamline-diffusion-finite-element-method for convection-diffusion problems. *Numer. Math.*, 78:165–188, 1997.
52. Johnson, C. *Numerical solution of partial differential equations by the finite element method*. Cambridge University Press, 1987.
53. Kanschat, G. and Suttmeier, F.-T. A posteriori error estimates for nonconforming finite element schemes. *CALCOLO*, 36:129–141, 1999.
54. Kilian, S. *Ein verallgemeinertes Gebietszerlegungs-/Mehrgitterkonzept auf Parallelrechnern*. PhD thesis, Universität Dortmund, 2001.
55. Kilian, S. *ScaRC als verallgemeinerter Mehrgitter- und Gebietszerlegungsansatz für parallele Rechnerplattformen*. Logos Verlag, Berlin, 2002. ISBN 3-8325-0092-8.
56. Knobloch, P. On Korn's inequality for nonconforming finite elements. *Technische Mechanik*, 20:205–214, 2000.
57. Köster, M. *Robuste Mehrgitter-Krylowraum-Techniken für FEM-Verfahren*. Universität Dortmund, 2004. Diplomarbeit.
58. Kuzmin, D. Positive Finite Element Schemes Based on the Flux-Corrected Transport Procedure. *Computational Fluid and Solid Mechanics*, 2001. 887-888.
59. Kuzmin, D., Löhner, R., and Turek, S. *Flux-Corrected Transport: Principles, Algorithms, and Applications*. Springer, 2005.
60. Kuzmin, D. and Turek, S. High-resolution FEM-TVD schemes based on a fully multidimensional flux limiter. Technical report, Universität Dortmund, Vogelpothsweg 87, 44227 Dortmund, April 2003. Ergebnisbericht Nr. 229.
61. Lacombe, F., Zapperi, S., and Herrmann, H. J. Dilatancy and friction in sheared granular media. *Eur. Phys. J. E*, 2:181–189, 1986.
62. Lee, C.-O., Lee, J., and Sheen, D. A Locking-free Nonconforming Finite Element Method for Planar Linear Elasticity. *Advances in Computational Mathematics*, 19(1-3):277–291, 2003.
63. Leveque, R. J. *Efficient solvers for incompressible flow problems: An algorithmic and computational approach*. Cambridge University Press, 2002.
64. Löhner, R. and Galle, M. Minimization of Indirect addressing for edge-based field solvers. *Comm. Num. Meth. Engng*, 18:335–343, 2002.
65. Luo, P. and Lin, Q. High Accuracy Analysis of the Adini's Nonconforming Element. *Computing*, 68:65–79, 2002.

66. Möller, M., Kuzmin, D., and Turek, S. Implicit finite element discretizations based on the flux-corrected transport algorithm. *International Journal for Numerical Methods in Fluids*, Volume 47, Number 10 - 11:1197–1203, April 2005.
67. Nedderman, R. M. *Static and Kinematic of Granular Material*. Cambridge Uni. Press, Cambridge, New York, 1992.
68. Nitsche, J. On Korn's second inequality. *R.A.I.R.O.*, 15:562–580, 1981.
69. Oswald, H. *Parallel Multigrid Algorithms for Solving the Incompressible Navier–Stokes Equations with Non-conforming Finite Elements in Three Dimensions*. PhD thesis, Universität Heidelberg, 1998. (mit R. Rannacher).
70. Ouazzi, A. A mixed formulation of the Stokes equation in terms of (ω, p, u). *Numer. Algorithms*, 21(1-4):343–352, 1999.
71. Ouazzi, A., Turek, A., and Hron, J. Finite Element Methods for the Simulation of Incompressible Powder Flow. *J. CNME*, :, 2005. in press.
72. Ouazzi, A. and Turek, S. Numerical Methods and Simulation Techniques for Flow with Shear and Pressure dependent Viscosity. In *Numerical Mathematics and Advanced Applications*. Springer, 2003. ENUMATH2003.
73. Ouazzi, A. and Turek, S. Unified edge-oriented stabilization of nonconforming finite element methods for incompressible flow problems. *J. Numer. Math.*, 2005. submitted.
74. Park, C. and Sheen, D. P_1-Nonconforming Quadrilateral Finite Element Methods for Second-Order Elliptic Problems. *SIAM J. Numer. Anal.*, 41(2):624–640, 2003.
75. Rannacher, R. and Turek, S. A Simple nonconforming quadrilateral Stokes element. *Numer. Methods Partial Differential Equations*, 8:97–111, 1992.
76. Raviat, P. A. and Thomas, J. M. *Introduction à l'analyse numérique des équations aux dérivées partielles*. Masson, Paris, 1983.
77. Rees, I., Masters, I., Malan, A. G., and Lewis, R. W. An edge-based finite volume scheme for saturated-unsaturated groundwater flow. *Comput. Methods. Appl.Mech. Engrg.*, 193:4741–4759, 2004.
78. Saad, Y. and Schultz, M. H. **GMRES:** A generalized minimal residual alghorithm for solving nonsymmetric linear systems. *SIAM J. Sci. Stat. Comput.*, 7:856–869, 1986.
79. Schaeffer, D. G. Instability in the evolution equation describing incompressible granular flow. *J. of Differential Equations*, 66:19–50, 1987.
80. Schaeffer, D. G. *Mathematical Issues in the continuum formulation of slow granular flow*. Springer, 1997.
81. Schieweck, F. and Tobiska. L. A nonconforming finite element method of upstream type applied to the stationary Navier-Stokes equation. *R.A.I.R.O. Modelisation Math. Anal.*, 23(4):627–647, 1989.
82. Schmachtel, R. *Robuste lineare und nichtlineare Lösungsverfahre für die inkompressiblen Navier-Stokes-Gleichungen*. Universität Dortmund, 2003. PhD thesis.
83. Schwab, C. *p- and hp-finite element methods*. Oxford, Clarendon Press, 1998. ISBN 0-19-850390-3.
84. Seshaiyer, P. Stability and Convergence of Nonconforming hp Finite-Element Methods. *Computers Math. Appl.*, 46:165–182, 2003.
85. Specovius-Neugebauer, M. Approximation of the Stokes Dirichlet problem in domains with cylindrical outlets. *SIAM J. Math. An.*, 30:645–677, 1999.
86. Stang, G. and Fix, G. J. *An Analysis of the Finite Element Method*. Prectice-Hall, New York, 1973.
87. Stynes, M. and Tobiska, L. The streamline-diffusion method for nonconforming q_1^{rot} elements on rectangular tensor product meshes. *IMA Journal of Numerical Analysis*, 21:123–142, 2001.
88. Tardos, G. I. A Fluid Mechanics approach to slow frictional Powder Flows. *Powder Technology*, 15:61–74, 1997.
89. Tardos, G. I., McNamara, S., and Talu, I. Slow and intermediate flow of a frictional bulk powder in the Couette geometry. *Powder Technology*, 4686:1–17, 2002.
90. Turek, S. *Ein robustes und effizientes Mehrgitterverfahren zur Lösung der instationären, inkompressiblen 2-D Navier-Stokes Gleichung mit diskret divergenzfreien finiten Elementen*. University of Heidelberg, 1991. Dissertation.
91. Turek, S. FEATFLOW . Finite element software for the incompressible Navier-Stokes equations: User Manual, Release 1.1. *Technical report*, 1998.

92. Turek, S. *Efficient solvers for incompressible flow problems: An algorithmic and computational approach*. Springer, 1999.
93. Turek, S. Korn's inequality for the rotated bilinear element. Technical report, Universität Dortmund, 2000. Interior note.
94. Turek, S., Becker, Ch., and Oswald, H. Parallel multilevel algorithms for solving the incompressible Navier–Stokes equations. In *Proceedings of the High Performance Workshop at the HLRZ Stuttgart*, 1998.
95. Turek, S., Hron, J., and Grajewski, M. Dual Weighted a Posteriori Error Estimation for a New Nonconforming Linear Finite Element on Quadrilaterals. In A. Meyer and T. Apel, editors, *16th Chemnitz Finite Element Symposium*, Applied Numerical Mathematics, July 2004. Tagungsband 16th Chemnitz Finite Element Symposium 2003.
96. Turek, S. and Kilian, S. An example for parallel ScaRC and its application to the incompressible Navier-Stokes equations. In *Proc. ENUMATH-97*. World Science Publ, 1998.
97. Turek, S. and Oswald, H. A parallel multigrid algorithm for solving the incompressible Navier–Stokes equations with nonconforming finite elements in three dimensions. In *Proc. Parallel CFD'96, Capri/Italy*, 1996.
98. Turek, S., Ouazzi, A., and Schmachtel, R. Multigrid Methods for Stabilized Nonconforming Finite Elements for Incompressible Flow involving the Deformation Tensor formulation. *J. Numer. Math.*, 10:235–248, 2002.
99. Turek, S., Rivkind, L., Hron, J., and Glowinski, R. Numerical analysis of a new time-stepping θ-scheme for incompressible flow simulations. Technical report, Universität Dortmund, 2005. Technischer Report Nr. 282.
100. Turek, S. and Schäfer, M. Benchmark computations of laminar flow around cylinder. In E. H. Hirschel, editor, *Flow Simulation with High-Performance Computers II*, volume 52 of *Notes on Numerical Fluid Mechanics*, pages 547–566. Vieweg, 1996. co. F. Durst, E. Krause, R. Rannacher.
101. Van der Vorst, H. A. **BICGSTAB:** A fast and smoothly converging variant of Bi-CG for the solution of nonsymmetric linear systems. *SIAM J. Sci. stat. Comput.*, 13 (2):631–644, 1992.
102. Van Kan J. A second–order accurate pressure–correction scheme for viscous incompressible flow. *SIAM J. Sci. Stat. Comp.*, 7:870–891, 1986.
103. Vanka, S. P. Implicit Multigrid Solutions of Navier-Stokes Equations in Primitive Variables. *J. of Comp. Phys.*, 65:138–158, 1985.